5-27-2016

# Nano-Photonic Waveguides for Chemical and Biomedical Sensing

Surya Venkatasekhar Cheemalapati
*University of South Florida*, cheemalapati@mail.usf.edu

# Nano-Photonic Waveguides for Chemical and Biomedical Sensing

by

Surya Venkatasekhar Cheemalapati

A dissertation submitted in partial fulfillment
of the requirements for the degree of
Doctor of Philosophy in Chemical Engineering
Department of Chemical and Biomedical Engineering
College of Engineering
University of South Florida

Major Professor: Anna Pyayt, Ph.D.
Venkat Bhethanabotla, Ph.D.
John Kuhn, Ph.D.
Manoj Ram, Ph.D.
Shengqian Ma, Ph.D.

Date of Approval:
May 10, 2016

Keywords: Single Cell Analysis, Nanoendoscopy, Plasmonics, Polysilicon

## DEDICATION

This dissertation is dedicated to my parents, C. Hymavathi and C. S. Murty.

## ACKNOWLEDGEMENTS

I would like to express my sincere gratitude to my advisor Dr. Anna Pyayt for guiding me through my Ph.D. I thank her for making me part of her research group at University of South Florida. I am extremely grateful to her for the opportunities she provided for me to pursue research in the field of Chemical and Biomedical engineering. She helped me sail through difficult times and has always been a source of strength and inspiration.

I thank my committee members for their support and guidance through the course of my graduate school.

I would like to thank my Parents, C. Hymavathi, my mother, an artist of many forms- singer/ painter/ writer and C.S. Murty, my father, a Chemical Engineer himself, for encouraging me to pursue graduate studies. I thank my brother, Krishnayya, for inspiring me and guiding me in my pursuit of higher studies. I thank him and his family, Shilpa, Abhay and Akshaya for all the love and support. I would like express my greatest appreciations to my wife, Sowmya, for being extremely supportive and accompanying me through the course of my graduate school. She has provided me with strength and encouragement to help me pursue my goals.

I would like to thank all the lab members and collaborators at University of South Florida. I am grateful for all their support. They have helped me with preparing samples for various experiments, become proficient on various tools, conduct data acquisition and data analysis.

I am thankful to the staff at Nanotechnology Research and Education Center (NREC) where I conducted several fabrication and characterization experiments.

Lastly I would like to thank all my friends who have been there for me during my time at University of South Florida and Oregon State University. Their support and encouragement has been phenomenal and I will always be grateful to them.

## TABLE OF CONTENTS

## LIST OF TABLES

## LIST OF FIGURES

## ABSTRACT

In this dissertation, advances in the fields of Photonics, and Plasmonics, and specifically, single cell analysis and waveguide sensing will be addressed. The first part of the dissertation is on Finite Difference Time Domain (FDTD) optimization and experimental demonstration of a nano-scale instrument that allows sensing at the cellular and subcellular levels. A new design of plasmonic coupler into a nanoscale waveguide is proposed and optimized using FDTD simulations. Following this, a subcellular nanoendoscope that can locally excite fluorescence in labelled cell organelles and collect the emitted fluorescent light for detailed spectrum analysis is fabricated and tested. The nanoendoscope has a sharp tapered tip of diameter ~ 50 nm that permits safe insertion into the cell that was confirmed by a number of viability experiments. FDTD analysis demonstrated that, with an optimized nanoendoscope taper profile, light emission and collection was very local. Thus, signal detection could be used for nano-photonic sensing of proximity of fluorophores. In further experiments, fluorescent signals were collected from individual organelles of living cells including: the nucleus of Acridine orange labelled human fibroblast cells, the nucleus of Hoechst stained live liver cells and the mitochondria of MitoTracker Red labelled MDA-MB-231 cells. In addition, this endoscope was inserted into a live organism, the nematode *Caenorhabditis elegans*, and *in- vivo* fluorescence signal was collected. Second, an innovative single step fabrication method of low loss polysilicon waveguides was developed as a potential platform for a number of photonic sensors. Optimization of a capacitively coupled plasma etching for the fabrication of a polysilicon

waveguide with smooth sidewalls and low optical loss was demonstrated. A detailed experimental study on the influences of RF plasma power and chamber pressure on the roughness of the sidewalls of waveguides was conducted and waveguides were characterized using a scanning electron microscope. It was demonstrated that optimal combination of pressure (30 mTorr) and power (150 W) resulted in the smoothest sidewalls. The optical losses of the optimized waveguide were 4.1± 0.6 dB/ cm. Finally, an on-chip nanophotonic sensor for continuous blood coagulation analysis was proposed. The system was simulated using three-dimensional FDTD software. At first, the noise due to the presence of cells was calculated. Next, the design of a waveguide cladding-based filtering structure for elimination of the noise from cells was proposed and significantly decreased noise level was theoretically demonstrated.

# CHAPTER 1: INTRODUCTION

According to the National Academy of Science, nanophotonics is defined as "the science and engineering of light matter interactions that take place on wavelength and subwavelength scales where the physical, chemical or structural nature of natural or artificial nanostructured matter controls the interactions" [1]. Nanophotonic devices are classified into three fundamental types based on the interactions with light i) plasmonics which uses nanoscale medium to confine light in very small volumes ii) optical waveguides which use a large contrast in refractive indices in device to transmit light and iii) photonic crystals which uses nanometer sized periodic arrays of high and low refractive index structure to control propagation of light [2]. This dissertation mostly focuses on waveguiding and plasmonic aspects of nanophotonic devices.

Nanophotonic devices are fabricated using various materials such as: silicon [3], diamond [4], grapheme [5], metal and semiconductor nanowires [6-9] and others which involve several approaches for fabrication of nanophotonic devices. One of them is top-down approach using traditional microelectromechanical systems (MEMS) techniques, while the other one is bottom-up, based on chemical synthesis of desired structures [10]. This thesis discusses several fabrication approaches including photolithography, wet and dry etching and their combination.

Application of nanophotonic devices include optical interconnects [11], magnetic and electric field sensors [4], photodetectors [12], chemical and biomedical sensors [13-15] and, light trapping nanophotonic structures for photovoltaics [16]. The nanophotonics broadly impacts the biomedical research and technology for studying the fundamentals of interactions and dynamics

at single cell/ molecule level [17] and along with other important applications such as bioimaging [18], light activated medical therapy [19], plasmonics [20], photonic crystal biosensors [21] and nano clinics for optical diagnostics [22]. In this dissertation a novel single cell analysis technology based on nanowires that can be used to deliver light into single cells is proposed and its design is optimized using FDTD software. Following this, a nanoscale-endoscope is fabricated, characterized and applied for *in- vivo and in- vitro* analysis. Next, a one-step fabrication technique for low loss polysilicon waveguide is discussed. Finally, an on-chip silicon waveguide that can be used to measure refractive index of surrounding material is discussed.

# CHAPTER 2: SINGLE CELL ENDOSCOPY

## 2.1 Note to the Reader

Portions of this chapter have been published in Optics Express 28001-28009 (2013) and have been reproduced here with permission from The Optical Society (OSA).

## 2.2 Introduction

Single cells are heterogeneous in nature due to stochasticity in gene [23], protein [24] expression and differences in ion concentration [25]. Information on cellular heterogeneity can help elucidate the pathophysiology of many diseases such as cancer [26-29] and facilitate the design of new therapies [30-32]. This can be achieved by performing fundamental analysis of the molecular dynamics inside single cells. Until recently, cells were considered uniform and average response of a culture of cells was considered for analysis [33]. It has been shown that studies based on cell populations conceal heterogeneity [24] such as responses to stimuli [26-28] or cell drug interactions [29]. Further, molecular biology studies performed outside living cells [34] do not capture the complexity occurring inside the single cell [35] and are destructive [36]. To perform analysis at cellular and subcellular level, various (single cell analysis) technologies have been developed. These include microscopy, various cell sorting technologies and recently developed nanotechnology based devices. Their advantages and limitations will be discussed in the following section.

Microscopy is one of the most popular analysis tools in cellular biology. They are categorized based on the technology used for illumination and image formation. Techniques like

confocal [37], multiphoton excitation fluorescence microscopy [38,39], STED [40], STORM [41] allow imaging at sub-cellular levels, but typically are performed on fixed cells. They do not provide required biochemical information [42], which is crucial [43] for monitoring drug-cell interactions at single cell level. Also, microscopy conducted on fixed cells does not provide dynamic information. However, recent advances in technology led to the invention of structured illumination microscopy (SIM) [44] which can perform high resolution dynamic imaging on live cells. However this technique is still very expensive and has limited availability. The most important limitation of all microscopy techniques is sample preparation. Imaging can only be conducted on homogenous samples and almost always *in- vitro*. A non-homogenous sample, such as an insect or a live organism, cannot be studied unless it is dissected. This limits the range of experiments that can be conducted using this technology.

Another approach to single cell analysis is flow cytometry. Flow cytometry and, specifically, fluorescence activated cell sorting (FACS) can perform analysis on thousands of single cells per minute and sort them according to their size and fluorescence intensities to determine cell viability, protein and gene expressions [45,46]. This technology can perform dynamic analysis but not at a single cell resolution. Additionally, it has limitation in terms of spatial resolution [33].

Several of these limitations can be overcome by using nanotechnology instruments which allow sensing at the cellular/ subcellular level [32,47,48], facilitate single cell analysis and are minimally invasive. Until recently, various single cell devices have been reported. These include; carbon nanotubes on AFM tips [49,50]; glass pipettes [27,51]; capillaries [52]; boron nitride nanotubes affixed onto tungsten wires [53]; sharpened macroscopic needles [54]; Ag nanowires on an electrochemically etched Tungsten tip [55]; FIB-milled AFM tips [56]; optical fiber-

nanowire-based endoscopes [57,58]; optical fiber- photonic crystal based endoscope [59]; and finally, nanofibers [28,31,43,60-66]. These devices can perform intracellular sensing of enzymes [28,60], pH [43], calcium ions [31,61], biomarkers [62-65], and quantum dots [57] using fluorescence. Intracellular protein sensing using nanocavities [59] or localized surface plasmon resonance [66]. Additionally, they can conduct in- situ electrochemical measurements [51,53] or SERS measurements for sensing biomolecules in single cell organelle [51,52,67]. Apart from sensing, these devices can also perform payload delivery of quantum dots, [49,54,57] DNA, [56] and fluids [51].

However, widespread application of these devices has been limited because their fabrication is difficult to scale up due to extensive use of manual assembly [53,57,59]. Additionally, they usually require sophisticated external detectors for signal detection [68]. Next additional information of the existing single cell technologies are discussed in more detail, case on case basis.

Variety of intracellular parameters can be measured using nanofiber biosensors. For example, calcium ion concentration in single cells was measured using a nanofiber biosensor in [31] and [61]. The experiments were conducted because calcium ions are important signaling agents. They act as intracellular messengers which transmit information inside cells to control their activity. Increase in calcium ion concentration can cause cell death. In these studies, the nanofibers were coated with Calcium Green-1Dextran. It is a fluorescent dye sensitive to calcium ions, which can be excited with 488 nm light and emits fluorescence at 530 nm. The ion concentrations were calculated from the fluorescence intensity change monitored using an external detector attached to the microscope objective. pH is another important parameter that was monitored inside single cells using nanotechnology based devices. pH inside single cells was

sensed using a nanofiber coated with pH sensitive dye [43]. Fluorescence signal was monitored using an external detector attached to the microscope objective. Similarly several biomarkers [62-65] were detected inside single cells. Antibody-immobilized nanofibers were used to detect benzopyrene tetrol (BPT), a biomarker for exposure to carcinogenic benzo *a* pyrene (BaP) [62,64]. Another cancer biomarker telomerase was detected using an enzyme coated nanofiber in [63].

The onset of apoptosis in a single cell was also detected using nanotechnology based devices. This was done by monitoring enzymatic activity of caspase-9 [60] using an enzyme coated nanofiber. Caspase-9 occurs inside single cell when apoptosis is induced. Similarly, other single cell sensing studies were conducted using an enzyme coated nanofibers. Extracellular lactate concentrations, a metabolite marker for cancer, were sensed in single cells [28]. Intracellular protein p53 was measured inside single cells using a nanofiber using localized surface plasmon resonance [66]. Other important intra cellular parameters such as cytochrome c [69], nitric oxide [70] have also been monitored. In all the fluorescent sensing studies mentioned above [28,31,60-65,68-70] the nanofiber was decorated with molecules that bind with the analyte of choice and produce changes in fluorescence intensity which was picked by the detector attached to the microscope objective. This makes them highly specific to single analyte and dependent upon the external detectors.

Along with nanofibers, single cell devices have also been fabricated using nanowires, nanotubes, photonic crystals and other technologies (for eg. AFM tips). Carbon nanotubes (CNTs) due to their small dimensions and high tensile strength have been used to probe single cells [49-51] and deliver cargo. For example, in [49] quantum dots were delivered into the cells. The device was made by attaching CNT onto an AFM tip using a nano manipulator inside a

scanning electron microscope and cut to desired length using an electron beam. Next, the CNT was functionalized and loaded with quantum dots. The device was used to probe HeLa cells where it was kept inside the cell for 15 minutes during which the quantum dots were cleaved due to the reductive environment inside single cells. Following this, the cell containing quantum dots was imaged using fluorescent microscopy. In another study [51], CNT on glass pipettes was used to perform sensing inside single cells. Device was fabricated by placing the CNT on the glass pipette using a flow through technique and then sealed with epoxy. For accurate positioning of the endoscopes, the CNTs were filled with super paramagnetic nanoparticles that would allow magnetic manipulation. Following this different types of tips were then prepared, each with different capabilities. The devices were used to study human carcinoma cell line HeLa and human osteosarcoma HOS cells. Surface enhanced Raman spectroscopy (SERS) active endoscopes were prepared by depositing gold nanoparticles on the functionalized CNT. Glass pipettes were coated with carbon to perform electrochemical measurements. Chemical identification using SERS was performed in HeLa cells and preliminary electrodynamics studies in salt solutions were performed. Additionally, fluorescent molecules were also transferred to HOS cells.

In a recent study [52], SERS was conducted in HeLa cells using CNT decorated with gold nanoparticles affixed onto pulled glass capillaries using epoxy. It was suggested that the sensitivity of SERS endoscopes could be used for real time analysis of heterogeneous cells. In [67], SERS experiments were conducted with a pulled glass nanopipette functionalized with gold nanoparticles via electrostatic interactions between the nanoparticles and polymer coatings. HeLa cells were used in this study. The nanopipette was used for in- situ intracellular analysis during external stimuli. The cell’s response to addition of KCl was monitored in real time. A

significant limitation of some of the technologies discussed above is the need to use epoxy to assemble the device. This limits reproducibility of the device and also inhibits mass production or lab to lab transfer of technology.

There were several single cell endoscopy studies based on nanoneedles and nanotubes. In another study [53], the authors fabricated a nanotube based (needle nanoprobe) electrodes and studied their electrochemical measurements in microenvironments. For fabrication, a boron nitride nanotube was attached to a metal microelectrode followed by depositing thin layers of metal by sputtering and insulating polymer by electro polymerization. The final step involved FIB cutting of end of the coated nanotube to expose the electrochemical sensing site. The authors did not perform any intracellular studies but suggested that application. In another study, [56], a nanoneedle was used to deliver payload into single cells. The nanoneedle of 200 nm diameter was fabricated by etching of Si AFM tips using Focused Ion Beam (FIB). Avidin was coated onto the nanoneedle and DNA was immobilized onto the needle using avidin-biotin interactions. HEK293 cells were used for their study. The DNA immobilized nanoneedle was inserted into a single cell repeatedly to deliver DNA. The nanoneedle fluorescence was monitored under confocal microscope to estimate the amount of DNA transferred, but the authors could not estimate the exact amount based on their imaging techniques.

Hybrid (nanowire/ nanotube) quantum dot (QD) combination has also been used for single cell analysis [57]. QD's as a biosensors are advantageous [71] due to their small size, bright and stable fluorescence [54], and low photobleaching [49]. Nanoneedles were used to deliver quantum dots into single cells for subsequent analysis [54]. Here, the endoscopy device was fabricated by attaching a boron nitride nanotube onto a sharpened macroscopic needle. Following this, the nanotube was coated with gold to enable surface modifications. QD's were

attached to the nanotube via disulfide bonds and were cleaved using the reductive environment inside single HeLa cell's cytoplasm. The nanoneedle was inserted in single cells for 15-30 minutes to facilitate the reductive cleavage of disulfide bonds. The diffusion of released quantum dots across the cell was observed to estimate several biophysical properties of the cell. In another study [59], the authors glued a photonic crystal nanocavity containing quantum dots and obtained nanocavity spectra from inside a single cell. The photonic crystal was inserted into PC3 human prostate cancer cell line and spectra from inside the cell were recorded into a spectrometer. In a separate experiment, the photonic crystal was cleaved inside the cancer cells and cell viability was observed. Following this *in- vitro* protein, streptavidin, sensing experiments were demonstrated.

Nanowires have also been extensively used in fabrication of single cell analysis technologies. In a recent study [55], SERS measurements were performed using a silver nanowire (Ag NW) attached to a Tungsten (W) tip. The Ag NWs were attached to an electrochemically etched tungsten tip via alternating current (AC) dielectrophoresis method and then glued using epoxy. HeLa cells were used for their studies. SERS spectra were measured by inserting the probe into the cell. In another study [57], $SnO_2$ nanowires were used to deliver quantum dots inside single cells and collected spectra from them. In another study [72], Aminopropyl tri-ethoxysilane (APTES) modified ZnO nanowires were used for single cell analysis. They were inserted into single cells by endocytosis and change in intensity upon interaction with DNA was observed. ZnO nanowires are biocompatible and advantageous due to their light guiding properties.

These devices demonstrate ability to perform analysis at single cell level. However, most of them are difficult to mass produce. One common feature among most of these devices is the

use of gluing materials like epoxy which could lead to intra device variability. A summary of these devices is provided in Table A1. The next section will introduce a novel design for reproducible single cell analysis device based on nanowires.

### 2.2.1 Nanowire-based Single Cell Endoscope

The advantages of the nanowire based design are very small excitation volume and less invasive penetration through the cell membrane, allowing study of photosensitive processes inside of a living cell. The idea is derived from a recently demonstrated technology [57], but the fabrication is complex and requires manual assembly of nanowires which makes them a single use devices. In order to make transition from the single use experimental tools demonstrating the principle to more standard device configuration suitable for mass-production and use in biomedical research labs, a much better understanding of the design principles on the nanoscale is required. Specifically, for the nanoscale endoscopes, predictable and controllable interface between the nanowire and the macroscopic world has to be developed. Ideally light should be coupled from a regular optical fiber, so this requires creation of a coupling structure from the optical mode propagating in the fiber into the optical mode that propagates in the nanowire. The requirements would be to minimize manual assembly and use standard MEMS techniques of fabrication together with traditional parallel nanowire growth procedures. Additional set of constraints comes from the need to couple light well into the nanowire while minimizing the background exposure decreasing imaging contrast.

Ultra-high resolution imaging of the cell interior can be done by 3D-scanning the nanoendoscope with very small steps (20-40 nm are easily attainable by contemporary micromanipulators). Camera designed for visible light and near IR light will not detect 1550 nm

excitation light, while second harmonic generation or two photon imaging can be detected by the camera attached to the microscope [73-77].

## 2.3 Methods

### 2.3.1 Design of Novel Single Cell Endoscope

The pioneering device demonstrated by Peydong Yang's lab [57] was using nanowires manually glued to the thinned fiber. For this configuration, it is hard to predict efficiency of coupling as well as other parameters of the endoscope such as mechanical robustness and effects of diffraction of light at the tip of the fiber on the overall device performance. Here an alternative approach is proposed that would simplify the manufacturing process, at the same time giving more broad control over the distribution of light intensity in the vicinity of the nanoprobe tip. The suggested design does not require thinning of the fiber core, instead, a thin metal ring can be deposited on the cleaved tip of the fiber for the selective coupling of the light from the fiber core to the nanowire as shown in Figure 1. FIB can be used to pattern a circular opening in the center of the fiber. Just single use of FIB is required, and then the design can be reproduced on many fibers using *align-and-shine* photolithography process [78]. The nanowire can be directly grown in the opening using one of many, gas [79-81] and hydrothermal [82-84] nanowire growth techniques. Overall proposed design significantly increases the reliability and ease of production, offering unprecedented control over the light field.

Figure 2 demonstrates modes propagating in the optical fiber and the nanowire used in the simulations. The two left images are the side view of the field distribution in the nanowire (top) and the fiber (bottom). On the right is shown a cross section of the mode coupled in the nanowire (top) and the fiber (bottom). It can be seen that the sizes of the modes are very different and that for the nanowire large portion of energy is concentrated around the nanowire.

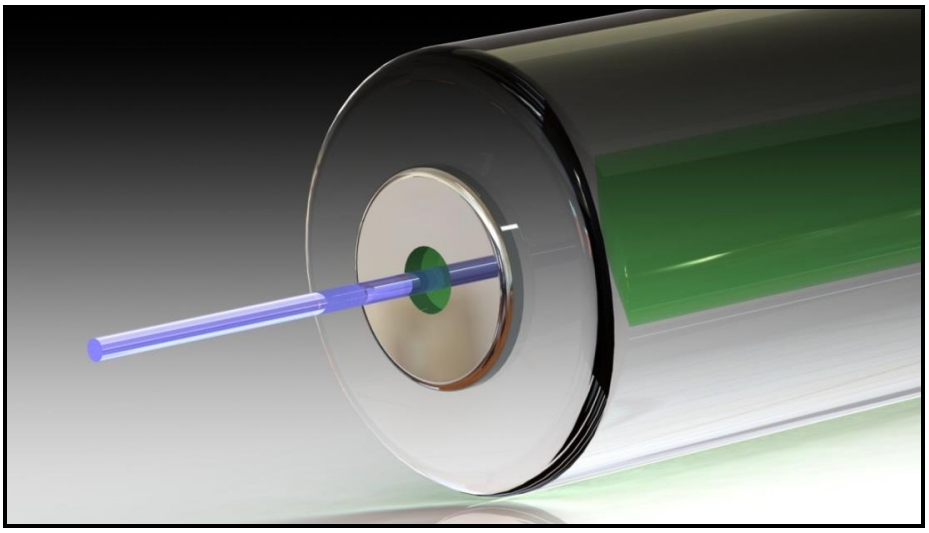

Figure 1 Schematics of the proposed design of the new nanowire-based single cell nanoendoscope. (Not to scale). First, thin film of metal is deposited on the cleaved fiber interface covering the core of the fiber. Then, an opening is milled in the center of the fiber interface using FIB. The purpose of the metal protection is to prevent light leakage and to optimize coupling of the light into the nanowire. Finally, the nanowire is grown directly in the opening of the fiber.

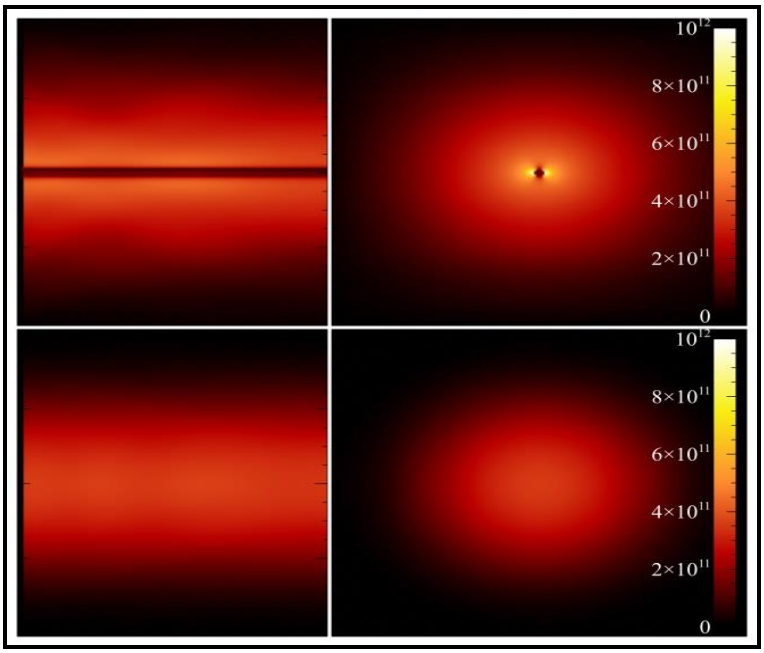


Figure 2 Mode propagating in the nanowire and optical fiber. Nanowire (Top) and the optical fiber (bottom). Side view (left) and cross-section (right) are shown.

## 2.4 Simulations

Three-dimensional simulations were performed on commercial FDTD software. The design parameters were: wavelength 1.5 μm, single mode optical fiber with refractive index 1.46 and 8 μm core diameter, layer of metal on the tip of the fiber with thickness of 200nm. An opening was located in the center of the metal film with the radius that was varied between 0.1 and 3.0 μm. A nanowire made of ZnO with refractive index of 2, diameter of 200 nm and length of 2μm was placed in the center of the opening at the end of the fiber. Light was propagating in the fiber and then coupled to the nanowire. The efficiency of coupling varied depending on the radius of the opening in the metal.

## 2.5 Results and Discussions

Distributions of electric field amplitude were measured in the plane that was parallel to the initial polarization of the coupled mode and the optical axis of the fiber. To estimate the contribution into field distribution introduced by the nanowire, initial simulations were performed for a configuration that did not have nanowire (Figure 3 (a)) and then the nanowire was added (Figure 3 (b)). Opening in the metal layer had radius δ ranging from 0.2 μm to 2.8 μm. Afterwards, a direct difference of the field amplitudes were calculated to estimate the contribution of the mode coupled into the nanowire into the total field distribution around the nanowire (Figure 4 (a)). Division of the simulated field intensity of configuration containing nanowire on the field intensity of configuration without nanowire were used to estimate the effect of local field enhancement introduced by the nanowire (Figure 4 (b)). While division provides information about relative intensity, difference describes absolute value that can be relatively small for the openings with the smaller radius.

First of all, it can be noticed that in absence of the nanowire (Figure 3 (a)) there is a cut off radius of the opening in the metal (~0.8 μm) after which light does not escape the fiber, exhibiting evanescent behavior. With larger openings a typical field distribution of diffraction on an opening can be observed.

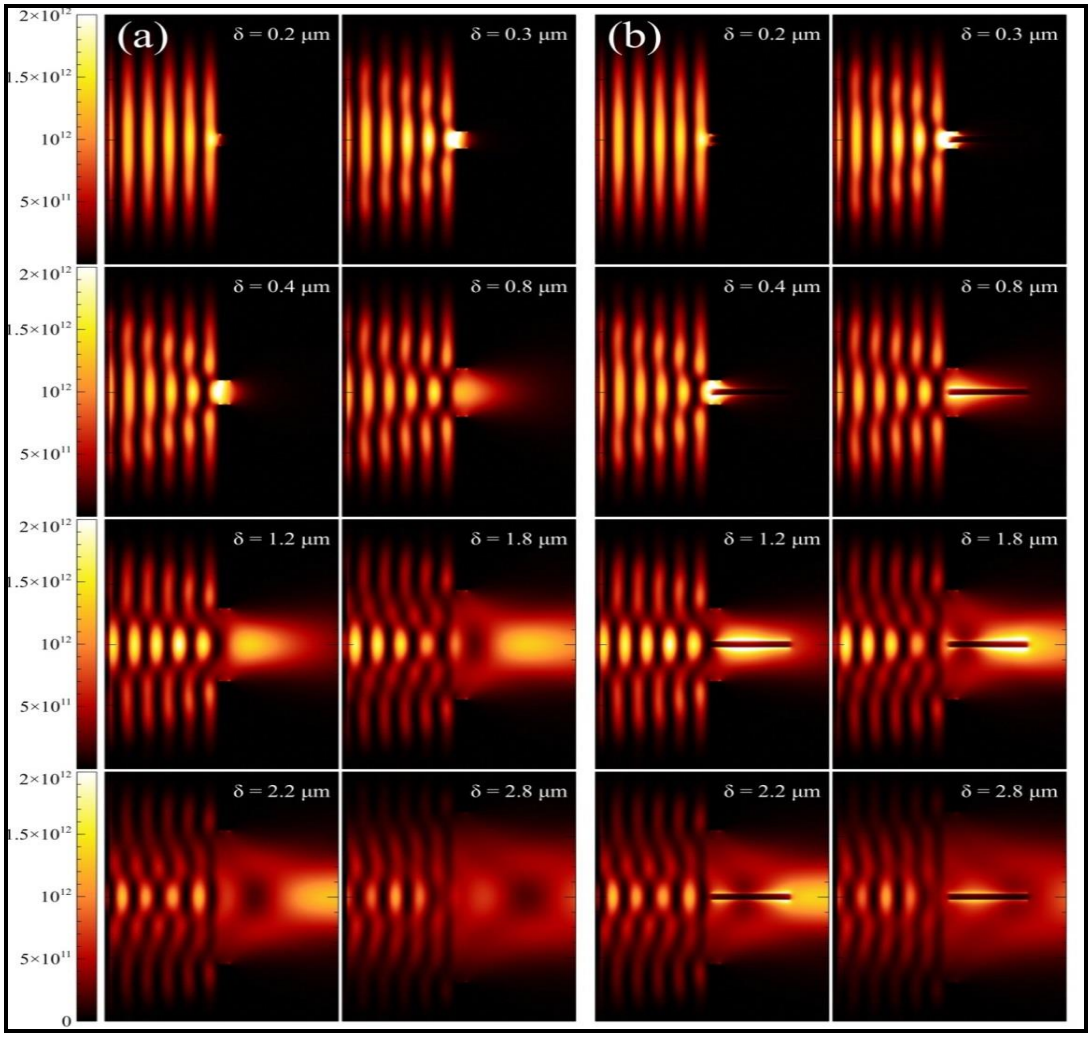


Figure 3 Simulation of the light propagation outside of the optical fiber through the metal opening when the nanowire is absent (a) and present (b). Each section demonstrates light intensity distribution in cross-section of the system demonstrated in Figure 1. The left side of each individual section corresponds to the light propagating in the core of optical fiber, thin metal layer (not visible) with opening is located in the center of the section, while the right part of the section corresponds to the light propagating through the opening out of the fiber core with (b) or without (a) the nanowire.

Next, when the nanowire is added to the system the field distribution outside of the optical fiber changes significantly (Figure 3 (b)). It can be observed that even for the openings in metal with a radius smaller than cut off radius, light propagates by coupling into the nanowire. When the radius of the opening is increased, it reaches the point when light couples into the nanowire only partially, with some amount of the light propagating in the space around the nanowire. This was investigated further in Figure 4 (a) showing difference in the field amplitude when nanowires were present and absent. Dark red corresponds to zero difference, while brighter areas indicate that the field with nanowire is higher than the field without it, vice versa, darker areas indicate that the fields without nanowire in that area is higher. Figure 4 (b) illustrates the ratio of the corresponding intensities. It can be observed that for the opening 0.2 μm extremely low light propagation is observed outside of the optical fiber.

For the opening with 0.3 and 0.4 μm radius there are two observations. First, light is locally enhanced in the metal opening due to plasmonic effects. Abnormally high propagation through sub-micron holes has been observed previously experimentally and theoretically [85-87], what comes in good agreement with these simulations. Second, outside of the metal opening light propagates along the nanowire in a uniform mode with the field concentrated closely around the nanowire in a way similar to the mode supported by the nanowire shown in Figure 2.

For larger openings presence of the nanowire has changed propagation of the light outside of the optical fiber. First of all, Figure 4 (a) with the difference of the fields in presence/absence demonstrates that the field around the nanowire is locally enhanced. There are two possible mechanisms explaining this effect. One of them is coupling of the light into nanowire and propagation it outside of the optical fiber. Second is a local field enhancement purely related to the difference in refractive indices between air and ZnO. The ratio of the

influence of those two mechanisms can be extracted from comparison of the substration and divisions of the fields with and without nanowires (Figure 4 (a) and (b)). It can be noticed that for larger openings presence of the nanowire causes uniform field enhancement along the nanowire (Figure 4 (b)), even when the field itself is not uniform (Figure 3 (a)). This indicates domination of the local field enhancement, since the nanowire mode is much more uniform along its length. This area corresponds to more than 2 times stronger field around the nanowire, which is in good agreement with theoretically expected based on refractive indices difference.

When the radius of the opening decreases below 0.8 μm the light intensity in the area around the nanowire normalized to the field without nanowire, is getting higher with the decrease of the opening, as demonstrated on Figure 4 (b). It can be explained by significantly less light escaping the fiber through the opening in the metal film and propagation through the mode coupled into nanowire playing more significant role.

To finalize, in order to deliver light using this nano-scale single cell endoscope inside the cell in close proximity to the different fluorescently tagged structures light has to propagate along the nanowire. To achieve high resolution scanning of the cell interior light has to be present in a small excitation volume. There is trade-off between two different configurations. If high contrast is extremely important, the best way is to create small opening in the metal layer. Light from the whole area of the opening will be coupled into mode supported by the nanowire while non-coupled light leakage around the nanowire will be minimized. It was shown that the coupling is optimal, and the excitation volume is minimal with the radius of the metal opening to be 0.4 μm. If the background light is not too critical, but local contrast is the most important, then openings between 0.4 and 0.8 μm would provide enough light outside of the optical fiber

than would be locally enhanced by the nanowire. Openings larger than 0.8 μm just create additional background increasing the level of noise.

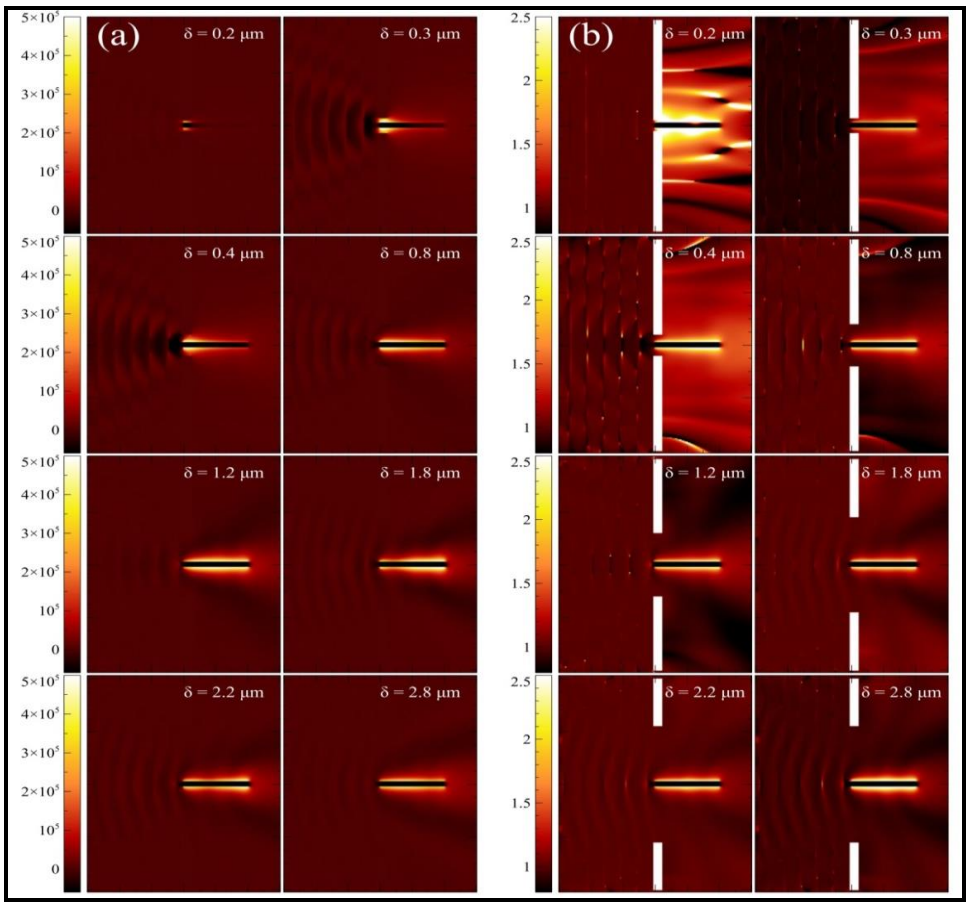


Figure 4 (a) Calculated difference between field amplitude distribution with and without the nanowire (b) Normalized field intensity distribution. Field intensity with the nanowire was divided by the field intensity without the nanowire. Top two images show some calculation artifacts since for the areas far from the center the field without nanowire is almost zero. Therefore, normalization relative to the almost zero fields significantly magnifies very low differences. In areas around nanowires the field is always present, therefore the normalization is not sensitive to artifact.

### 2.6 Future Work

The next step would be to fabricate the nanoscale endoscope using the optimized design as discussed above. Based on the conducted simulations, different coupling metal structures can be fabricated on top of the optical fiber. Multiple metal films with different thicknesses can be tested. The device can be fabricated in the fabrication flow shown in Figure 5.

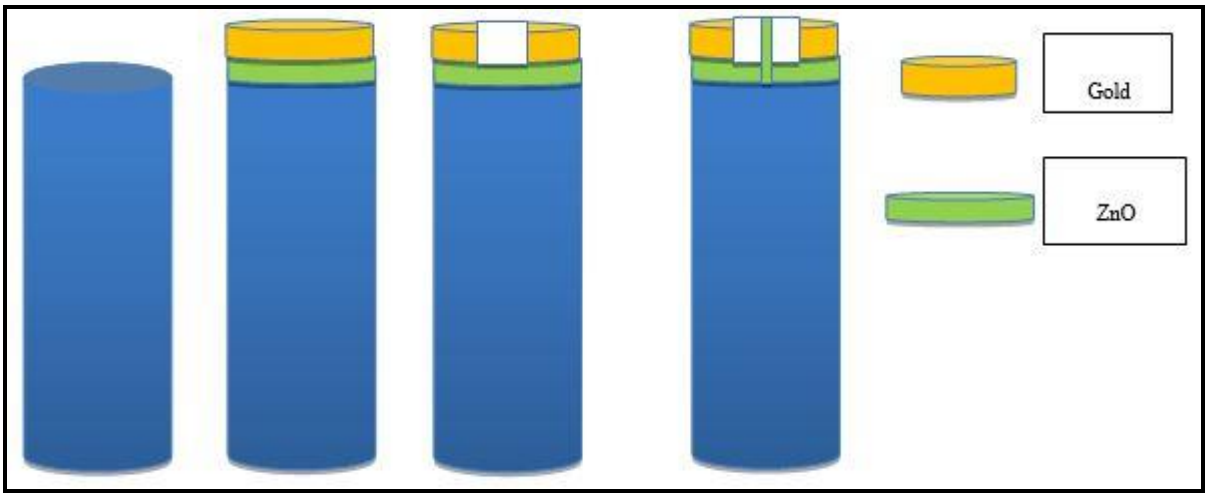


Figure 5 The proposed fabrication steps of single cell endoscope. (a) Optical fiber (b) ZnO (optional) and gold deposited on the fiber (c) Patterning of metal (d) growth of single ZnO nanowire.

Large number of optical fibers can be placed into sputtering machine for parallel metal deposition. Then metal on top of an optical fiber interface can be patterned using multiple techniques and the most reproducible and suitable technique for mass production can be used. There are several established methods for fabricating structures on top of an optical fiber [59,88-92]. A simple and rapid epoxy-based method for transferring photonic crystal (PC) cavities to the facets of optical fibers, which basically allows gluing the structure to the fiber interface and then removing it from the substrate [59,90]. Subtractive patterning can be done via Chemical Lift-Off Lithography [91]. Metal deposition on the cleaved fiber interface followed by e-beam [92] or FIB patterning can be used to directly create patterned metallic structures. The metallic structures created with FIB can be later mass-produced using the innovative align-and-shine technique for series production of photolithography patterns on optical fibers that allow repeating of the pattern using a combination of photolithography and alignment provided by a regular fiber splicing system [93]. FIB or e-beam lithography can be used to create the master pattern and then use the *align-and-shine* technique to duplicate it.

The second step will be to grow single nanowire in the opening in metal. Hydrothermal growth of ZnO nanowires is a well-established technology. In Figure 6, ZnO nanowires were grown using this technique on an optical fiber to show that possibility. The seeding layer was grown via sputtering. Growth of the nanowires is very sensitive to the substrate: while dense growth requires thin ZnO seeding layer deposited on surface small number of isolated nanowires can be grown on the core of the optical fiber. The goal should be to grow just one nanowire in desired location.

Several configurations can be tested. The first will require sputtering of a ZnO seeding layer under the metal. Then opening in metal will provide access to the seeding layer where after hydrothermal growth ZnO nanowires will be located. In order to decrease density of the nanowires in the opening, another design might be to just grow the nanowires on glass fiber in the metal-free opening. Alternative approach could be using the patterned metal structure on top of the optical fiber as plasmonic tweezers that have been demonstrated previously for very similar configurations [94]. After that trapped ZnO particle will be dried on the surface of the optical fiber and heated for some duration at a specific temperature to ensure reliable contact with the fiber. Next the hydrothermal growth step can be conducted, and the nanowire can be grown selectively from the seeding nanoparticle. One of the possible approaches is plasmonic tweezers capturing ZnO nanoparticles that will serve as seeding for the following nanowire growth. Additionally fiber thinning technology might be used in order to create smaller area closer to the interface with the nanowire. Controlled dipping and pulling fiber tip out of HF creates very well predicted conical shape.

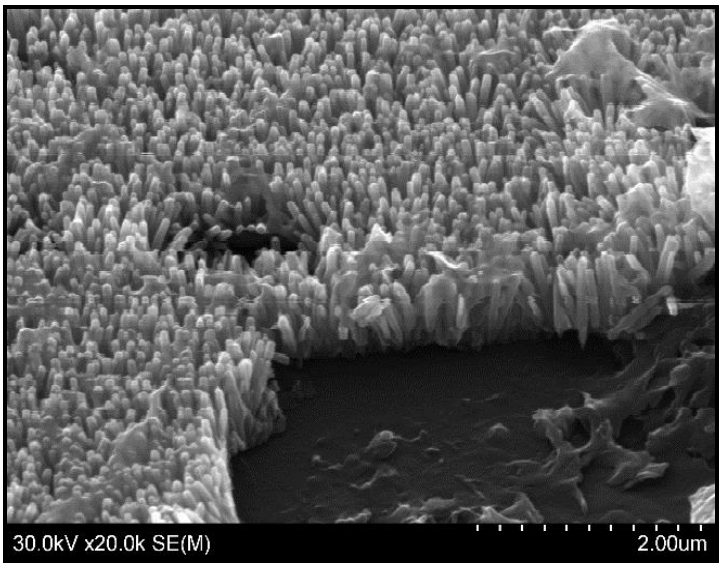


Figure 6 Synthesis of ZnO nanowires. Vertically aligned ZnO nanowires of approximately 0.7 um length have been grown on the optical fiber core.

## 2.7 Conclusion

A new design and FDTD simulations for a nanowire-based intracellular endoscope are presented based on a combination of an optical fiber and a nanowire. The fiber can be used as is, freshly cleaved, without applying any thinning techniques. A thin film of a metal deposited on the tip of the fiber and then milled aids better coupling of light into the nanowire and focusing of light in the vicinity of the tip of the nanowire, effectively decreasing excitation volume and increasing power density. Series of simulations were performed in three dimensions, the resulting distribution of electric field was analyzed to determine the optimal conditions at which better coupling of light from the fiber to the nanowire occurs. Also, the distribution of field amplitude and intensity was analyzed in terms of local contrast vs. total light intensity in close proximity to the nanowire. Conditions, optimal for two possible scenarios of measurement (maximized contrast, maximized local intensity) were determined. It was observed, that with opening of subwavelength size the light transmission through the opening was either low or

negligible depending on the size of the opening. Local field enhancement was observed inside the opening in the metal due to plasmonic enhancement [85,87]. With introduction of the nanowire to the simulated configuration the light starts propagating through the nanowire, providing high contrast in the vicinity of the tip of the nanowire. It was shown that the coupling is optimal, and the excitation volume is minimal with the radius of the metal opening to be 0.4 μm. To summarize, the proposed instrument platform gives a researcher a flexible tool for future intracellular study, specifically for high spatial resolution intracellular spectroscopy where high local contrast is required, and photo-activated payload delivery, where maximum power delivered inside the cell is critical. Towards the end of the chapter, several fabrication ideas have been proposed that can be utilized to realize the technology. In the next chapter, an optical fiber based nanoendoscope is discussed.

# CHAPTER 3: NANOFIBER BASED SINGLE CELL ENDOSCOPY: DESIGN AND FABRICATION

## 3.1 Introduction

The nano endoscope presented in this chapter has important advantages of traditional single cell endoscope [58]. It is minimally invasive and has ability to sense inside single cells. Additionally, the device addresses two important challenges mentioned in the previous chapter. The first challenge is that the existing single cell devices have extensive manual processing during fabrication. This step makes them irreproducible. The device reported here is reproducible and has an ability to be mass produced. Secondly, all the fiber based devices reported in the earlier chapter use microscope objective coupled with detectors such as photo multiplier tubes or avalanche photo-diodes, and spectrometers to detect the optical signal. This not only makes the entire setup expensive but also limits their application to *in- vitro* analysis exclusively. The nano endoscope presented here does not need microscope objective for signal detection, since it has the ability to locally collect signals from biological specimen.

The nanoendoscope was fabricated from silicon dioxide fibers. They are tapered in shape with profile diameters 8 microns at the waist to below 200 nm at the tip. They can be easily be produced in large quantities, are minimally invasive, allow single cell manipulation, and has the capability to simultaneously transmit and receive optical signals from intracellular organelle without the use of external detectors. This technology permits efficient and cost effective single cell organelle analysis, *in- vitro* and *in- vivo*.

The nanoendoscope tip is was designed using FDTD simulations. Initially FDTD simulations of light emerging from a tapered nanoendoscope tip were conducted. Following this, the nanoendoscope was fabricated. For reproducible fabrication, a detailed experiment to calculate the etch rate of silicon dioxide was designed and etch end point was estimated. Then multiple nanoendoscopes with different taper profiles were fabricated. A fiber holder cassette was designed and 3D printed to fabricate endoscopes in bulk. The fabricated endoscopes were characterized using scanning electron microscopy (SEM). Then an optical connection was established by splicing them to regular optical fibers.

After fabrication, the endoscopes were characterized for their transmission spectra and losses. Several experiments showcasing the forward light guiding properties of the nanoendoscope were demonstrated. These include shining light out of the endoscope under the microscope objective, illuminating fluorescently labelled micro beads and dye solution. Towards the end of the chapter, Viability of the endoscope on live cells is demonstrated using stained fibroblast cells and liver cell lines.

## 3.2 Methods

### 3.2.1 Simulations

The nanoendoscope taper profile optimization was conducted using FDTD simulations in commercially available FDTD software OPTI-FDTD solving simplified Maxwell's equations (eq.1-4) written with assumption that no conductive currents or charges are present in the system

$$\nabla \times E = -\mu \frac{\partial H}{\partial t} \qquad \text{eq. (1)},$$

$$\nabla \times H = \varepsilon \frac{\partial E}{\partial t} \qquad \text{eq. (2)},$$

$$\nabla \cdot (\varepsilon E) = 0 \qquad \text{eq. (3)},$$

$$\nabla \cdot (\mu H) = 0 \qquad \text{eq. (4)},$$

where $\mathrm{E} = \left[E_x(t,x,y,z), E_y(t,x,y,z), E_z(t,x,y,z)\right]$, is a vector describing the electric field strength, and $\mathrm{H} = \left[H_x(t,x,y,z), H_y(t,x,y,z), H_z(t,x,y,z)\right]$ is the vector that describes the magnetic field strength at a specific location (x,y,z) and time *t*. μ and ε are the magnetic permeability and dielectric permittivity respectively. A silicon dioxide fiber with a refractive index of 1.46 was modeled to have a taper radius that ranged from an 8 μm diameter base to a 200nm tip over a length of 30 μm, 44 μm and 59 μm (Figure 7). Green light, with a wavelength of 532 nm, was coupled into each respective structure and subsequently the shape of the outcome beam was analyzed.

### 3.2.2 Fabrication and Characterization

Following this, single cell nanoendoscopes of three different taper lengths 30 μm, 44 μm and 59 μm were fabricated from, cleaved single mode silicon dioxide 125/ 8 μm, fibers using a combination of traditional wet etching techniques [95,96]. The resultant tapered fiber tips were characterized using a HITACHI SU-70 scanning electron microscope (SEM) and then spliced to a regular single mode fiber using an IFS 10 arc fusion splicer to provide an optical connection with minimal loss. Further, optical transmission spectra and loses were investigated.

### 3.2.3 Cell Viability Experiments

Cell viability is an important quality for the single cell analysis device [26]. The device can be called minimally invasive if a cell is able to survive the probing of nanoendoscope with a minimal damage. This means the device must be biocompatible and small. The cell viability can be tested using different methods. In another study [97], the cell was probed with the nanoendoscope and was continuously monitored using the optical microscope for its behavior. It was shown that the cell had undergone mitosis after probing with the nanoendoscope thereby providing evidence of cell viability. In another study using photonic crystals [59], the nanobeam

was probed in a population of cells using live-dead cell kit. Long term effects of the nanobeam was studied after it was cleaved inside the cell and the cell was monitored the cell for several days. In another study [27], the calcium wave signalling due to mechanical disturbance caused by probing the cell with carbon nanotube endoscope was monitored. The signal was compared with those generated during probing with a glass pipette. It was shown that the carbon nanotube based nanoendoscope due to its small diameter induced less stress than the glass pipette.

In this study, three different types of viability experiments were conducted. In the first type, a nanoendoscope was placed inside the cell membrane and was kept in constant position while the cell was continuously monitored. The cell was stained with Live-Dead cell kit. Fluorescent images were taken at 5 minute intervals. In the second experiment, the nanoendoscope was placed inside the cell membrane similar to the previous experiment. Here, instead of leaving the nanoendoscope in a constant position, the probe was moved deep into the cell in precise steps at regular time intervals. The cell was stained with Hoechst and monitored continuously using video recording. In the third experiment, multiple cells (n=10) were probed briefly and were monitored after 24 hour time interval to observe the long term effects.

### 3.3 Results and Discussions

#### 3.3.1 Simulations: Design of Nanoendoscope

Light shining out of the nanoendoscope as a function of the taper profile optimization was simulated using FDTD simulations in commercially available software OPTI-FDTD. Figure 7 shows FDTD light transmission profiles of tapered fibers, with tapers consisting of an 8 μm base narrowing to a 200nm tip over taper lengths ranging from 30 μm to 59 μm. It is observed that the shape of the output beam is a function of the taper length. At a taper length of 30 μm, the transmission of light was very local and close to the apex.

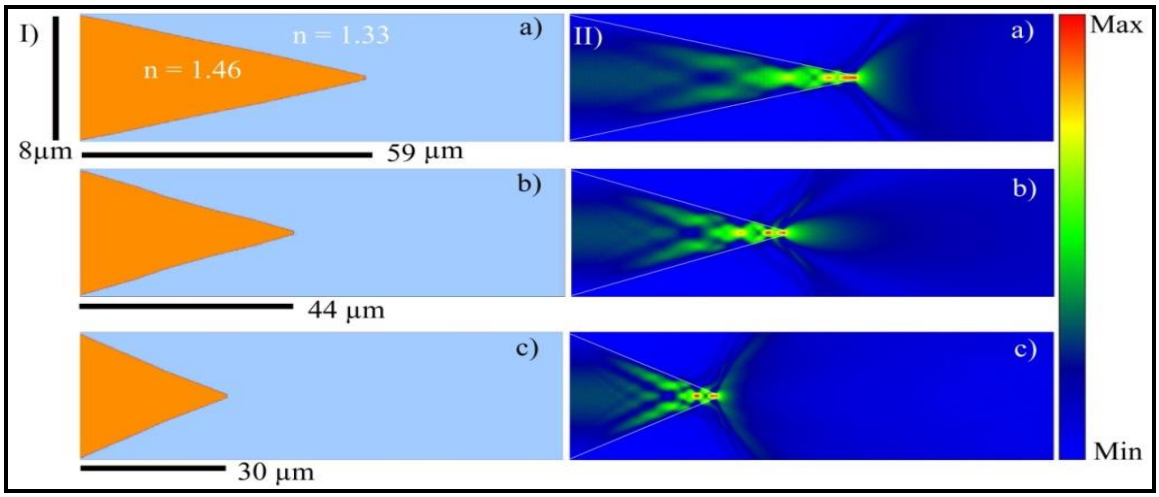


Figure 7 FDTD simulations of light coupling into nanoendoscopes tapered from 8 µm to 200 nm over different lengths (a) 59 µm (b) 44 µm and (c) 30 µm.

For the taper lengths of 44 µm and 59 µm, the mode propagating in the optical fiber was shown to be continuously squeezed along the taper of the nanoendoscope, before fanning out at the apex. For the 44 µm taper length, the transmission is focused over a distance of several micrometers from the apex; comparatively, the 60 um taper lengths emit an unfocused beam that spreads widely at a very short distance from the apex. The range of light transmission geometries allows for different tapered profile tips to be used for different applications. For example, a taper length of 30 µm can be utilized for an experiment that requires near field excitation, while taper lengths of 44 µm or 59 µm can be used for local fluorescent spectra collection inside single cells.

### 3.3.2 Fabrication of Nanoendoscope Device and Characterization

Following the design optimization, single cell endoscopes were fabricated using wet etching. The details of that process are shown in Figure 8. The circular glass fibers can be etched by dipping into HF solution. Upon insertion, the liquid forms a meniscus on the fiber, the height of which is a function of a fiber diameter [98]. As the fiber is etched, the height of the meniscus gradually decreases, thereby forming a tapered fiber.

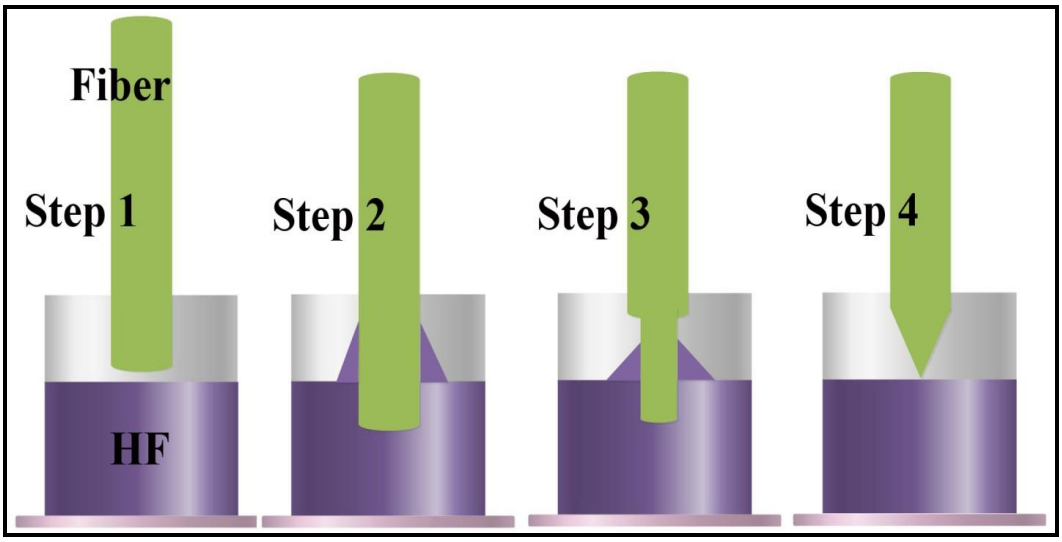


Figure 8 Schematic of the HF etching of optical fibers. Steps 1 to 4 indicate the various stages of the etching process.

The wet etching involves the following chemical reaction (eq. (5)). Several factors, such as concentration of HF, temperature of the reaction, dopants in the fiber, influence the reaction. They need to be considered during process optimization. If any of the factors are changed, separate characterization should be performed.

$$4\,HF + SiO_2 \rightarrow SiF_4 + 2H_2O \qquad \text{eq. (5)}$$

In order to detect the endpoint of etching, several freshly cleaved fibers were prepared and dipped into the HF solution as shown in Figure 9. Fibers were etched for different times (T1, T2, T3 so on) and characterized using SEM for identifying the etch end point. After identifying the endpoint, nanoendoscopes were then fabricated and characterized using SEM.

Figure 10 shows nanoendoscopes with tip diameter around 100 nm. The diameters ranged from 50 nm to 200 nm.

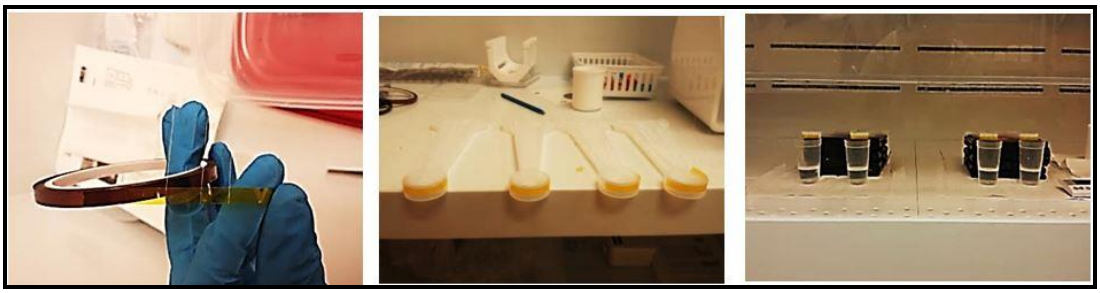

Figure 9 Various steps involved in fabrication of nanoendoscope. First, cleaved optical fibers are loaded onto the capton tape. Next tape with optical fibers is affixed onto a Teflon holder. Finally, the Teflon holder placed in solution of HF. The process is timed after insertion of holder with fibers into HF.

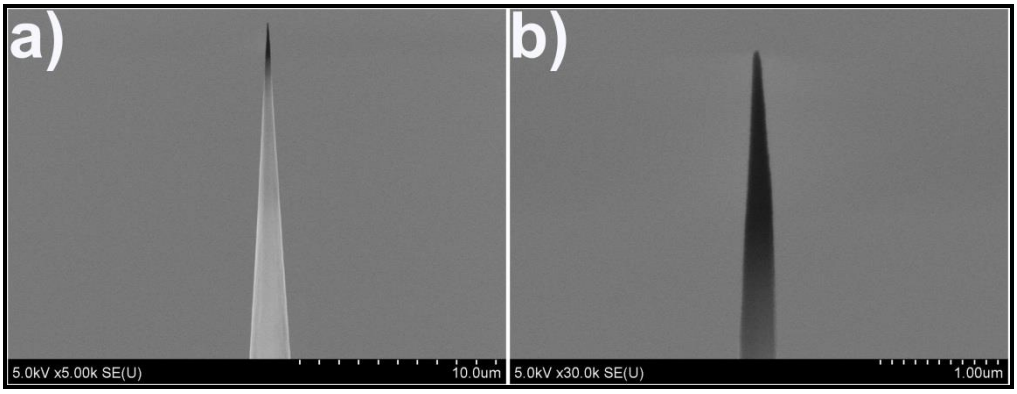


Figure 10 Scanning electron microscope images of wet etched fibers.

The variation arrives from the handling (timely removal) of etched fibers at the fabrication end point. Further control on the tip diameter can be obtained by reducing the HF concentration which will decrease the etch rate.

Following this, an experiment was conducted by increasing the etch time beyond the endpoint. Figure 11 shows the SEM images of the fibers etched for 43 min, 47 and 51 minutes in HF. They have taper lengths of 59, 44 and 30 micrometers respectively. These different shapes can be used for different applications as disused in FDTD design section. Thick fibers (small taper profiles) can be used for probing rigid cancer cells whereas, thin and long tapered fibers can be used for probing normal cells or living organisms like worms. The 44 micrometer taper

was used in all the experiments and further simulations due to its light guiding properties as discussed earlier.

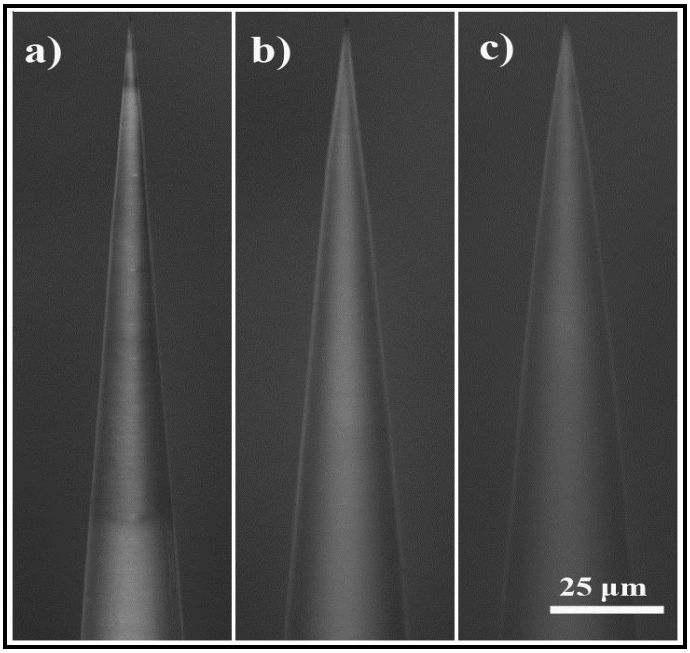


Figure 11 Different fiber profiles characterized by scanning electron microscope. Fibers etched in HF for (a) 43 min (b) 47 min and (c) 51 min.

Figure 12 Mass production of nanoendoscopes. (a) A 3-D printed cassette for loading fibers and holder. (b) Multiple (25) fibers loaded onto the cassette. (c) Holder with cassette inserted into HF for fabrication of nanoendoscopes. The process is timed after insertion of cassette holder into HF.

Following this, mass production of the fibers was conducted. The current fabrication technique as shown in Figure 9 provided an average of 4-6 fibers per loading.

Each loading took approximately 60 minutes from start (loading fibers) to finish (unloading the fabricated fiber). It would require frequent visits to the cleanroom for conducting several experiments with nanoendoscopes. In order to eliminate this problem, a 3D printed cassette for holding 25 fibers was designed and printed. It is shown in Figure 12 where multiple fibers (25) were loaded at once and etched in one run. This increased the yield of production and significantly reduced production cost for the lab. The fabricated nanoendoscopes were fusion spliced to the cleaved end of an optical fiber.

Figure 13 shows the process steps involved in fusion splicing. The length requirements have to be carefully met for successful splicing. The nanoendoscope now has two ports on two sides. On one end is the nano sized tip which can be used to probe single cells. The other is the optical connection end which can be connected to a laser source or a spectrometer. A Y-splitter can be connected to the optical connection end of the nanoendoscope and simultaneously connect the laser source and spectrometer. The completed nanoendoscopes were attached to an Eppendorf micro manipulator for nm resolution control movements of nanoendoscope during experiments.

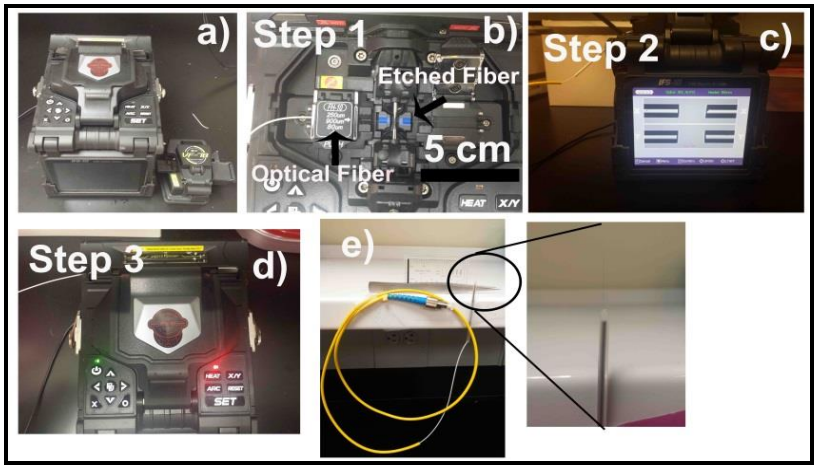


Figure 13 Splicing technique (a-e) for completing optical connection to the single cell nanoendoscope.

### 3.3.3 Transmission Characterization

In the next step, the nanoendoscope was characterized for a broad range of wavelengths. For analysis of transmission spectrum, broadband light was coupled into the optical connection end. Light was guided out of the nano sized tip of nanoendoscope (forward light guiding) and spectra were collected using a BaySpec spectrometer. Following this, light was back-coupled into the endoscope. This was done by placing the broadband light beam at the tip of the nanoendoscope. The spectra of forward and backward light guiding in the nanoendoscope are presented in Figure 14. It can be observed that light in visible range and near IR region is transported through fiber in both directions. This will enable its application in fluorescent spectroscopy of biological specimen.

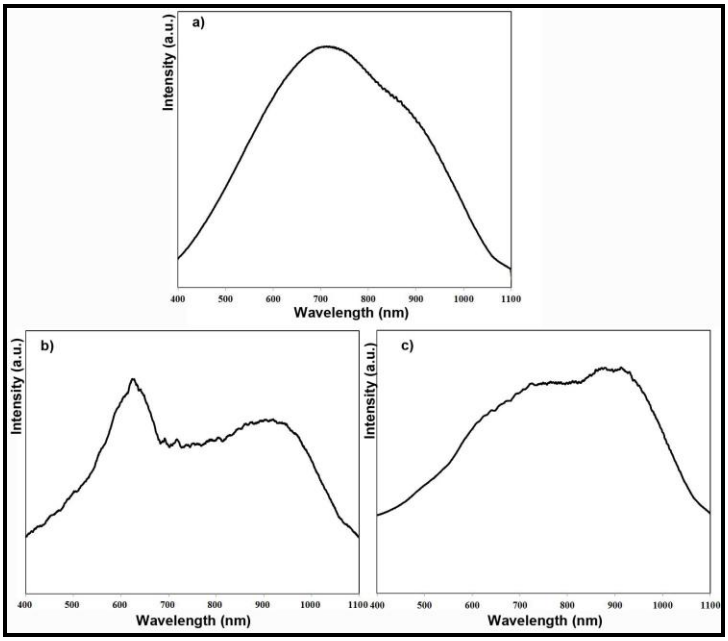


Figure 14 Transmission spectra plots of fabricated nanoendoscope. (a) Lamp spectrum (b) Forward coupling transmission of broad band light (c) Backward coupling transmission of broadband light source.

Following this, transmission loss (dB/ cm) of the nanoendoscope was estimated. Green light (532 nm) was guided though the nanoendoscope (forward and backward) as described

above and power was measured using a power meter. The transmission loss was calculated relative to the initial input power. The losses were plotted in Figure 15.

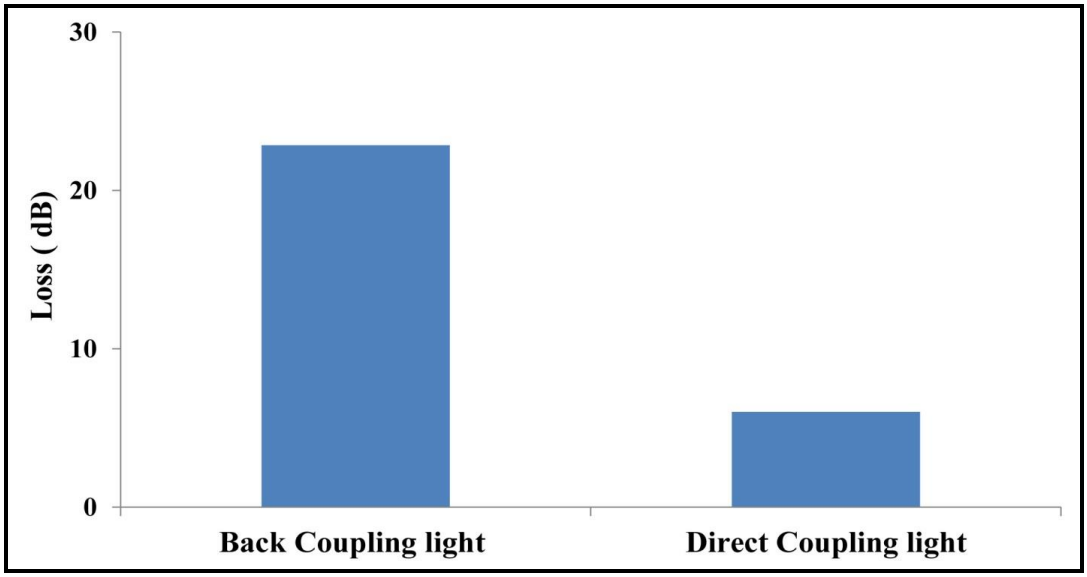


Figure 15 A plot of loss calculations for the fabricated nanoendoscope.

### 3.3.4 Forward Light Guiding Experiments

Following this, several experiments were conducted to demonstrate the forward light guiding properties of the nanoendoscope. Nanoendoscope was placed under microscope objective and forward light coupling was observed using 532 nm green lasers coupling into nanoendoscope. Figure 16 shows optical microscopy images of 532 nm light shining out of the nanoendoscope tip. The shape of the beam was very similar to the simulated beam shown in Figure 7 II (b) and the light propagates over a distance several micrometers from the apex, again, similar to the simulations. Following this, nanoendoscope was dipped into fluorescent a dye which was illuminated using forward light coupling and observed under the microscope.

Figure 16 II shows the excitation of a fluorescent dye when the nanoendoscope forward coupled with 532 nm light was dipped into the dye. It can be observed that the nanoendoscope is able to locally excite fluorescence in the solution.

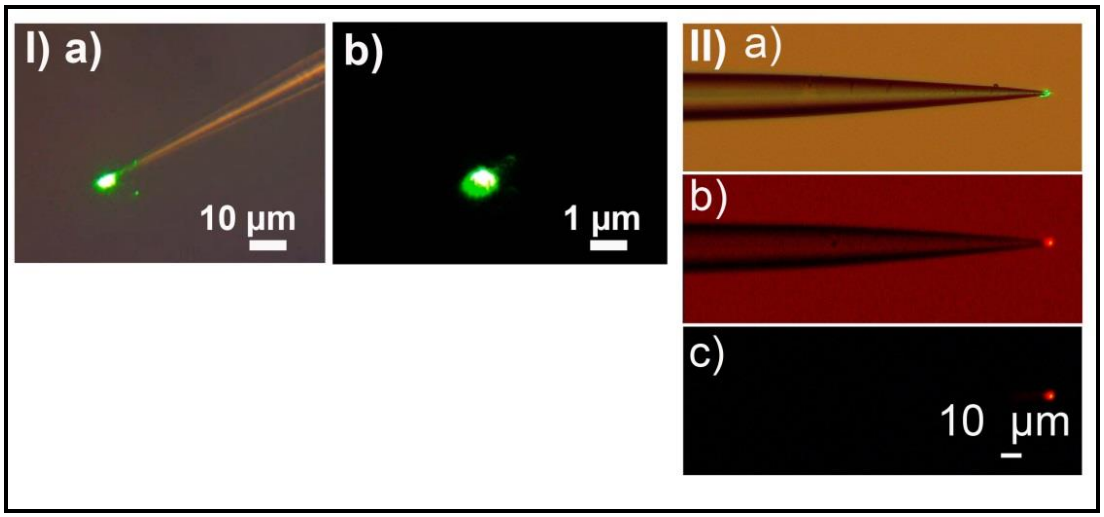


Figure 16 Forward light coupling of light into nanoendoscope. Part I) (a) and b) are experimental demonstration of 532 nm light coupling into the endoscope under microscope. Part II) A thin layer of fluorescent molecules was attached to its surface a) is green light coupling into the tip and fluorescence excited by light coupled into tip of the endoscope with microscope light on (b) and off (c).

Then it was used to selectively illuminate micron sized spheres coated with fluorescent dyes (procedure for synthesizing dye coated sphere is provided in the Appendix A). The nanoendoscope can be used to locally deliver light into small structures. In Figure 17 (a) & (b), small illumination volume of endoscope is used to excite fluorescence in an individual fluorescent bead.

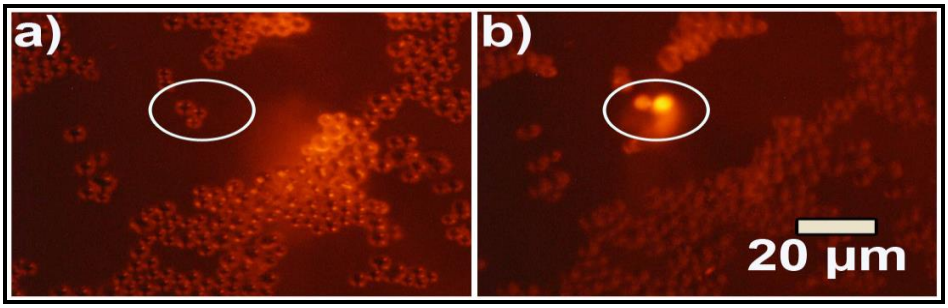


Figure 17 Forward light coupling of light into nanoendoscope on fluorescent samples. (a) Light is turned off and (b) light coupling into single cell endoscope and illuminating micron scale fluorescent bead.

### 3.3.5 Cell Viability

#### 3.3.5.1 Experiment 1

Figure 18 shows the bright field (a) and fluorescent microscopy images (b) and (c) of fibroblast cells that were probed with the nano endoscope. The cells were stained with live-dead cell kit. Live cells emit green light. The nanoenscope was inserted into the cells using micromanipulator and was kept in constant position. Fluorescent images were taken at 5 minutes intervals. Figure 18 (b) is the image taken at the beginning of the experiment (t=0 min). Figure 18 (c) is the image taken at 55 minutes from the start of the experiment (t=55 min). In the next cell viability study, the cell was constantly probed with the nanoendoscope and monitored under optical microscope.

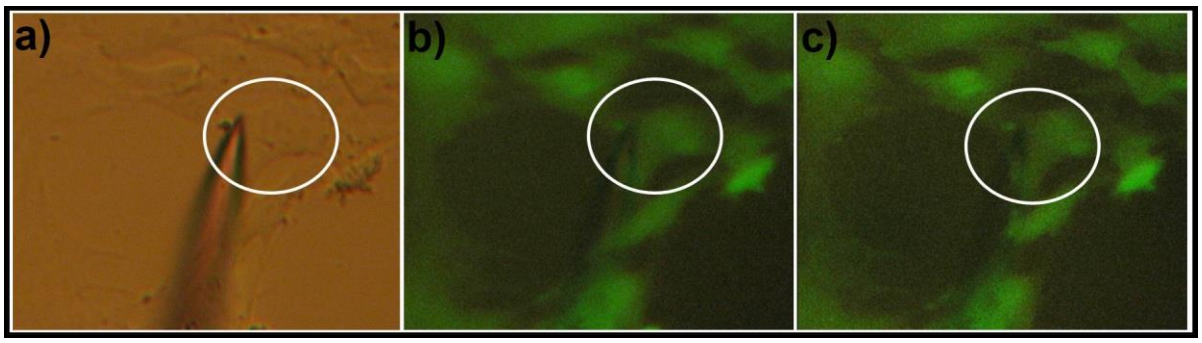


Figure 18 Investigation of cell viability with nanoendoscope. (a) Bright field image of endoscope inserted into single cell t = 0 (b) corresponding fluorescent image at t = 0 (c) fluorescent image of the cell at t = 55 minutes showing the cell is alive.

#### 3.3.5.2 Experiment 2

Figure 19 shows the bright field (a) and florescent images (b) of nano endoscope probed into a liver cell. The cell was approximately 20 micrometer thick according to the Z-stack images taken on a similar population of cells. In Figure 19 I (a) and (b) live cells can be observed before the nanoendoscope was inserted. Then, the cell was probed in Figure 19 II (a) and (b). In two successive steps, approximately 6 minutes apart, the cell was further probed. The endoscope was

inserted by 7 μm, Figure 19 III (a) and (b,) and then, 3 μm deeper, Figure 19 IV (a) and (b). During the entire experiment, video was continuously recorded and filters were alternated between bright field and fluorescent field. All the images were extracted from the video recording. At the final step, Figure 19 V (a) and (b) (z = 0 μm), the nanoendoscope was placed for next 30 minutes. Then the nanoendoscope was removed and cells were observed using fluorescent filter.

Figure 20 shows fluorescent images taken before and after the experiment. The images look identical indicating minimal damage to the cells after continuous perturbation for nearly 50 minutes. It can be observed that the cells remained viable after the experiment. This demonstrates that sensing inside thick cells, where deep penetration is required, can be achieved.

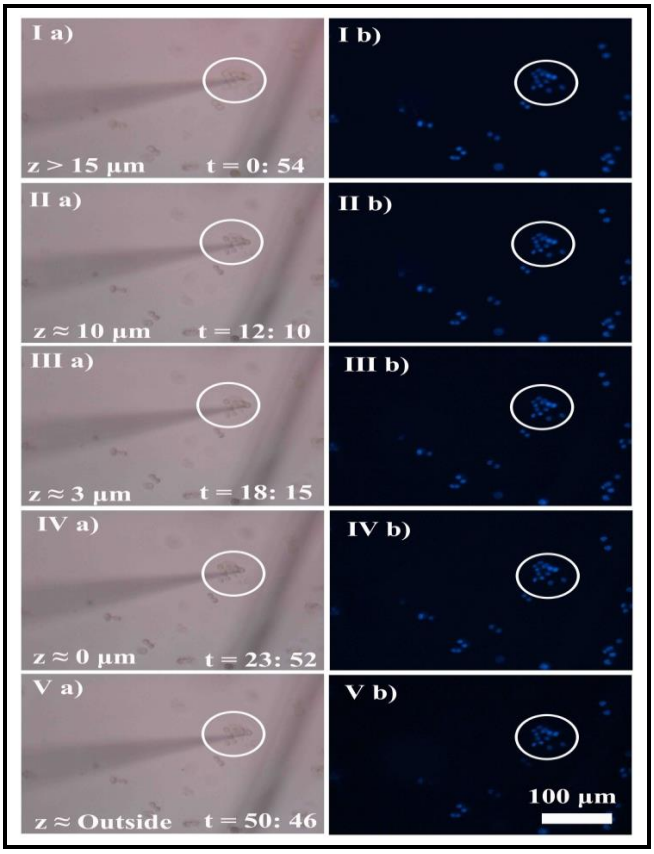


Figure 19 Experiment 2 of viability test. Continuous perturbation of liver cells with nanoendoscope to test their viability.

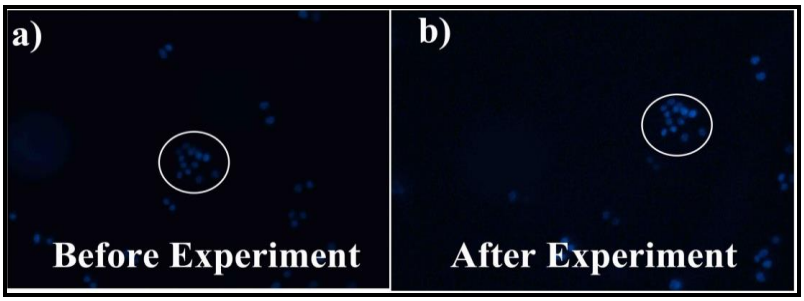


Figure 20 Hoechst stained liver cells observed (a) before and (b) after the viability experiment.

### 3.3.5.3 Experiment 3

In the next experiment multiple liver cells were probed once as shown in Figure 21 and analyzed after 24 hours to monitor any long term effects on these cells as shown in Figure 22. The cells were stained with Hoechst and cell tracker. Figure 22 shows a representative image of a cell (out of multiple cells) that was probed with the nanoendoscope. It can be observed that the cells were alive and healthy after 24 hours, their morphology looks good and they are fluorescent. This provides evidence that probing them once for a short time does not cause long term consequences. This also indicates that the same cells potentially can be probed multiple times. These experiments provide evidence that the nano endoscope is minimally invasive providing a platform for continuous monitoring or multiple analyses on single cells.

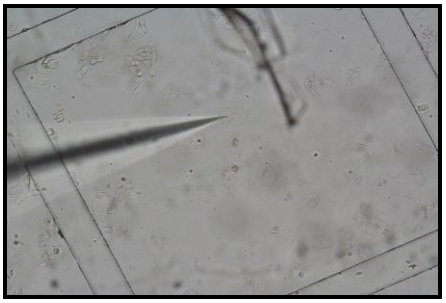

Figure 21 Experiment 3 of viability test. Probing cells with nanoendoscope. Multiple cells were probed and observed for 24 hours.

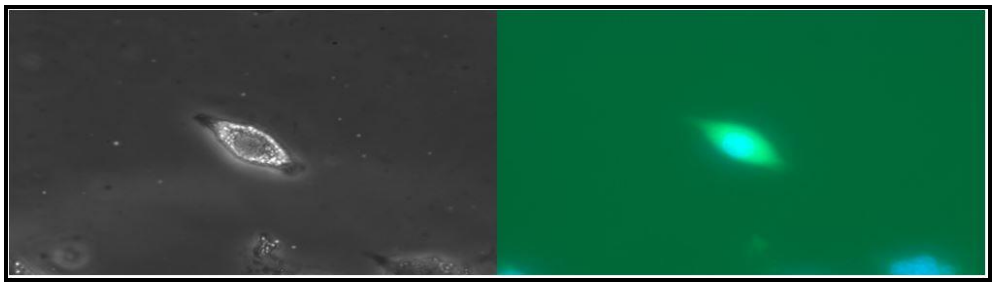

Figure 22 Representative picture of several cells observed for viability. (a) Bright field and (b) Fluorescent imaging of cells probed with the nanoendoscope as observed 24 hours after the probing.

### 3.4 Conclusion

In this chapter, a nanoendoscope has been introduced. First nanoendoscope design was optimized using OPTI-FDTD software. It was shown that a taper profile of 44 microns provided a focused beam of light that would be useful for sensing single cells. Following this, the nanoendoscope of three different taper profiles was fabricated and characterized using SEM. Then, a 3D printed cassette was used to increase the yield of fabrication. Following this, an optical connection was established to the fabricated nanoendoscope using arc fusion splicing.

Then, a series of experiments were conducted to characterize the light guiding properties of the nanoendoscope. Transmission losses of the nanoendoscope were first estimated. Then, light coming out of the nanoendoscope was observed under the microscope. Following this fluorescent dye and beads were illuminated showcasing the forward light guiding properties of the nanoendoscope.

At the end, the nanoendoscope cell viability was tested in three different scenarios. It was shown that the small diameter and taper profile are viable for prolonged and multiple analysis on single cells. The next chapter will focus on optimization of backward light guiding/ back coupling of light and experimental demonstration on single cells.

# CHAPTER 4: NANOFIBER BASED SINGLE CELL ENDOSCOPY: *IN-VITRO* AND *IN-VIVO* EXPERIMENTS

## 4.1 Introduction

In this chapter, FDTD analysis on light collection from fluorescent samples excited using external light and light coupling from the nanoendoscope itself, i.e. simultaneous excitation and collection of light, is first conducted.

Following this, experimental validation of optical light collection into the nanoendoscope was obtained by collecting spectra, first from fluorescent dyes and then using biological specimens, fluorescently labelled intracellular organelle of fibroblast and liver cell lines.

Next, simultaneous optical light delivery and collection was experimentally demonstrated first using fluorescent dyes and then using biological specimens MDA-MB-231cancer cells. These experiments demonstrated that fluorescent light can be coupled back through a nanoendoscope and the localized spectra from the interior of a cell can be acquired.

Finally, an intracellular fluorescent spectrum was collected *in- vivo* from live Caenorhabditis elegans worms.

## 4.2 Methods

### 4.2.1 Simulations

Back coupling simulations were conducted by placing a point source of light near the tip of the nanoendoscope and relocating the source in a 2D array of points to investigate efficiency of coupling at the different geometric locations. This was used to approximate the mechanisms

and properties used when collecting fluorescence from a sample excited by an external light source. Further analysis was then conducted to investigate the efficiency of the back coupling of light if measured while forward coupled light was simultaneously propagating through the nanoendoscope.

### 4.2.2 Experimental Validation

After these simulations, experiments that measured the light collected from fluorescent dyes, sub cellular organelle via the single cell nanoendoscope were conducted using two experimental setups. In the first setup, a human lung fibroblast cell was stained with Acridine orange and excited using an external light source generated by a built-in Nikon, blue excitation, fluorescent filter. The fluorescent emission signal was then collected using the nanoendoscope which had been inserted into nucleus of the cell. In the second setup, the nanoendoscope was inserted into an MDA-MB-231 cell that was stained with MitoTracker Red and then fluoresced using a green excitation light (532 nm) forward coupled into the nanoendoscope; simultaneously, the back coupled fluorescent emission signal was collected and measured using the same nanoendoscope. Following this, *in- vivo* experiments were conducted using *C. elegans* worms. Neurodegeneration model animals that stably express polyglutamine residues fused to Yellow Fluorescent Protein (YFP) in the body wall muscle (strain AM140, genotype rmIs132 unc-54p::Q35::YFP) [99], were anesthetized with 10 mM Levamisole, mounted on 2% agarose pads, and then probed with the nanoendoscope. The emitted spectrum was then collected by the nanoendoscope.

Figure 23 I (a-j) shows the back coupling of light into a nanoendoscope with the taper length 44 μm from a point source located at different distances from the apex of the tip. It is

observed that the coupling efficiency quickly decreases when the point source is moved from 0.015 µm to 3.0 µm away from the apex of the nanoendoscope tip.

### 4.3 Results and Discussion

#### 4.3.1 Simulations: Light Collection

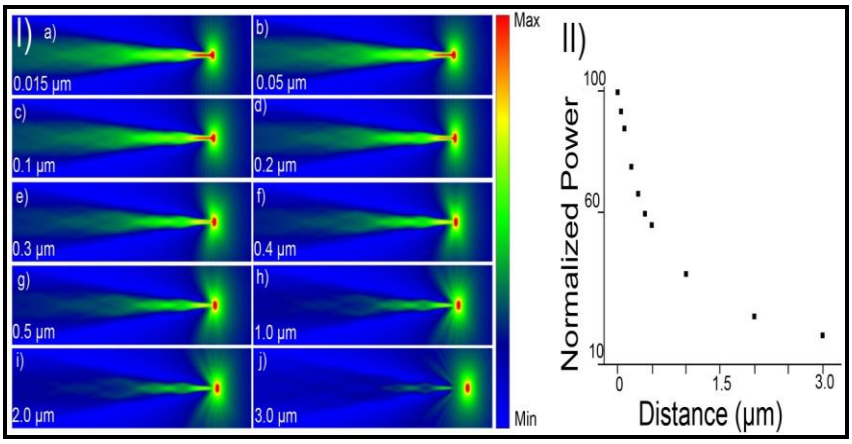


Figure 23 Nanoendoscope tip light collection characterization. Part I (a) shows FDTD 2D single cell endoscope tip tapering from an 8 µm diameter base to 200 nanometers at the apex of the tip over a distance of 44 µm with a point light source places at different distances from the tip from 0.015 µm to 3.0 µm. II) is the plot of normalized power with respect to 0.015 µm distance from the point source to the apex of optical fiber.

This information can be applied to a case when an external light source is used for the excitation of a fluorescent sample and a nanoendoscope is used to collect the intensity of the fluorescent signal. The relative intensity decreases from 100% at distance 0.015 µm from the apex to 40 % over a distance of 1 µm, Figure 23 II. In order to simulate the simultaneous forward and back coupling of light and to optimize the geometric position of the fluorescent source with respect to the nanoendoscope tip for effective back coupling, further analysis was conducted.

Figure 24 shows 3D plots of the relative power intensities for (a) forward (b) back and (c) the cross product of the forward and backward coupling. The center of the nanoendoscope is modeled at (x=0.0 µm, z=0.015 µm). The Z axis is parallel to the direction of the tapering tip of

the endoscope 8 μm base of the tip to the 200nm apex. The X axis is perpendicular to the axis upon which light propagates.

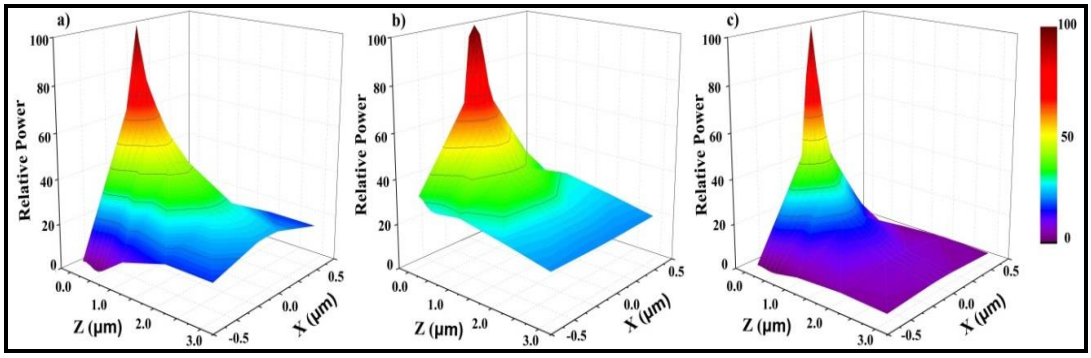


Figure 24 Theoretical optimization of light delivery and collection by the nanoscale endoscope tip. (a) Forward coupling of light (b) Back coupling of light (c) is a product of forward and back coupling intensities.

A 2D array of point sources around the single cell endoscope tip were simulated and light collection intensities were recorded, Figure 24 (b). Intensity of light transmitted in the endoscope was recorded these array of points and shown in Figure 24 (a). The height of the images is the light intensity. It can be observed that light transmission can work quite efficiently over several micrometers. The intensity of light relative to that at center (x=0.0 μm, z=0.015 μm) decreases from 100% to 30 % over a distance of 2 μm (x=0 μm, z=2 μm). On observing the relative intensity along the axis perpendicular to fiber, x-axis at z=0.015, the intensity decreases to 80% in 50 nm on either side of the fiber (x=0.05 μm, z=0.015 μm), to 65% in just 100 nm (x = 0.1 μm, z=0.015 μm), and to just 2% in 500 nm (x=0.5 μm, z=0.015 μm). Figure 24 (b) shows the intensity of signal collected by the tip from a point source located at different X, Z locations away from the endoscope. The intensity of light relative to that at center (x=0 μm, z=0.015 μm) decreases exponentially with distance indicating that signal will be highest when the tip is very close to the fluorescent source. It decreases to 56% in 500 nm and to 20% over a distance of 3 μm (x=0 μm, z=3 μm). Along X axis the intensity decreases to 66% after moving 100 nm from

center, to 31% at 500 nm (x=0.5 μm, z=0.015 μm). In order to simulate simultaneous forward and back coupling of light, the product of forward and backward intensities is calculated and shown in Figure 26 (c). Along Z axis, the relative intensity decreases from 100% at center axis location (x=0 μm, z=0.015 μm) to 45% over a distance of 300 nm(x=0 μm, z=0.3 μm). Along X axis at (z =0.015 μm), the intensity goes down to 42% at 100 nm (x=0.1 μm, z=0.015 μm). This demonstrates that when nanoendoscope is used for light delivery, the collection by the same nanoendoscope tip is very local and works efficiently only with 100's of nanometers. Thus detection of fluorescent signal combined with simultaneous delivery can be used for nanophotonic sensing of XYZ position of the fluorophore.

### 4.3.2 External Excitation: Light Collection Experiments

#### 4.3.2.1 Fluorescent Dye Experiments

Spectrum collection using external excitation was conducted first on a group of commercially available florescent dyes. Five fluorescent dyes—Fluorescein, Green Fluorescent dye, Bromfluorescein, Rhodamine 6G, and Rhodamine B, were excited using an external UV LED light. The endoscope was dipped into the solutions, and spectra were collected and analyzed using a spectrum analyzer. Figure 25 (a) shows the source spectrum and (b) to (c) show the spectra collected at the tip of the endoscope. Following this, mixtures of dyes Rhodamine 6G and Green Fluorescent dye, Fluorescein, and Rhodamine B were created and excited by external UV LED, and then spectra were collected. Figure 26 shows individual spectra resolved from mixture of dyes.

This demonstrates that the endoscope has broadband collection abilities, and that multiple fluorescent signals can be resolved. In the next experiment a fluorescent dye was excited externally using microscope light, as described earlier.

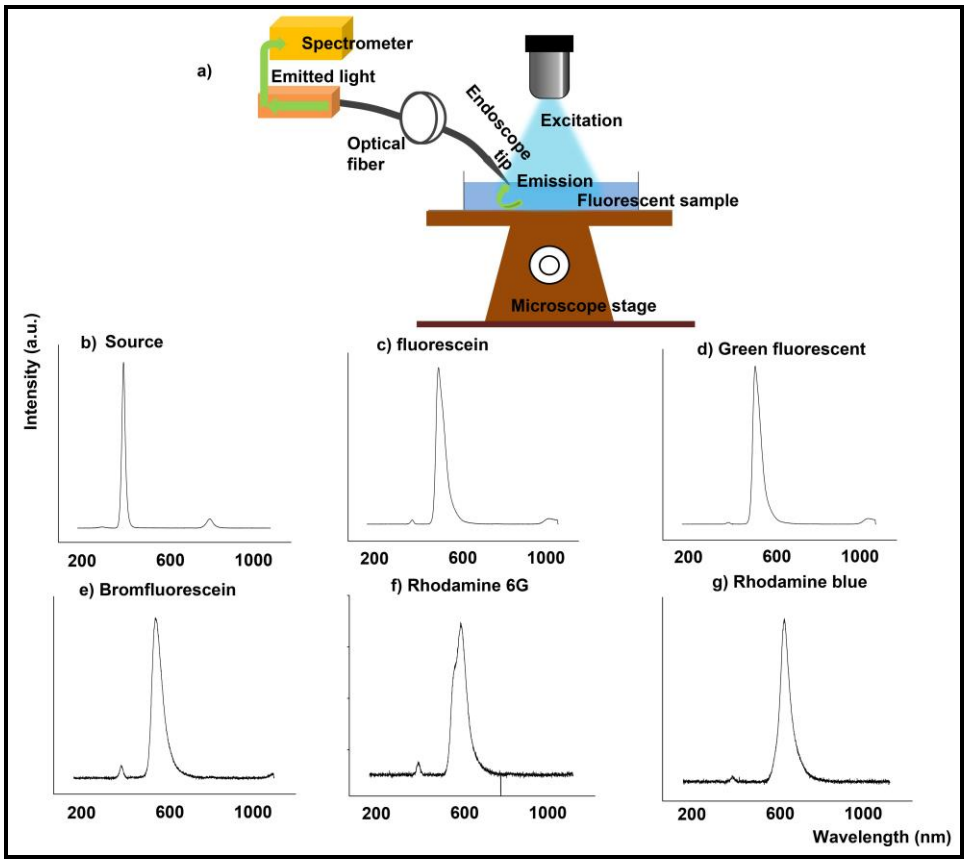


Figure 25 Light collection from fluorescent dyes. (a) Experimental schematic of light collection experiments from multiple fluorescent dyes (c-g). (b) is the spectra of the external source.

The endoscope tip was first placed ~3000 μm away from the dye solution and then was slowly moved towards its surface. The emitted light from the dye solution was continuously collected by the nanoendoscope tip and analyzed using the spectrometer connected to the nanoendoscope. The peak wavelength intensities vs nanoendoscope-dye separation distances were plotted in Figure 27. Black dots represent the excitation light and red dots represent the emitted signal from the dye solution. It can be observed that the intensity of signal increased as the nanoendoscope approached the dye solution. This can be used in future experiments for identifying the position of the nanoendoscope tip with respect to the fluorescent sample. Another interesting point is that the maximum intensity is observed just before the nanoendoscope was

dipped into the dye solution. When the endoscope was dipped into the solution (X axis distance ~ 4000 μm), the intensity of both the microscope excitation light and the corresponding emitted signal from the dye reduced. This could be due to the change in refractive index of the medium (from air to dye solution). The refractive index sensing capabilities of the nanoendoscope can also be utilized for automatic positioning of the tip inside different cellular regions or identifying the tip location.

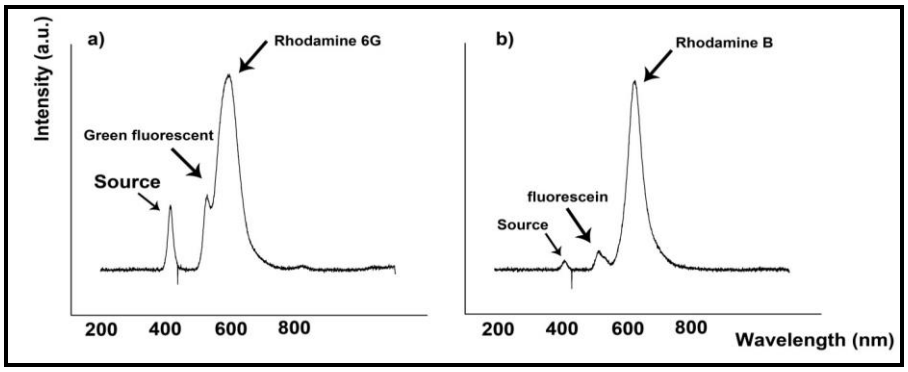


Figure 26 Spectra of light collected from mixture of fluorescent dyes. (a) & (b) different mixtures of fluorescent dyes excited by external light and emission signal was collected by the nanoendoscope.

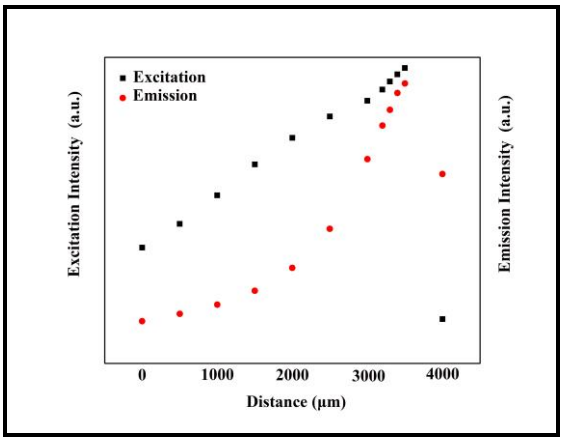


Figure 27 A plot of intensity vs. distance of nanoendoscope approaching a dye solution. The rise in intensity of emission (red) indicated the fiber is approaching the dye solution. A dip in both excitation (black) and emission (red) indicates the fiber enter the solution of dye.

#### 4.3.2.2 *In-Vitro* Spectroscopy: External Excitation

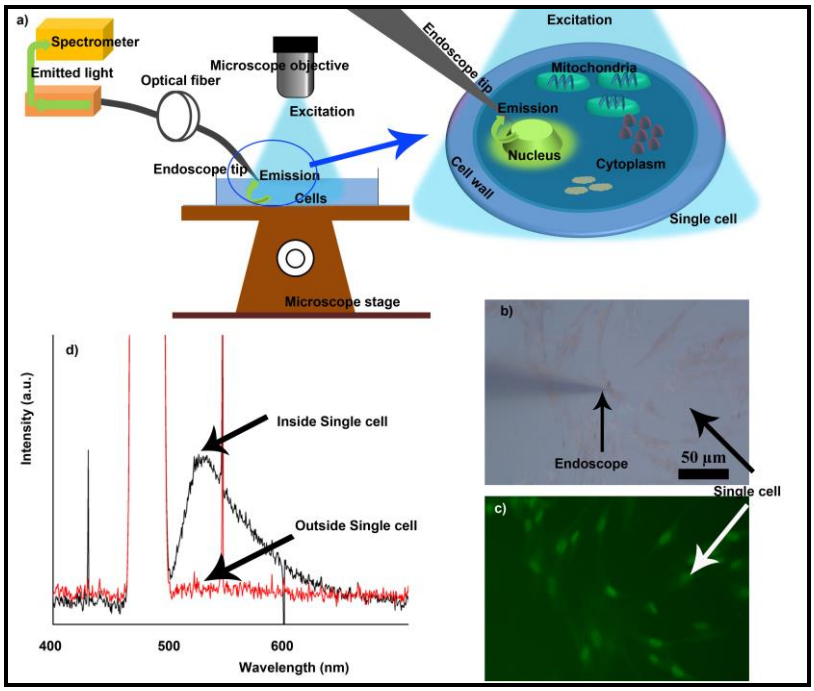


Figure 28 *In-vitro* spectrum collection using nanoendoscope from fibroblast cells. (a) Schematics of the experiment where internal microscope light source was used for fluorescence excitation. (b) A bright field image of the nanoendoscope inserted into a fibroblast single cell and (c) the corresponding fluorescence image. (d) The black curve is the spectrum (peak ~ 525 nm) from single cell collected from single cell endoscope and red line is when it is outside the cell.) of Acridine orange stained fibroblast cell. The nanoendoscope was after insertion into the cell.

Figure 28 summarizes the fluorescence spectra obtained from the excitation of a single fibroblast human lung cell stained with Acridine orange. Figure 28 (a) shows the schematics of the experiment. The nanoendoscope was inserted into the cell using a high precision 40 nm step resolution micromanipulator that was controlled using custom made software. The cell nuclei were labelled with Acridine orange which has a fluorescence absorption peak at 490 nm and an emission peak at around 525 nm. This absorption peak required a built-in Nikon, blue excitation, fluorescent filter which was used to generate the needed excitation wavelength with a broadband LED. As the cell emitted the fluorescence signal from its interior, the nanoendoscope at a close proximity to the organelle, Figure 28 (b), (c) collected the spectrum. Figure 28 (d) shows the

emission peak (black) at 525 nm for Acridine orange in a single cell. There was an absence of the peak at 525 nm, Figure 28 (d), when endoscope was just outside the cell where the signal from the organelle was too weak for detection. Here the nanoendoscopes ability to collect the spectrum from sub-cellular organelle was demonstrated.

Next, live liver cells were Hoechst stained and probed with a nanoendoscope as shown in Figure 29 (b). Spectra were taken as the nanoendoscope was inserted into the nucleus of the cells. It can be observed in Figure 29 (a), that the spectral intensity increased as nanoenscope goes deeper into the interiors of the cell. No cell indicates background signal, z= 0 µm is when nanoendoscope initially penetrates the cell surface and z= 7 & 10 µm are signals obtained when nanoendoscope goes deeper into the cell by these distances. This difference cannot be perceived using conventional optical microscopy as seen in Figure 29 (c). The change in spectra closely resembles that observed in FDTD simulations. This technique can be used for high resolution imaging or to locate intracellular organelle.

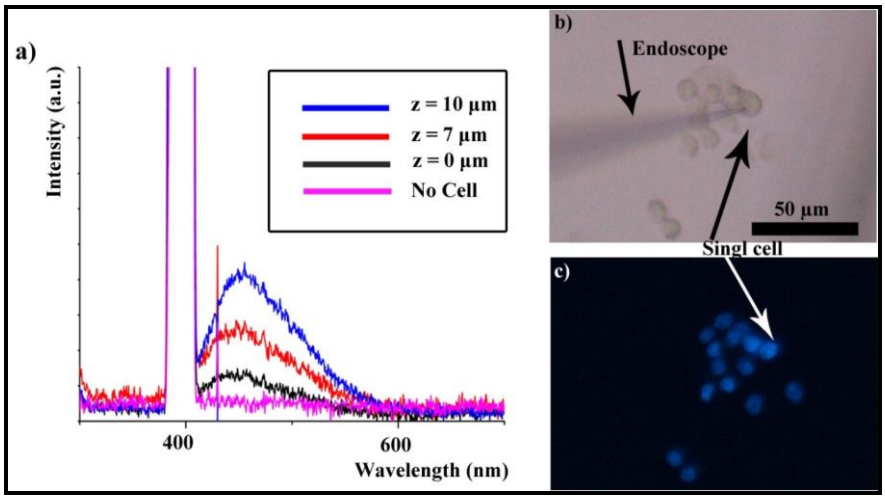


Figure 29 *In-vitro* spectrum collection using nanoendoscope from liver cells. (a) Spectrum collected from stained cells at different heights in the cell. No cell indicates background signal, z= 0 µm is when endoscope initially penetrates the cell surface and z= 7 & 10 µm are signals obtained when nanoendoscope goes deeper into the cell by these distances. (b) A bright field image of the nanoendoscope inserted into a live liver cell (c) the corresponding fluorescent image.

### 4.3.3 Simultaneous Excitation and Collection

#### 4.3.3.1 Fluorescent Dye Experiments

Spectrum collection was done using simultaneous excitation and collection of emission signal using fluorescent dyes (Figure 30). Three commercially available dye solutions were used in this experiment. Nanoendoscope was dipped into these solutions and excited with 532 nm light and emission was also collected and sent to a spectrometer using a Y-splitter as shown in the schematic Figure 30 (a). The emitted spectra from the dyes (b) Bromofluroscene (c) Rhodamine 6G and (d) Rhodamine blue was collected by the same endoscope tip and analyzed using the attached spectrometer.

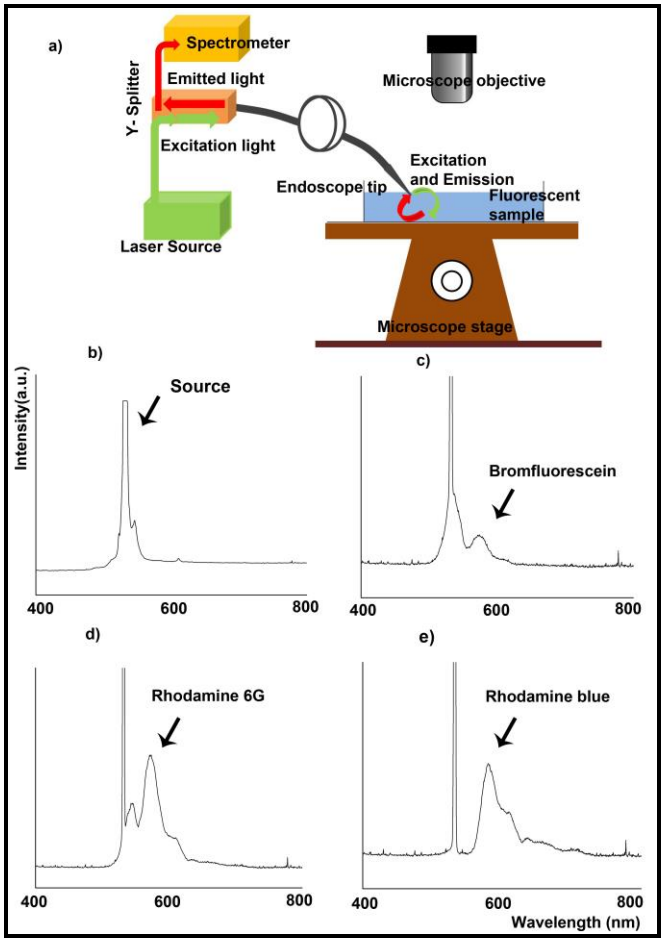


Figure 30 Simultaneous light excitation and collection of emission from fluorescent dyes. (b) spectra of the source 532 nm and (c-e) various dyes used in this experiment.

The spectra were continuously recorded as the nanoendoscope was moved towards the dye solution. It can be seen that the nanoendoscope is extremely sensitive to the distance from the fluorescent sample as shown in Figure 31. The spectrometer records intensity for all wavelengths (191 nm-1101 nm). The relative excitation intensity at each distance (step) in Figure 31 is the laser intensity measured at that step normalized with initial source power. The relative emission intensity presented in Figure 31 at each distance (step) is the emission wavelength intensity (577 nm) at each step normalized with the background signal at the step (191 nm). An increase in relative excitation intensity can be observed if the fluorescent signal intensity is higher than the background.

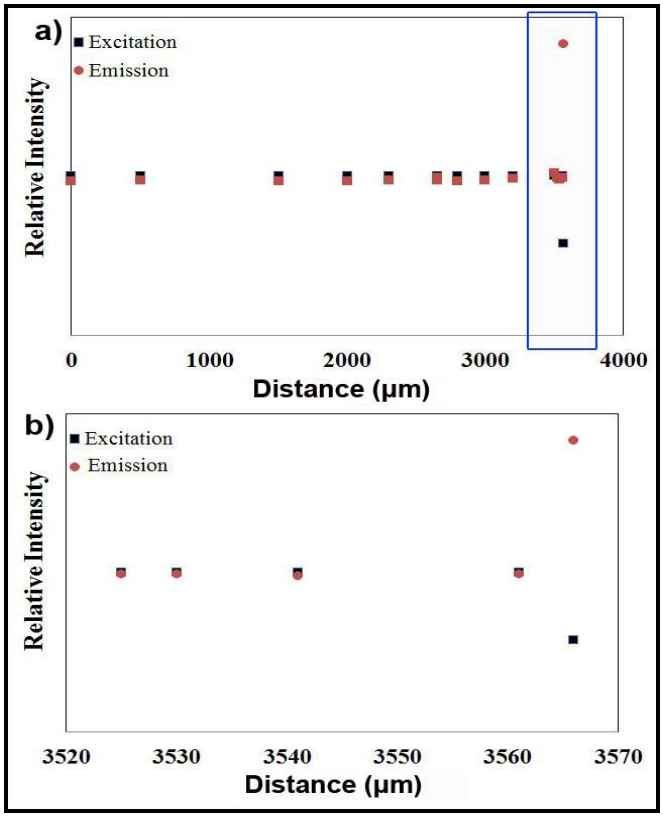


Figure 31 Simultaneous light excitation and collection of emission while approaching a fluorescent dye. (a) Relative intensity plotted against the distance from the dye surface. (b) A close up of the graph (a) highlighted by the blue box.

The fluorescent signal was only detected when the tip was near the dye solution (closer than 5 μm), as opposed to few thousand μm as observed in the external excitation experiment Figure 27. This shape of the curve is very similar to one obtained using the FDTD simulations.

#### 4.3.3.2 *In-Vitro* Spectroscopy

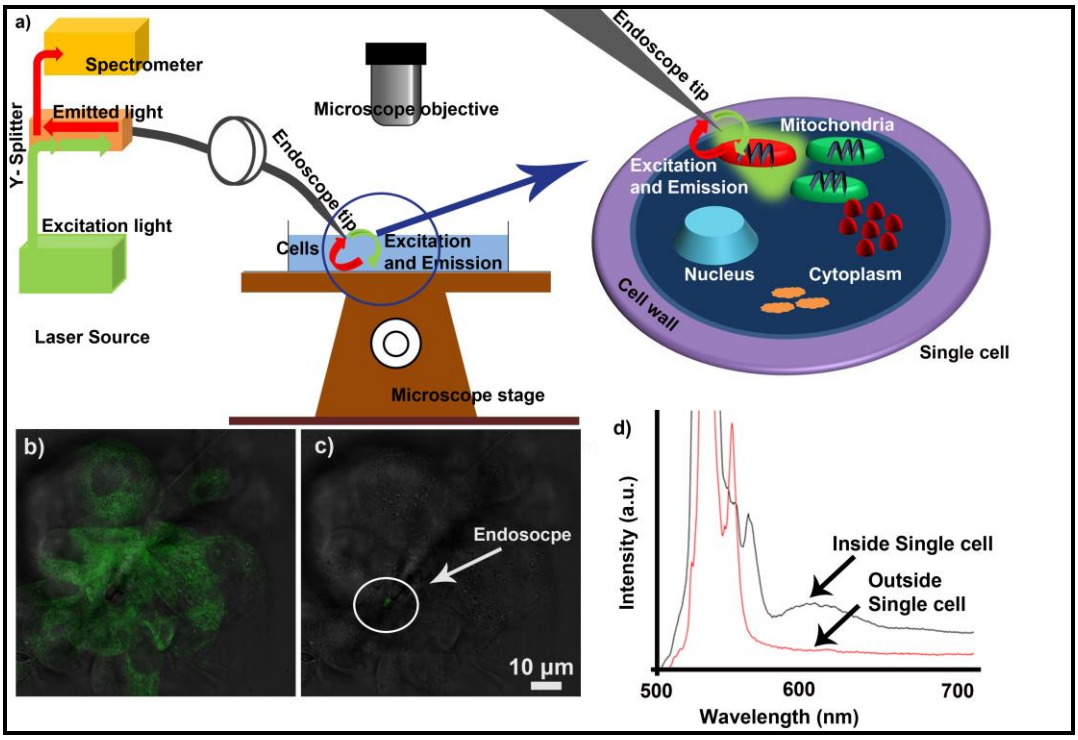


Figure 32 *In-vitro* simultaneous light excitation and collection of emission from fluorescently labelled cell. Fluorescent spectrum collected using configuration shown in (a) from a Mito tracker stained MDA-MB-231 cell (b, c) fluorescent image. (d) Red curve back reflection of the excitation signal (peak at 532 nm), Black – spectrum from inside a Mito-tracker-labeled cell (peak ~600nm).

Next, an experiment for the simultaneous delivery and collection of optical signals via the single cell nanoendoscope was conducted on live MDA-MB-231 cells that were stained with MitoTracker as shown in Figure 32 (a). The staining procedure is provided in the Appendix A. The expected value for excitation and emission were approximately 525 nm and 600 nm respectively. The single cell nanoendoscope was inserted into the cell by using a high precision control micromanipulator. The excitation source, a 532 nm green laser, was coupled into the

nanoendoscope via a Y splitter. Figure 32 (b) shows fluorescent image of the whole cell exposed to wide field excitation. Figure 32 (c) demonstrates local excitation of fluorescence using nanoscale endoscope delivering light into the cell. The fluorescence emitted near the nanoendoscope tip was coupled back and analyzed using spectrometer (Figure 32 (d) Black curve).

#### 4.3.3.3 *In-Vivo* Demonstration

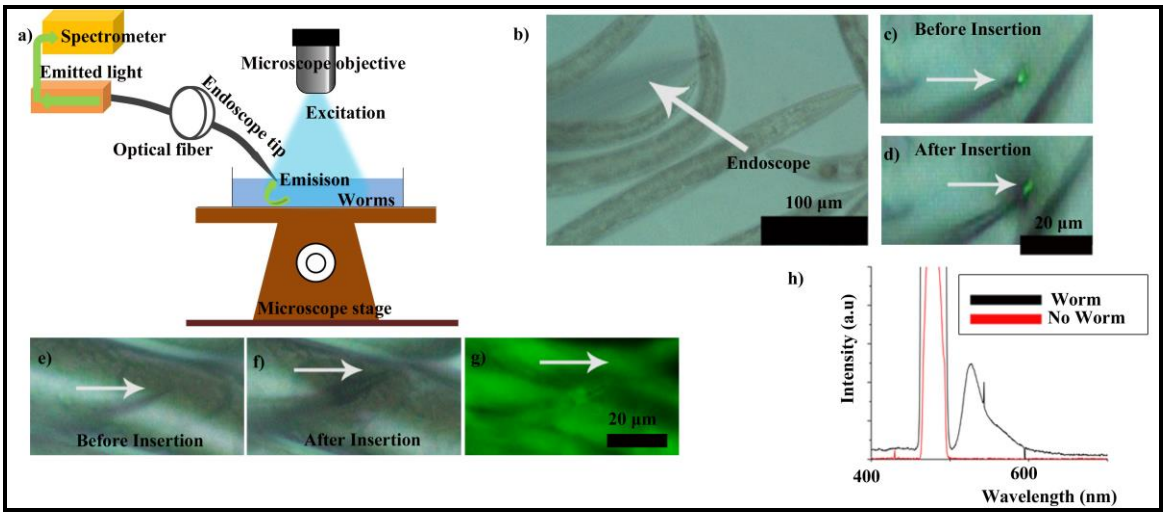


Figure 33 *In-vivo* fluorescent collection. The experiment was performed using the schematic shown (a) from C. elegans nematodes (AM140) shown in b). (c-f) Nanoendoscope during insertion (c) & (e) and after insertion (d) & (f). (g) is the fluorescence as observed under the microscope (h) is the collected spectrum via nanoendoscope.

Next, *in- vivo* experiments were conducted using *C. elegans* strain AM140, which harbors an integrated multi-copy neurodegeneration model transgene integrated into the genome. The worms fluoresce upon excitation with blue light and emit green signal at ~ 530 nm. The nanoendoscope was inserted into the worms as shown in Figure 33 (a-f). YFP was excited using an external microscope light and a spectrum was collected using the nanoendoscope (Figure 33 (a)). The spectrum from the *in- vivo* experiment shows a peak at 525 nm (Figure 33 (g)). This is the first time a nanoendoscope has been used to collect a fluorescence spectrum.

## 4.4 Future Work

The nanoendoscope will be applied for a number of single cell analysis experiments. These will involve decorating the tip with fluorescent dyes or drugs in conjunction with the sensing capabilities of the nanoendoscope to analyze the heterogeneous nature of single cells. The simultaneous forward and backward coupling ability will be utilized to perform further *in-vivo* analysis on worms and other organisms that still remain a challenge for biological community due to several limitations described in earlier chapter.

## 4.5 Conclusion

A single cell nanoendoscope that can simultaneously deliver and collect light on the sub-cellular level was fabricated. FDTD simulations of simultaneous light delivery and collection showed that the performance of endoscope depended on the location of the tip with respect to the fluorescent sample. Following the simulations, the nanoendoscope was shown experimentally to collect the spectrum from intracellular organelle in two configurations, using an external light source and light source propagating from the nanoendoscope itself. The nanoendoscope was inserted in a live multicellular organism and fluorescence was measured. This technology is an important step towards the realization of *in- vivo* analysis that eliminates the requirement of a microscope objective for signal collection.

# CHAPTER 5: ON CHIP WAVEGUIDE FABRICATION

## 5.1 Note to the Reader

Portions of this chapter have been published in Applied Optics 5745-5749 (2014) and have been reproduced here with permission from OSA.

## 5.2 Introduction

Optical waveguides are critical building blocks of on-chip photonics. Quality of an optical waveguide is largely defined by its optical loss. For straight polysilicon waveguides, absorption and scattering at grain boundaries [100,101], substrate coupling and radiation loss at etched waveguide sidewalls are the main sources of optical loss [102-104]. Therefore, thicker waveguide claddings can be used to minimize substrate coupling loss and fabrication can be optimized to decrease the surface roughness [100,105,106]. Photolithographic mask used for the waveguide patterning has to be printed with high resolution to reduce line edge roughness [107,108]. Additionally, post-processing methods can be used to make sidewalls smoother. They include gas phase oxidation [109], wet chemical oxidation [110], hydrogenation [101], resist reflow [111], end facet polishing [112] and related processes [113]. This requires introducing additional fabrication steps, increases error rates and cost of the fabrication process. Ideally, fabrication should be done using simple process with a small number of steps. Since etching of the waveguide is frequently done using one of the dry etching techniques, and capacitively coupled plasma reactors are still widely spread this study was conducted on optimization of the optical waveguide fabrication using this equipment.

Traditionally etching of planar waveguides is done using either inductively coupled plasma (ICP) with a passivation gas flow or electron cyclotron resonance (ECR) plasma [114-116], since they have high density of plasma, high directionality and higher power levels. However this equipment is very expensive and thus unavailable in many microfabrication facilities, while capacitively coupled plasma reactors are less expensive and more readily available, but were not previously used for this application [117]. Here the application of capacitively coupled plasma reactor is demonstrated for fabrication of polysilicon photonic waveguides with a low loss of 4.1 ± 0.6 dB/ cm by optimization of process parameters such as pressure and power using a careful design of experiments and observe 62% improvement in sidewall surface roughness of the fabricated waveguides for the optimal combination of parameters relative to non-optimized. The following sections describe the specific experimental procedures and the outcomes.

**5.3 Experimental Procedure**

The optical waveguides were fabricated on silicon wafers with $SiO_2$ used as a material for bottom cladding and polysilicon as a core material. Approximately 1 μm of $SiO_2$ was grown on two inch wafers in atmospheric furnace at 1050 ºC. Next, 1.2 μm of polysilicon was grown in a low pressure furnace at 605 ºC. AZ4620 photoresist was spin coated using Laurel Spinner. After spinning, the wafer was soft baked in the nitrogen furnace for 40 minutes at 90 ºC and re-hydrated in atmosphere for 1 hour before the photolithography was done on Quintil Q-2001C mask aligner. Then, the wafer was diced and etching experiments were conducted on dies from the same wafer to minimize variations between experiments.

The photoresist structure was first characterized using HITACHI SU-70 scanning electron microscope (SEM) and low surface roughness has been demonstrated. Initial silicon

etching experiments were conducted at power 100 W and pressure 100 mTorr with varying ratios of $SF_6$ and $O_2$ gas mixtures for optimization of the etch rate [118]. Then a set of experiments with different combinations of pressure and power were conducted in a parallel plate capacitively coupled 13.56 MHz RF Plasma Therm plasma reactor.

Table 1. The experimental design for optimizing the dry etching recipe for smooth waveguide sidewalls. There were 12 types of experiments for each combination of pressure and power. The total flow rate of gases was kept constant at 50 sccm for all the experiments.

| Pressure (mTorr) | RF Power (W) | | |
|---|---|---|---|
| 15 | 100 | 150 | 200 |
| 30 | 100 | 150 | 200 |
| 50 | 100 | 150 | 200 |
| 100 | 100 | 150 | 200 |

The fabricated waveguides were characterized using SEM and sidewalls roughness values were then estimated from the images. The optimal parameter determined based on outcomes of all the experiments were 30mTorr and 150W for pressure and RF power, respectively. Then a two inch wafer with $SiO_2$ cladding and polysilicon core layer was processed under optimal conditions. After that the wafer was cleaved and transmission losses of the fabricated waveguide were measured using cutback method [119].

**5.4 Results and Discussions**

According to [120,121], the radiation losses of a waveguide are proportional to the square of sidewall roughness. Therefore the goal of this study was to minimize the roughness as much as possible with the capacitively coupled plasma reactor set up. In order to optimize surface

roughness on nanometer scale all the fabrication steps were characterized using SEM. After deposition of layers of $SiO_2$ and polysilicon, the photoresist was spin-coated and patterned. Figure 34 shows SEM of the photoresist line cross-section with the width of 4.3 μm and smooth walls. Then, in order to optimize etching parameters, the first step was to find optimal gas chemistry. While $SF_6$ to $O_2$ are gases used in traditional Si etching recipes [118,122], further characterization was needed to understand the influence of gas flow ratios on etch rate and selectivity of the photoresist.

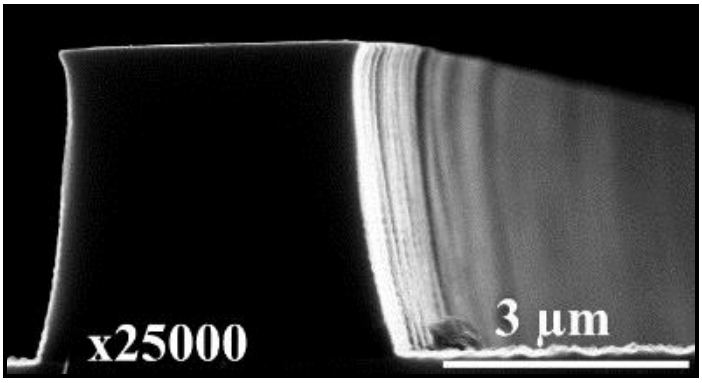


Figure 34 Photolithography optimization. Scanning electron micrograph of AZ4620 photoresist waveguide pattern taken after photolithography and before the etching.

Figure 35 (a) demonstrates the etch rate of the polysilicon vs the flow ratio of $SF_6$ to $O_2$. The maximum rates are observed for $SF_6$ concentrations between 80 and 90%. The low etch rates for lower concentrations of $SF_6$ can be attributed to lower effective temperature of electrons in the plasma while at higher concentrations it can be due to lowering of electron density [123,124] both of which influence the degree of ionization in the plasma chamber and the etching of polysilicon. At the same time, presence of oxygen can also be important for improvement of the etching efficiency by removing the polymer products formed during etching.

Another important parameter of the etching process that needs to be monitored for photoresist integrity is selectivity of etching of photoresist vs polysilicon. Figure 35 (b) shows

selectivity as a function of oxygen concentration in plasma and in the flow. While 100 % $SF_6$ yields maximum selectivity it corresponds to a very slow etch rate due to depletion of oxygen, therefore 90% concentration was used based on a trade-off between selectivity and the etch rate.

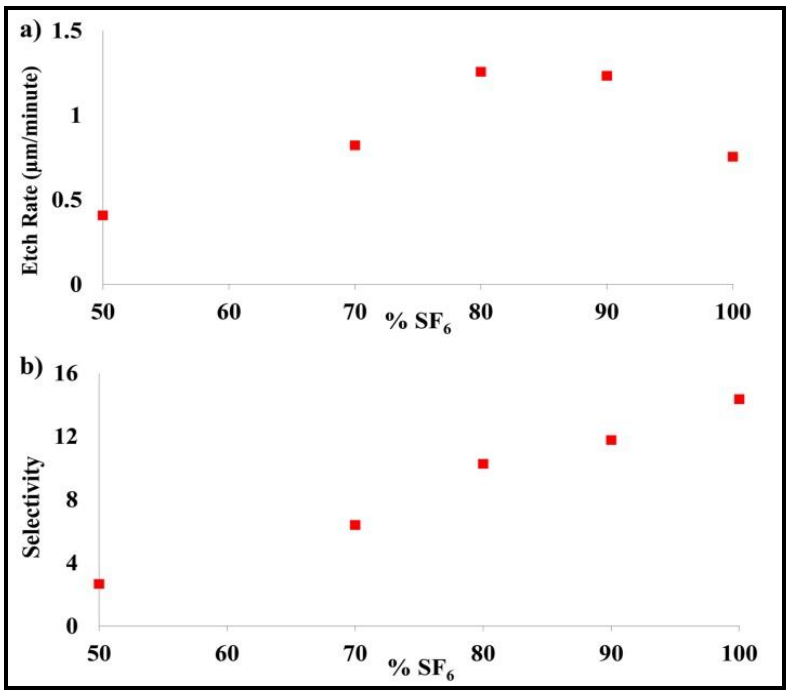


Figure 35 Etch gas composition optimization. a) The etch rate of polysilicon vs ratio of $SF_6$ to $O_2$. b) Selectivity of etching of polysilicon vs photoresist conducted at 100 mTorr pressure, 100 W power and 50 SCCM of total flow of gases.

The next step was to choose set of parameters for further optimization. Recently, fabrication processes using capacitively coupled plasma reactor have been studied [124-129], and the main parameters used in optimization were pressure, power and their combination. The experimental design of optimization based on these two parameters is presented in Table 1.

The pressure was varied from 15 to 100 mTorr for three RF plasma powers 100, 150 and 200 W and the corresponding surface roughness was estimated using SEM [115,130]. All the waveguides were imaged under identical conditions (Figure 36). The height variation ($Z_{ij}$) was determined from the SEM images at 9 different points of each waveguide. The estimations were

taken at identical locations across all samples in areas of the image where it was focused best. The roughness approximations were done at 3 different heights and 3 different displacement along the waveguide in a 3x3 square grid labeled $Z_{ij}$, where i=1 to 3 was changing along the waveguide and j=1 to 3 across the waveguide.

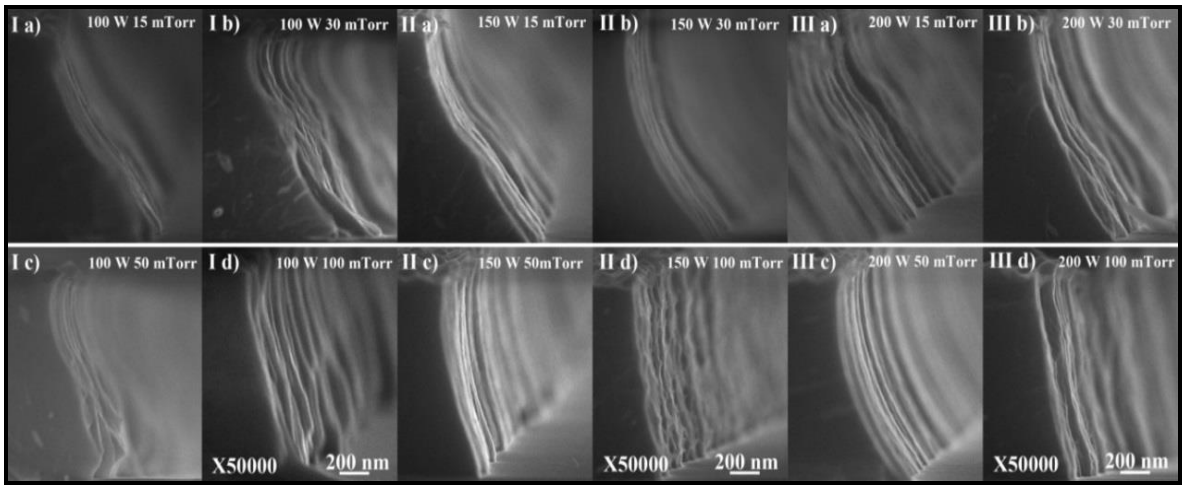


Figure 36 Waveguide etching sidewall characterization. Scanning electron micrographs of waveguides etched using experimental design presented in Table 1. I ) II) and III) correspond to 100 W, 150 W and 200 W power, respectively, and labels a, b, c, d are shown for pressures 15, 30, 50 and 100 mTorr.

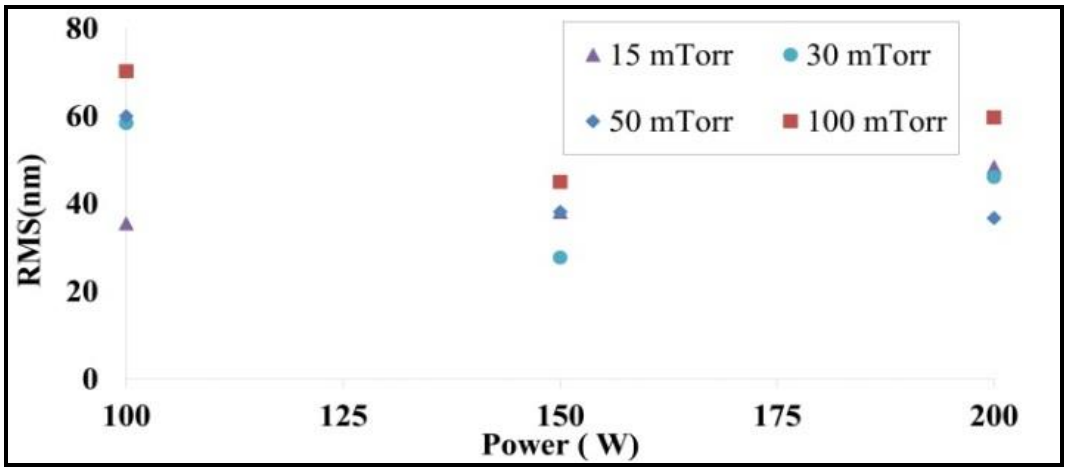


Figure 37 Plots of root mean square roughness (RMS) vs. the power of etch at all pressures in the experiment.

The estimated roughness values were calculated using equation 6 (m=n=3) and the summary of these results is plotted in Figure 47.

$$RMS = \sqrt{\frac{1}{m*n}\sum_{i=1}^{m}\sum_{j=1}^{n} Z_{ij}^2} \qquad \text{eq. (6)}$$

Further analysis demonstrates that for 100 W power (Figure 36 I) and pressure range 15-100 mTorr (a, b, c, d), at lower pressures the smoothness of the sidewalls is improved and at higher pressures the walls are more vertical. The estimated roughness is reduced from 71nm to 35 nm as the pressure is decreased from 100 mTorr to 15m Torr (Figure 37). Figure 36-II demonstrates the SEM images for higher power (150 W) and the same pressure ranges 15-100 mTorr (a, b, c, d). The roughness decreases as pressure is reduced. However, it can be noted that for 100 mTorr the sidewalls for 150 W are smoother (estimated roughness of 45 nm) than for 100 W RF (71 nm roughness). This may be due to the increase in etch rate, plasma density, ionization and dissociation of species at high powers [115,128]. For the power 200 W, decrease in surface roughness was also observed when the pressure was reduced from 100 mTorr to 15mTorr (Figure 36-III a, b, c, d). However, for the pressure 100 mTorr the surface roughness slightly increased (59 nm) in comparison with the value at 150 W (45 nm) due to higher acceleration of species in the plasma reactor. To summarize, it can be seen from the sidewall roughness summary in Figure 37 that for the capacitively coupled plasma reactors the optimal combination of the pressure and the power that gives the lowest surface roughness can be determined. For the constant power level, higher pressures increased roughness of the sidewalls. This can be explained by the fact that high pressure would block the products of etching from escaping. Decrease in pressure at constant power increases mean free path of reactive species in the plasma [131] thus producing smoother sidewalls. However, further decrease to much lower

pressure - 15 mTorr results in increased roughness possibly caused by enhanced ion bombardment [103]. In all the experiments with varying power, the pressures higher than 50mTorr resulted in rougher surfaces. The optimal combination of the pressure and power for the reactor setup was determined to be 30 mTorr and 150 W with the estimated roughness value of 27 nm. The non-optimized parameters resulted in surface roughness as high as 71 nm, thus proper optimization provides us with 62% of improvement. After determining the optimal parameters, the next step was to calculate the transmission losses of the fabricated waveguide and compare with losses for polysilicon waveguides fabricated using ICP reactive ion etching.

The measurements were done for the wavelength 1550 nm that has very low absorption loss in silicon. The overall absorption loss is influenced by the dimensions of a waveguide [100,132,133]. For example, a loss of 6.2 dB/cm was reported for a polysilicon waveguide width of 350 nm [134] and just 0.56 dB/cm was reported for a 10 μm width waveguide [135]. Since the width of our waveguide is 3.6 μm, the high quality waveguide should have a loss between those two values.

The losses of the waveguide fabricated using optimized conditions of our reactor, 150 W and 30mTorr, were studied using cutback method [119]. All the waveguides were fabricated with the same width 3.6 μm. Then they were cleaved at 3 different lengths $L_1$, $L_2$ and $L_3$. Coupling of light into waveguide was done from an optical fiber using high precision XYZ-stage while observing it under microscope as shown in Figure 38.

The output mode was monitored to ensure that the measurement was conducted for light properly coupled into the waveguide. The transmitted output power was measured directly by a power meter. For each length six measurements of the transmitted power were conducted.

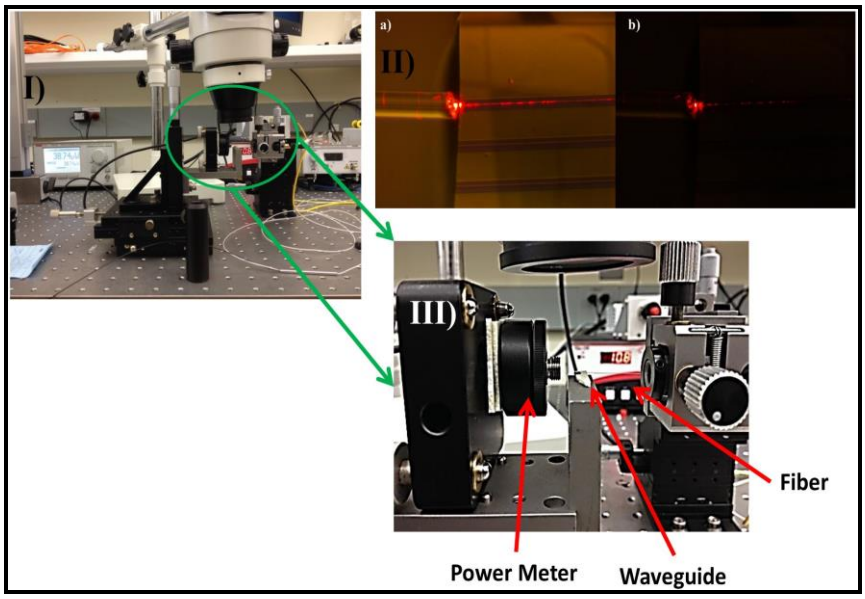


Figure 38 Experimental setup for loss testing of waveguides.

Additionally, direct measurement of light without any waveguides was used to determine the base power. Powers measured for each length $L_1$, $L_2$, $L_3$, were averaged to $P_1$, $P_2$, $P_3$, respectively and transmission loss coefficients were calculated for three sets of lengths, ($L_1$-$L_2$), ($L_2$-$L_3$), ($L_1$-$L_3$) using equation (7) [100] from where m, n are 1, 2 or 3. Finally, an average of those three values was 4 .1 dB/ cm with a standard error of ± 0.6 dB/ cm.

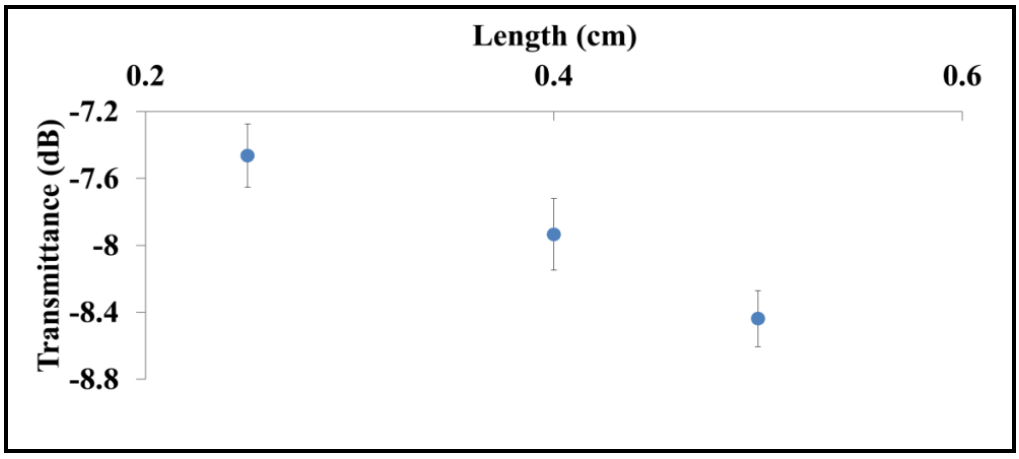


Figure 39 The measured attenuation of light (dB) after propagation in waveguides of three different lengths.

Figure 39 demonstrates transmission losses $T_1$, $T_2$, $T_3$ (in dB) corresponding to the averaged powers $P_1$, $P_2$, $P_3$ for 3 waveguide lengths.

$$a_{mn}\left(\frac{dB}{cm}\right) = \left(\frac{10}{L_m - L_n}\right) log\left(\frac{P_m}{P_n}\right) = \left(\frac{T_m - T_n}{L_m - L_n}\right) \qquad \text{eq. (7)}$$

## 5.5 Conclusion

Here application of capacitively coupled plasma reactor for fabrication of polysilicon optical waveguides with smooth sidewalls was demonstrated and several levels of optimization of multiple fabrication parameters were described. First, the influence of the flow ratio of $SF_6$ to $O_2$ gases was studied and the optimal ratio was found to be 90%/ 10%. Next, optimal combination of the pressure and power was determined to be 30 mTorr and 150 W with a very low estimated surface roughness value of 27 nm. Additionally, the fabricated waveguides have a low propagation loss 4.1 ± 0.6 dB/ cm. This demonstration of the use of capacitively coupled plasma reactor for polysilicon waveguide fabrication would potentially enable work of silicon photonics in larger number of universities possessing this equipment. In the next chapter a potential application for the low loss polysilicon waveguide is described.

# CHAPTER 6: BLOOD COAGULATION SENSOR DESIGN

## 6.1 Introduction

Measurement of the speed of blood coagulation is required for a large portion of the population. Nearly 80% of patients with diabetes die due to excessive blood clotting [136,137]. Malfunctioning of the coagulation system results in multiple disorders, ranging from ones with increased bleeding, such as hemophilia, to unwanted clot formation, and as a result - heart attacks and strokes [138-142]. Anticoagulant medications are taken regularly by more than 2 million patients in the U.S. [143,144], and it currently requires periodic dose adjustments and visits to the hospitals. There is a need in a device that can be used to monitor speed of blood coagulation at home, frequently, using small volume of blood obtained using fingerprick, at low cost and easily operated by non-professional.

There are several traditional approaches to the testing of speed of blood coagulation: prothrombin time (PT) that can be done in hospital [145,146] or at home using portable device called Coaguchek [147], partial thromboplastin time (PTT) [148] and thromboelastography (TEG) [149]. Prothrombin time test is a relatively low cost and widely used, but it provides a single data point for the whole coagulation process without any information about the dynamics. On the other hand, thromboelastography is a "gold standard" method that monitors the dynamics of coagulation by continuously measuring the strength of the clot, but it is much more expensive and slow. Recent advances have led to new devices for coagulation analysis. These devices are based on optical [150-153], electrical [154,155] and mechanical properties of blood [156].

Lim et al. [150] used transmission of light through blood plasma to detect the rate of coagulation but their device required pre-processing of blood before testing. Other optical devices based on surface plasmon resonance [151,152] were used with the whole blood, but their continuous operation required sophisticated sensor pre-processing before each testing. Light scattering technique was also used for coagulation detection [153], but different effects related to presence of the cells caused decrease in sensitivity and reproducibility [157]. Magnetic detection of blood coagulation requires use of external receiver coil that cannot be integrated on-chip [156]. Change in electrical properties of blood has also been demonstrated as a mechanism for monitoring blood coagulation [154,155]. Lei et al [155] fabricated an microfluidic sensor that required such external components as pumps and electrodes. Usually one of those limitations prevented integration of blood coagulation device on-chip. More recently, Tripathi et al. [158] utilized the change in light speckle intensity caused by cells in the whole blood. Since movement of cells becomes slower as coagulation increases this changes the rate of change of speckle intensity. However they require the use of high speed cameras making the process expensive.

Several refractive index sensors have been developed till date. These include brag grating sensors [159], photonic crystals [160], ring resonators [161], long period fiber grating [162] and others [163-169]. These sensors are extremely sensitive to their surrounding medium and their performance will be influenced by the presence of red blood cells.

There is a need to create a new low-cost, on chip, easy to operate device that would be able to monitor coagulation of whole blood continuously near the patient. The device proposed in this dissertation is based on continuous monitoring of the refractive index change of whole blood during coagulation [170].

The main sensing component is silicon waveguides with a silicon dioxide ($SiO_{2)}$ cladding that can be easily integrated on-chip. The device can measure the amount of light reflected back from the waveguide-whole blood interface using Fresnel's equation for reflectance. The coagulation can be monitored by observing the change in reflected power during increase of refractive index of coagulating blood. This task is usually very challenging since blood is very nonhomogeneous [171] and red blood cells absorb and scatter light [157,172]. In this work, first the amount of noise created by the presence of red blood cells was characterized and then propose a technique to eliminate the noise generated by the presence of red blood cells by isolating them from the sensor surface using a 3D cladding filtering structure. The proposed device can be easily fabricated with the current MEMS technologies. First, layers of silicon dioxide cladding and silicon core can be deposited using one of several deposition techniques available [173]. Following this, well characterized fabrication techniques such as lithography and dry etching [174] can be utilized for fabricating low loss devices within simulated design parameters. The new proposed structure would enable the device to work with the whole blood and at the same time be miniature, low cost, and provide continuous information about the dynamics of coagulation.

**6.2 Design**

The blood coagulation device based on optical waveguides can be made really miniature (Figure 40). During coagulation blood plasma refractive index increases while fibrin mesh is formed around blood cells. This change in refractive index can be detected by measuring amount of light reflected from the interface between the waveguide and the plasma. When refractive index of the waveguide material is known, Fresnel's equation can be used to calculate the refractive index of plasma. The Y-splitter is used to connect the light source and the detector to

the sensing waveguide. Light is coupled into the waveguide and is reflected back from the waveguide-blood interface to a light detector/ power meter as shown in the Figure 40. The refractive index of blood determines how much light is reflected back into the detector. By monitoring the rate of change of power reflected back to the detector speed of coagulation can be determined. The cells present in the system can also reflect some light back to the waveguide and thus introduce additional noise interfering with the measurements.

Initially different materials were considered for the waveguide. The first step for design optimization was to determine material that would provide highest signal. Figure 41 (a) demonstrates reflectivity from the waveguide-blood interface calculated using Fresnel's equation, eq. (8), $R = \left(\frac{n_1 - n_2}{n_1 + n_2}\right)^2$, where $n_1$ is the refractive index of the waveguide material and $n_2$ is the refractive index of the blood. The uncoagulated and coagulated blood refractive indices used in the simulations are 1.345 and 1.351 respectively [175]. Figure 41 (b) shows the difference in signals for uncoagulated vs. fully-coagulated plasma. Both plots are normalized relative to the input intensity equal to 1 a.u. It can be noticed that a higher refractive index corresponds to a higher portion of light reflected from the interface and also to a higher contrast between coagulated and uncoagulated plasma. Therefore, for the maximum signal level, silicon with a refractive index of 3.5 is chosen for the core of the waveguide. Infrared light with the wavelength 1.5 μm was used in simulations since it can propagate in silicon waveguide with very low attenuation.

### 6.3 Results and Discussion

Three dimensional (3D) simulations were performed using commercial FDTD software. The waveguide core had square cross section with 1μm x 1μm and refractive index 3.5

corresponding to silicon. The substrate and cladding were both silicon dioxide with refractive index of 1.46.

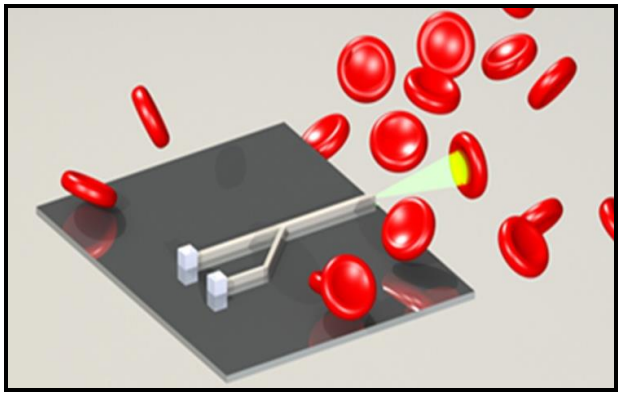

Figure 40 The proposed design for the blood coagulation sensor. Light is coupled into the waveguide and is reflected back from the waveguide-blood interface into the power detector. The change in refractive is monitored by measuring the change in reflected power.

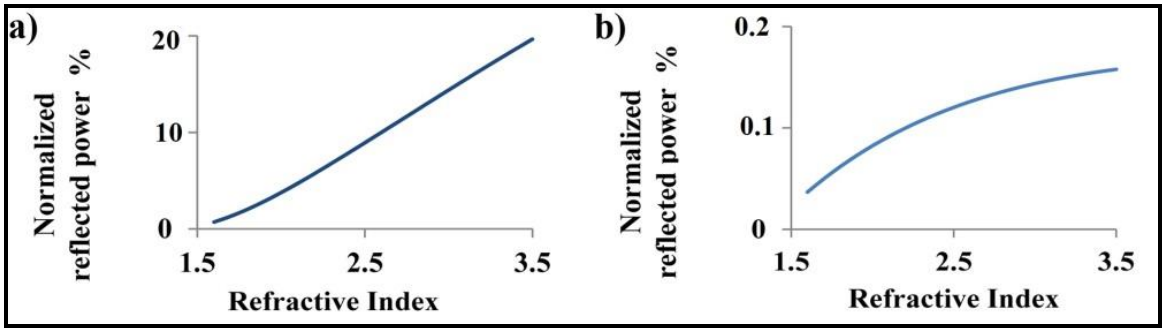


Figure 41 Waveguide material selection. (a) Demonstrates reflectivity from the waveguide-blood interface calculated using Fresnel's equation (8), where n1 is the refractive index of the waveguide material and n2 is the refractive index of the blood. The uncoagulated and coagulated blood refractive indices used in the simulations are 1.345 and 1.351 respectively. (b) shows the difference in signals for uncoagulated vs. fully-coagulated plasma for different sensing materials. Both plots are normalized relative to the input intensity equal to 1 .a.u.

The red blood cells were modeled with refractive index 1.394 [176] and diameter 6 μm [177]. IR light was coupled into the waveguide and is reflected back from the waveguide blood interface. Initially reflected power was measured for uncoagulated and coagulated blood plasma and normalized with respect to the value for uncoagulated plasma. These two values are used as

boundary conditions for the rest of the simulations in this study. All the normalized powers presented in this study are normalized with respect to the reflected power from the uncoagulated blood plasma.

The simulations were conducted in several steps. They started with characterization of the noise caused by the presence of red blood cells in the whole blood. First, orientation of the cell reflecting most of the light back into waveguide was determined. Figure 42 (a) shows normalized reflected power vs angle between the cell and the waveguide interface. Figure 42 (b) explains the way how angle was determined. The noise was the highest when the cell was oriented directly facing the waveguide at zero degrees. Considering this orientation of the cell the "worst case scenario" generating maximum noise, the next set simulations was conducted for this orientation.

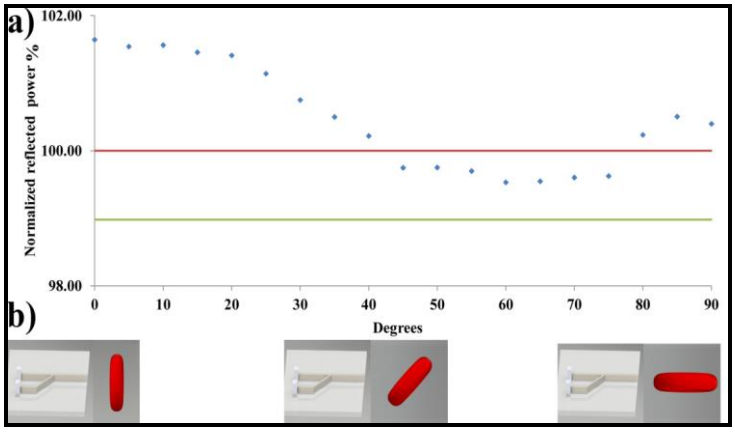


Figure 42 Noise due to presence of cell at different orientations. (a) The normalized reflected power (in %) vs. angle between the cell and the interface of the waveguide. Red line is the reflected power from the uncoagulated blood. Green line is the reflected power from the coagulated blood. Blue is the reflected power in presence of the red blood cell. (b) Explanation of the orientation of the cell relative to the waveguide (not to scale).

After that the noise from the presence of the cell in front of the waveguide interface was analyzed for different distances between the cell and the waveguide. As the cell was moved away

from the waveguide the total intensity, including intensity from the waveguide interface and the back-reflection from the cell, was measured at the other end of the waveguide.

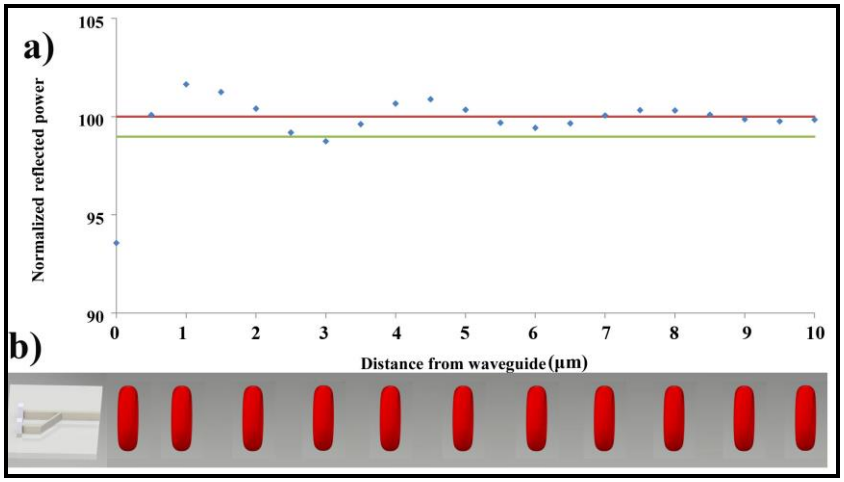


Figure 43 Noise due to presence of cell at different distances from waveguide. a) The normalized reflected power vs. distance of the cell from the interface face of the waveguide. Red line is the reflected power from the uncoagulated blood, green line is the reflected power from the coagulated blood, blue dots is the reflected power in presence of the red blood cell. b) Visualization of the cell movement from the interface of the waveguide (picture not to scale).

Figure 43 demonstrates the data for the cell that was moved away from the face of the waveguide to a distance of 10 µm with 0.5 µm per increment. The normalized reflected power is the ratio of the reflected power in presence of the cell to the power reflected from the pure uncoagulated blood plasma. It can be noticed that when the cell is close to the waveguide there is a high level of noise, and a small movement causes large signal fluctuation. The amplitude of the fluctuation is higher than the difference in signals between uncoagulated and fully coagulated plasma, what makes signal to noise ratio less than one and any detection impossible. Furthermore, the level of noise significantly decreases when the cell moves away from the interface of the waveguide. Since red blood cells can sediment at speed of several micrometers per second [178], this means that for right orientation it would take only a few seconds before the cells move out of the high noise range and not influence the detection of coagulation at all.

However this design would not be immune to noise caused by movement of the sensor as the whole what can produce random movement of cells near waveguide interface. Therefore, there is a need to completely eliminate the presence of cells from the interface of the waveguide.

In order to completely eliminate all the noise caused by the presence of the cells a new 3D cladding is proposed for the waveguide that will be filtering all the blood cells (Figure 44) The cladding is 10 μm thick and contains 1μm slit above the core of the waveguide. Red and white blood cells will be filtered out and stay on the surface of the cladding, since they are larger than the size of the opening, and only plasma will be able to reach the reflective waveguide interface.

Simulations were conducted for same conditions as earlier simulations. The cell is moved from the face of the waveguide to observe the influence of new design on the noise by cells.

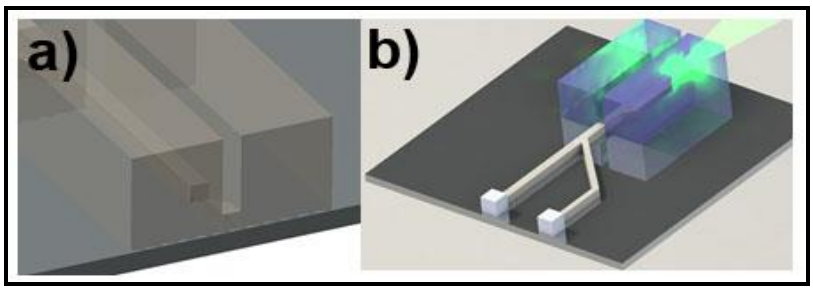


Figure 44 Proposed 3D cladding design. The next iteration of the design with 3D tall cladding for filtering cells from the sensing interface of the waveguide.

Figure 45 (a) shows the refractive index profile in cross section of the proposed 3D cell filtering cladding with 1 μm wide slit giving access to plasma and filtering out cells. Figure 45 (b) demonstrates the mode inside the waveguide.

The tail of the mode does not propagate far from the core, therefore cells on the surface of the cladding will be virtually invisible to the sensor. In order to confirm this statement additional simulations were conducted for this device configuration.

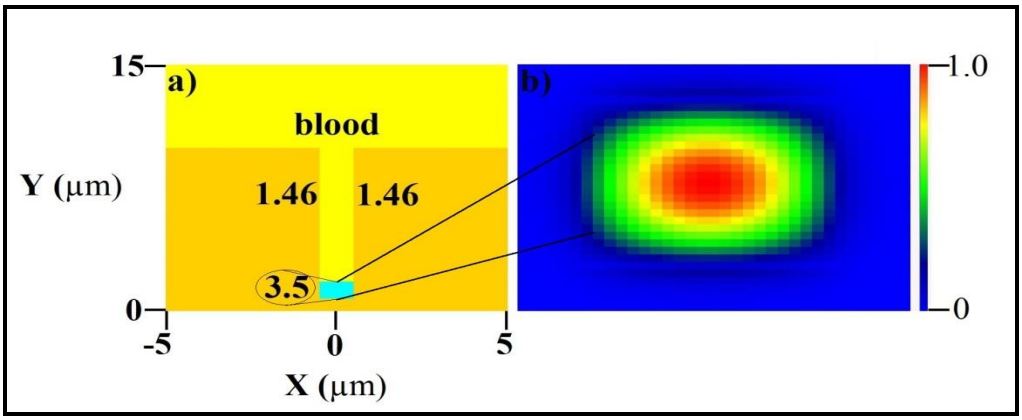


Figure 45 Refractive index and mode of proposed design. (a) The refractive index plot of the blood coagulation sensor. Si, n =3.5, represented by cyan color, cladding SiO2, n=1.46, represented by orange color and surrounded by blood, n = 1.345, represented by yellow color. (b) The mode supported by the Si waveguide.

Figure 46 shows the normalized power vs the distance between the cell and the waveguide for the configurations without and with the cladding. It can be noticed that with the cladding all the noise due to the presence of the cell is completely eliminated. Since the cells are completely removed from the interface of the waveguide, the reflected power is coming only from the blood plasma completely ignoring cells.

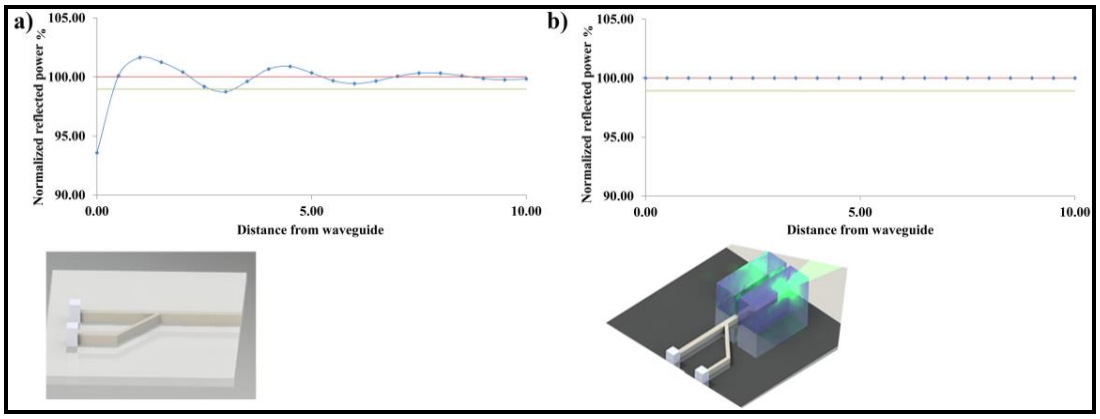


Figure 46 Reduction of noise due to 3D cladding design. The normalized reflected power vs. distance of the cell from the interface of the waveguide. Red is the reflected power from the uncoagulated blood. Green is the reflected power from the coagulated blood. Blue is the reflected power in presence of the red blood cell for designs without (a) and with the 3D cladding (b).

## 6.4 Conclusion

Design and optimization of a new on-chip photonic sensor for continuous coagulation monitoring in whole blood was presented. Three dimensional FDTD simulations were used for the design optimization. It was observed that reflection from a waveguide interface can be used to monitor increasing reflective index of coagulating blood, but that cells would generate noise with the amplitude larger than the signal to measure. Consecutively, new design has been proposed. It included incorporation of tall waveguide claddings containing small slits that can filter out the cells, but give access to the plasma. It was then demonstrated that the structure can be used to completely eliminate noise caused by the cells while accurately measuring the increase of refractive index in blood plasma.

## REFERENCES


1. "Nanophotonics: Accessibility and Applicability". 2008: The National Academies Press.

2. Kirchain, R. and L. Kimerling, "A roadmap for nanophotonics". *Nature Photonics*, 2007. **1**(6): p. 303-305.

3. Pavesi, L. and D.J. Lockwood, "Silicon photonics". Vol. 1. 2004: Springer.

4. Loncar, M. and A. Faraon, "Quantum photonic networks in diamond". *Mrs Bulletin*, 2013. **38**(2): p. 144-148.

5. Avouris, P. and F.N. Xia, "Graphene applications in electronics and photonics". *Mrs Bulletin*, 2012. **37**(12): p. 1225-1234.

6. Chu, S., G. Wang, W. Zhou, Y. Lin, L. Chernyak, J. Zhao, J. Kong, L. Li, J. Ren, and J. Liu, "Electrically pumped waveguide lasing from ZnO nanowires". *Nature Nanotechnology*, 2011. **6**(8): p. 506-510.

7. Xiong, X., C.L. Zou, X.F. Ren, A.P. Liu, Y.X. Ye, F.W. Sun, and G.C. Guo, "Silver nanowires for photonics applications". *Laser & Photonics Reviews*, 2013.

8. Xiong, Q., C.A. Grimes, M. Zacharias, A.F.i. Morral, K. Hiruma, and G. Shen, "Semiconductor Nanowires and Nanotubes: From Fundamentals to Diverse Applications". *Journal of Nanotechnology*, 2012. **2012**.

9. Murphy, C.J., T.K. San, A.M. Gole, C.J. Orendorff, J.X. Gao, L. Gou, S.E. Hunyadi, and T. Li, "Anisotropic metal nanoparticles: Synthesis, assembly, and optical applications". *Journal of Physical Chemistry B*, 2005. **109**(29): p. 13857-13870.

10. Cunningham, A. and T. Bürgi, "Bottom-up Organisation of Metallic Nanoparticles", in *Amorphous Nanophotonics*, C. Rockstuhl and T. Scharf, Editors. 2013, Springer Berlin Heidelberg. p. 1-37.

11. Van Thourhout, D., T. Spuesens, S.K. Selvaraja, L. Liu, G. Roelkens, R. Kumar, G. Morthier, P. Rojo-Romeo, F. Mandorlo, P. Regreny, O. Raz, C. Kopp, and L. Grenouillet, "Nanophotonic Devices for Optical Interconnect". *Ieee Journal of Selected Topics in Quantum Electronics*, 2010. **16**(5): p. 1363-1375.

12. Peumans, P., A. Yakimov, and S.R. Forrest, "Small molecular weight organic thin-film photodetectors and solar cells". *Journal of Applied Physics*, 2003. **93**(7): p. 3693-3723.

13. Jackson, J.B. and N.J. Halas, "Surface-enhanced Raman scattering on tunable plasmonic nanoparticle substrates". *Proceedings of the National Academy of Sciences of the United States of America*, 2004. **101**(52): p. 17930-17935.

14. Maisenholder, B., H.P. Zappe, M. Moser, P. Riel, R.E. Kunz, and J. Edlinger, "Monolithically integrated optical interferometer for refractometry". *Electronics Letters*, 1997. **33**(11): p. 986-988.

15. Stockle, R.M., Y.D. Suh, V. Deckert, and R. Zenobi, "Nanoscale chemical analysis by tip-enhanced Raman spectroscopy". *Chemical Physics Letters*, 2000. **318**(1-3): p. 131-136.

16. Polman, A. and H.A. Atwater, "Photonic design principles for ultrahigh-efficiency photovoltaics". *Nature Materials*, 2012. **11**(3): p. 174-177.

17. Prasad, P.N., "Nanophotonics". 2004: Wiley. com.

18. Nel, A.E., L. Mädler, D. Velegol, T. Xia, E.M. Hoek, P. Somasundaran, F. Klaessig, V. Castranova, and M. Thompson, "Understanding biophysicochemical interactions at the nano–bio interface". *Nature materials*, 2009. **8**(7): p. 543-557.

19. Atwater, H.A., "The promise of plasmonics". *Scientific American*, 2007. **296**(4): p. 56-63.

20. Haes, A.J. and R.P. Van Duyne, "A nanoscale optical biosensor: sensitivity and selectivity of an approach based on the localized surface plasmon resonance spectroscopy of triangular silver nanoparticles". *Journal of the American Chemical Society*, 2002. **124**(35): p. 10596-10604.

21. Chow, E., A. Grot, L. Mirkarimi, M. Sigalas, and G. Girolami, "Ultracompact biochemical sensor built with two-dimensional photonic crystal microcavity". *Optics letters*, 2004. **29**(10): p. 1093-1095.

22. Bergey, E., L. Levy, X. Wang, L. Krebs, M. Lal, K.-S. Kim, S. Pakatchi, C. Liebow, and P. Prasad, "DC Magnetic Field Induced Magnetocytolysis of Cancer Cells Targeted by LH-RH Magnetic Nanoparticles in vitro". *Biomedical Microdevices*, 2002. **4**(4): p. 293-299.

23. Kaern, M., T.C. Elston, W.J. Blake, and J.J. Collins, "Stochasticity in gene expression: From theories to phenotypes". *Nature Reviews Genetics*, 2005. **6**(6): p. 451-464.

24. Wang, D.J. and S. Bodovitz, "Single cell analysis: the new frontier in 'omics'". *Trends in Biotechnology*, 2010. **28**(6): p. 281-290.

25. Teruel, M.N. and T. Meyer, "Parallel single-cell monitoring of receptor-triggered membrane translocation of a calcium-sensing protein module". *Science*, 2002. **295**(5561): p. 1910-1912.

26. Walling, M.A. and J.R.E. Shepard, "Cellular heterogeneity and live cell arrays". *Chemical Society Reviews*, 2011. **40**(7): p. 4049-4076.

27. Orynbayeva, Z., R. Singhal, E.A. Vitol, M.G. Schrlau, E. Papazoglou, G. Friedman, and Y. Gogotsi, "Physiological validation of cell health upon probing with carbon nanotube endoscope and its benefit for single-cell interrogation". *Nanomedicine-Nanotechnology Biology and Medicine*, 2012. **8**(5): p. 590-598.

28. Zheng, X.T., H.B. Yang, and C.M. Li, "Optical Detection of Single Cell Lactate Release for Cancer Metabolic Analysis". *Analytical Chemistry*, 2010. **82**(12): p. 5082-5087.

29. Gao, Y., T. Longenbach, E.A. Vitol, Z. Orynbayeva, G. Friedman, and Y. Gogotsi, "One-dimensional nanoprobes for single-cell studies". *Nanomedicine*, 2014. **9**(1): p. 153-168.

30. Evanko, D., "Watching single molecules in cells". *Nature Methods*, 2008. **5**(1): p. 25-25.

31. Wang, S., F. Ye, X. Lang, D. Fei, A. Turner, and Y. Ge, "Detection of [Ca2+] I Changes In Sub-Plasma Membrane Micro Domains in A Single Living Cell By an Optical Fiber-Based Nanobiosensor". *Austin Journal of Nanomedicine and Nanotechnology*, 2014. **2**(4): p. 1022.

32. Zheng, X.T. and C.M. Li, "Single cell analysis at the nanoscale". *Chemical Society Reviews*, 2012. **41**(6): p. 2061-2071.

33. Lindstrom, S. and H. Andersson-Svahn, "Overview of single-cell analyses: microdevices and applications". *Lab on a Chip*, 2010. **10**(24): p. 3363-3372.

34. Yum, K., N. Wang, and M.F. Yu, "Nanoneedle: A multifunctional tool for biological studies in living cells". *Nanoscale*, 2010. **2**(3): p. 363-372.

35. Xie, X.S., J. Yu, and W.Y. Yang, "Perspective - Living cells as test tubes". *Science*, 2006. **312**(5771): p. 228-230.

36. Chao, T.C. and A. Ros, "Microfluidic single-cell analysis of intracellular compounds". *Journal of the Royal Society Interface*, 2008. **5**: p. S139-S150.

37. Minsky, M., "Memoir on Inventing the Confocal Scanning Microscope". *Scanning*, 1988. **10**(4): p. 128-138.

38. Denk, W., J.H. Strickler, and W.W. Webb, "Two-photon laser scanning fluorescence microscopy". *Science*, 1990. **248**(4951): p. 73-76.

39. Kalies, S., K. Kuetemeyer, and A. Heisterkamp, "Mechanisms of high-order photobleaching and its relationship to intracellular ablation". *Biomedical Optics Express*, 2011. **2**(4): p. 805-816.

40. Hell, S.W. and J. Wichmann, "Breaking the diffraction resolution limit by stimulated emission: stimulated-emission-depletion fluorescence microscopy". *Optics Letters*, 1994. **19**(11): p. 780-782.

41. Rust, M.J., M. Bates, and X.W. Zhuang, "Sub-diffraction-limit imaging by stochastic optical reconstruction microscopy (STORM)". *Nature Methods*, 2006. **3**(10): p. 793-795.

42. Chiu, D.T., "Micro- and nano-scale chemical analysis of individual sub-cellular compartments". *Trac-Trends in Analytical Chemistry*, 2003. **22**(9): p. 528-536.

43. Tan, W.H., Z.Y. Shi, S. Smith, D. Birnbaum, and R. Kopelman, "Submicrometer Intracellular Chemical Optical Fiber Sensors". *Science*, 1992. **258**(5083): p. 778-781.

44. Ball, G., R.M. Parton, R.S. Hamilton, and I. Davis, "A Cell Biologist's Guide to High Resolution Imaging". *Imaging and Spectroscopic Analysis of Living Cells: Optical and Spectroscopic Techniques*, 2012. **504**: p. 29-55.

45. Givan, A.L., "Principles of flow cytometry: An overview". *Methods in Cell Biology, Vol 63*, 2001. **63**: p. 19-50.

46. Villas, B., "Flow cytometry: an overview". *Cell vision: the journal of analytical morphology*, 1997. **5**(1): p. 56-61.

47. Obataya, I., C. Nakamura, S. Han, N. Nakamura, and J. Miyake, "Nanoscale operation of a living cell using an atomic force microscope with a nanoneedle". *Nano Letters*, 2005. **5**(1): p. 27-30.

48. Vo-Dinh, T., "Nanobiosensors: Probing the sanctuary of individual living cells". *Journal of Cellular Biochemistry*, 2002: p. 154-161.

49. Chen, X., A. Kis, A. Zettl, and C.R. Bertozzi, "A cell nanoinjector based on carbon nanotubes". *Proceedings of the National Academy of Sciences*, 2007. **104**(20): p. 8218-8222.

50. Menard-Moyon, C., K. Kostarelos, M. Prato, and A. Bianco, "Functionalized Carbon Nanotubes for Probing and Modulating Molecular Functions". *Chemistry & Biology*, 2010. **17**(2): p. 107-115.

51. Singhal, R., Z. Orynbayeva, R.V.K. Sundaram, J.J. Niu, S. Bhattacharyya, E.A. Vitol, M.G. Schrlau, E.S. Papazoglou, G. Friedman, and Y. Gogotsi, "Multifunctional carbon-nanotube cellular endoscopes". *Nature Nanotechnology*, 2011. **6**(1): p. 57-64.

52. Niu, J.J., M.G. Schrlau, G. Friedman, and Y. Gogotsi, "Carbon Nanotube-Tipped Endoscope for In Situ Intracellular Surface-Enhanced Raman Spectroscopy". *Small*, 2011. **7**(4): p. 540-545.

53. Yum, K.S., H.N. Cho, H. Hu, and M.F. Yu, "Individual nanotube-based needle nanoprobes for electrochemical studies in picoliter microenvironments". *Acs Nano*, 2007. **1**(5): p. 440-448.

54. Yum, K., S. Na, Y. Xiang, N. Wang, and M.F. Yu, "Mechanochemical Delivery and Dynamic Tracking of Fluorescent Quantum Dots in the Cytoplasm and Nucleus of Living Cells". *Nano Letters*, 2009. **9**(5): p. 2193-2198.

55. Lu, G., H. De Keersmaecker, L. Su, B. Kenens, S. Rocha, E. Fron, C. Chen, P. Van Dorpe, H. Mizuno, J. Hofkens, J.A. Hutchison, and H. Uji-i, "Live-Cell SERS Endoscopy Using Plasmonic Nanowire Waveguides". *Advanced Materials*, 2014. **26**(30): p. 5124-5128.

56. Han, S.W., C. Nakamura, I. Obataya, N. Nakamura, and J. Miyake, "A molecular delivery system by using AFM and nanoneedle". *Biosensors & Bioelectronics*, 2005. **20**(10): p. 2120-2125.

57. Yan, R.X., J.H. Park, Y. Choi, C.J. Heo, S.M. Yang, L.P. Lee, and P.D. Yang, "Nanowire-based single-cell endoscopy". *Nature Nanotechnology*, 2012. **7**(3): p. 191-196.

58. Ladanov, M., S. Cheemalapati, and A. Pyayt, "Optimization of light delivery by a nanowire-based single cell optical endoscope". *Optics Express*, 2013. **21**(23): p. 28001-28009.

59. Shambat, G., S.-R. Kothapalli, J. Provine, T. Sarmiento, J. Harris, S.S. Gambhir, and J. Vučković, "Single-Cell Photonic Nanocavity Probes". *Nano Letters*, 2013.

60. Kasili, P.M., J.M. Song, and T. Vo-Dinh, "Optical sensor for the detection of caspase-9 activity in a single cell". *Journal of the American Chemical Society*, 2004. **126**(9): p. 2799-2806.

61. Wang, S., H. Zhao, Y. Wang, C. Li, Z. Chen, and V. Paulose, "Silver-coated near field optical scanning microscope probes fabricated by silver mirror reaction". *Applied Physics B*, 2008. **92**(1): p. 49-52.

62. Vo-Dinh, T., J.P. Alarie, B.M. Cullum, and G.D. Griffin, "Antibody-based nanoprobe for measurement of a fluorescent analyte in a single cell". *Nature Biotechnology*, 2000. **18**(7): p. 764-767.

63. Zheng, X.T. and C.M. Li, "Single living cell detection of telomerase over-expression for cancer detection by an optical fiber nanobiosensor". *Biosensors & Bioelectronics*, 2010. **25**(6): p. 1548-1552.

64. Kasili, R.M., B.M. Cullum, G.D. Griffin, and T. Vo-Dinh, "Nanosensor for in vivo measurement of the carcinogen benzo[a]pyrene in a single cell". *Journal of Nanoscience and Nanotechnology*, 2002. **2**(6): p. 653-658.

65. Clark, H.A., R. Kopelman, R. Tjalkens, and M.A. Philbert, "Optical nanosensors for chemical analysis inside single living cells. 2. Sensors for pH and calcium and the intracellular application of PEBBLE sensors". *Analytical Chemistry*, 1999. **71**(21): p. 4837-4843.

66. Hong, W., F. Liang, D. Schaak, M. Loncar, and Q.M. Quan, "Nanoscale Label-free Bioprobes to Detect Intracellular Proteins in Single Living Cells". *Scientific Reports*, 2014. **4**.

67. Vitol, E.A., Z. Orynbayeva, M.J. Bouchard, J. Azizkhan-Clifford, G. Friedman, and Y. Gogotsi, "In Situ Intracellular Spectroscopy with Surface Enhanced Raman Spectroscopy (SERS)-Enabled Nanopipettes". *ACS Nano*, 2009. **3**(11): p. 3529-3536.

68. van Zanten, T.S., A. Cambi, and M.F. Garcia-Parajo, "A nanometer scale optical view on the compartmentalization of cell membranes". *Biochimica Et Biophysica Acta-Biomembranes*, 2010. **1798**(4): p. 777-787.

69. Song, J.M., P.M. Kasili, G.D. Griffin, and T. Vo-Dinh, "Detection of cytochrome C in a single cell using an optical nanobiosensor". *Analytical chemistry*, 2004. **76**(9): p. 2591-2594.

70. Barker, S.L., Y. Zhao, M.A. Marletta, and R. Kopelman, "Cellular applications of a sensitive and selective fiber-optic nitric oxide biosensor based on a dye-labeled heme domain of soluble guanylate cyclase". *Analytical chemistry*, 1999. **71**(11): p. 2071-2075.

71. Clarke, S.J., C.A. Hollmann, Z.J. Zhang, D. Suffern, S.E. Bradforth, N.M. Dimitrijevic, W.G. Minarik, and J.L. Nadeau, "Photophysics of dopamine-modified quantumdots and effects on biological systems". *Nature Materials*, 2006. **5**(5): p. 409-417.

72. Lee, J., S. Choi, S.J. Bae, S.M. Yoon, J.S. Choi, and M. Yoon, "Visible light-sensitive APTES-bound ZnO nanowire toward a potent nanoinjector sensing biomolecules in a living cell". *Nanoscale*, 2013. **5**(21): p. 10275-10282.

73. Campagnola, P.J. and L.M. Loew, "Second-harmonic imaging microscopy for visualizing biomolecular arrays in cells, tissues and organisms". *Nature Biotechnology*, 2003. **21**(11): p. 1356-1360.

74. Campagnola, P.J., A.C. Millard, M. Terasaki, P.E. Hoppe, C.J. Malone, and W.A. Mohler, "Three-Dimensional High-Resolution Second-Harmonic Generation Imaging of Endogenous Structural Proteins in Biological Tissues". *Biophysical Journal*, 2002. **82**(1): p. 493-508.

75. LaComb, R., O. Nadiarnykh, and P.J. Campagnola, "Quantitative Second Harmonic Generation Imaging of the Diseased State Osteogenesis Imperfecta: Experiment and Simulation". *Biophysical Journal*, 2008. **94**(11): p. 4504-4514.

76. Makarov, N.S., E. Beuerman, M. Drobizhev, J. Starkey, and A. Rebane. "Environment-sensitive two-photon dye". 2008.

77. Starkey, J.R., N.S. Makarov, M. Drobizhev, and A. Rebane, "Highly sensitive detection of cancer cells using femtosecond dual-wavelength near-IR two-photon imaging". *Biomedical Optics Express*, 2012. **3**(7).

78. Petrušis, A., J.H. Rector, K. Smith, S.d. Man, and D. Iannuzzi, "The align-and-shine technique for series production of photolithography patterns on optical fibres". *Journal of Micromechanics and Microengineering*, 2009. **19**(4).

79. Chang, P.-C., Z. Fan, D. Wang, W.-Y. Tseng, W.-A. Chiou, J. Hong, and J.G. Lu, "ZnO Nanowires Synthesized by Vapor Trapping CVD Method". *Chemistry of Materials*, 2004. **16**(24): p. 5133-5137.

80. Huang, M.H., Y. Wu, H. Feick, N. Tran, E. Weber, and P. Yang, "Catalytic Growth of Zinc Oxide Nanowires by Vapor Transport". *Advanced Materials (Weinheim, Germany)*, 2001. **13**(2): p. 113-116.

81. Kirkham, M., X. Wang, Z.L. Wang, and R.L. Snyder, "Solid Au nanoparticles as a catalyst for growing aligned ZnO nanowires: a new understanding of the vapour–liquid–solid process". *Nanotechnology*, 2007. **18**(36).

82. Greene, L.E., M. Law, J. Goldberger, F. Kim, J.C. Johnson, Y. Zhang, R.J. Saykally, and P. Yang, "Low-Temperature Wafer-Scale Production of ZnO Nanowire Arrays". *Angewandte Chemie International Edition*, 2003. **42**(26): p. 3031-3034.

83. Greene, L.E., M. Law, D.H. Tan, M. Montano, J. Goldberger, G. Somorjai, and P. Yang, "General Route to Vertical ZnO Nanowire Arrays Using Textured ZnO Seeds". *Nano Letters*, 2005. **5**(7): p. 1231-1236.

84. Vayssieres, L., "Growth of Arrayed Nanorods and Nanowires of ZnO from Aqueous Solutions". *Advanced Materials (Weinheim, Germany)*, 2003. **15**(5): p. 464-466.

85. Ebbesen, T.W., H.J. Lezec, H.F. Ghaemi, T. Thio, and P.A. Wolff, "Extraordinary optical transmission through sub-wavelength hole arrays". *Nature*, 1998. **391**(6668): p. 667-669.

86. Miyamaru, F. and M. Hangyo, "Anomalous terahertz transmission through double-layer metal hole arrays by coupling of surface plasmon polaritons". *Physical Review B*, 2005. **71**(16).

87. Velasco, M.G., P. Cassidy, and H. Xu, "Extraordinary transmission of evanescent modes through a dielectric-filled nanowaveguide". *Optics Communications*, 2011. **284**(19): p. 4805-4809.

88. Weintraub, B., Y.G. Wei, and Z.L. Wang, "Optical Fiber/Nanowire Hybrid Structures for Efficient Three-Dimensional Dye-Sensitized Solar Cells". *Angewandte Chemie-International Edition*, 2009. **48**(47): p. 8981-8985.

89. Mitsushio, M., K. Miyashita, and M. Higo, "Sensor properties and surface characterization of the metal-deposited SPR optical fiber sensors with Au, Ag, Cu, and Al". *Sensors and Actuators a-Physical*, 2006. **125**(2): p. 296-303.

90. Shambat, G., J. Provine, K. Rivoire, T. Sarmiento, J. Harris, and J. Vuckovic, "Optical fiber tips functionalized with semiconductor photonic crystal cavities". *Applied Physics Letters*, 2011. **99**(19): p. 191102-191102-3.

91. Liao, W.S., S. Cheunkar, H.H. Cao, H.R. Bednar, P.S. Weiss, and A.M. Andrews, "Subtractive Patterning via Chemical Lift-Off Lithography". *Science*, 2012. **337**(6101): p. 1517-1521.

92. Mendes, P.M., S. Jacke, K. Critchley, J. Plaza, Y. Chen, K. Nikitin, R.E. Palmer, J.A. Preece, S.D. Evans, and D. Fitzmaurice, "Gold nanoparticle patterning of silicon wafers using chemical e-beam lithography". *Langmuir*, 2004. **20**(9): p. 3766-3768.

93. Bourliaguet, B., C. Pare, F. Emond, A. Croteau, A. Proulx, and R. Vallee, "Microstructured fiber splicing". *Optics Express*, 2003. **11**(25): p. 3412-3417.

94. Grier, D.G., "A revolution in optical manipulation". *Nature*, 2003. **424**(6950): p. 810-816.

95. Puygranier, B.A.F. and P. Dawson, "Chemical etching of optical fibre tips - experiment and model". *Ultramicroscopy*, 2000. **85**(4): p. 235-248.

96. Cao, J. and J.Z. Wang, "Development of Ag nanopolyhedra based fiber-optic probes for high performance SERS detection". *New Journal of Chemistry*, 2015. **39**(4): p. 2421-2424.

97. Vo-Dinh, T. and P. Kasili, "Fiber-optic nanosensors for single-cell monitoring". *Analytical and Bioanalytical Chemistry*, 2005. **382**(4): p. 918-925.

98. Mondal, S.K., A. Mitra, N. Singh, S.N. Sarkar, and P. Kapur, "Optical fiber nanoprobe preparation for near-field optical microscopy by chemical etching under surface tension and capillary action". *Optics Express*, 2009. **17**(22): p. 19470-19475.

99. Morley, J.F., H.R. Brignull, J.J. Weyers, and R.I. Morimoto, "The threshold for polyglutamine-expansion protein aggregation and cellular toxicity is dynamic and influenced by aging in Caenorhabditis elegans". *Proceedings of the National Academy of Sciences*, 2002. **99**(16): p. 10417-10422.

100. Liao, L., D.R. Lim, A.M. Agarwal, X.M. Duan, K.K. Lee, and L.C. Kimerling, "Optical transmission losses in polycrystalline silicon strip waveguides: Effects of waveguide dimensions, thermal treatment, hydrogen passivation, and wavelength". *Journal of Electronic Materials*, 2000. **29**(12): p. 1380-1386.

101. Säynätjoki, A., S. Arpiainen, J. Ahopelto, and H. Lipsanen. "High-index-contrast optical waveguides on silicon". in *Physics of Semiconductors: 27th International Conference on the Physics of Semiconductors–ICPS*. 2005.

102. Yimit, A., A.G. Rossberg, T. Amemiya, and K. Itoh, "Thin film composite optical waveguides for sensor applications: a review". *Talanta*, 2005. **65**(5): p. 1102-1109.

103. Jaberansary, E., T.M.B. Masaud, M.M. Milosevic, M. Nedeljkovic, G.Z. Mashanovich, and H.M.H. Chong, "Scattering Loss Estimation Using 2-D Fourier Analysis and Modeling of Sidewall Roughness on Optical Waveguides". *Ieee Photonics Journal*, 2013. **5**(3).

104. Barwicz, T. and H.A. Haus, "Three-dimensional analysis of scattering losses due to sidewall roughness, in microphotonic waveguides". *Journal of Lightwave Technology*, 2005. **23**(9): p. 2719-2732.

105. Kartalopoulos, S.V., "Introduction to DWDM technology: data in a rainbow". 2000.

106. Lee, K.K., D.R. Lim, L.C. Kimerling, J. Shin, and F. Cerrina, "Fabrication of ultralow-loss Si/SiO2 waveguides by roughness reduction". *Optics Letters*, 2001. **26**(23): p. 1888-1890.

107. Ladouceur, F., J.D. Love, and T.J. Senden, "Effect of side wall roughness in buried channel waveguides". *Optoelectronics, IEE Proceedings* -, 1994. **141**(4): p. 242-248.

108. Zhou, Z., "Micro/Nano Lithography Accurate top-down processing of silicon photonic devices".

109. Sparacin, D.K., K. Wada, and L.C. Kimerling. "Oxidation kinetics of waveguide roughness minimization in silicon microphotonics". in *Integrated Photonics Research*. 2003. Washington, D.C.: Optical Society of America.

110. Sparacin, D.K., S.J. Spector, and L.C. Kimerling, "Silicon waveguide sidewall smoothing by wet chemical oxidation". *Journal of Lightwave Technology*, 2005. **23**(8): p. 2455-2461.

111. Cai, J.N., P.H. Lim, Y. Ishikawa, and K. Wada, "Silicon Waveguide Sidewall Smoothing by Resist Reflowing". *Journal of Nonlinear Optical Physics & Materials*, 2010. **19**(4): p. 801-809.

112. Jette-Charbonneau, S., N. Lahoud, R. Charbonneau, G. Mattiussi, and P. Berini, "End-facet polishing of surface plasmon waveguides in lithium niobate". *Advanced Packaging, IEEE Transactions on*, 2008. **31**(3): p. 479-483.

113. Hung, S.C., E.Z. Liang, and C.F. Lin, "Silicon Waveguide Sidewall Smoothing by KrF Excimer Laser Reformation". *Journal of Lightwave Technology*, 2009. **27**(5-8): p. 887-892.

114. Solehmainen, K., T. Aalto, J. Dekker, M. Kapulainen, M. Harjanne, K. Kukli, P.i. Heimala, K. Kolari, and M. Leskel, "Dry-Etched Silicon-on-Insulator Waveguides With Low Propagation and Fiber-Coupling Losses". *Journal of Lightwave Technology*, 2005. **23**(11).

115. Li, W., Y. Ruan, B. Luther-Davies, A. Rode, and R. Boswell, "Dry-etch of As[sub 2]S[sub 3] thin films for optical waveguide fabrication". *Journal of Vacuum Science & Technology A: Vacuum, Surfaces, and Films*, 2005. **23**(6): p. 1626-1632.

116. Li, W.T., D.A.P. Bulla, J. Love, B. Luther-Davies, C. Charles, and R. Boswell, "Deep dry-etch of silica in a helicon plasma etcher for optical waveguide fabrication". *Journal of Vacuum Science & Technology A: Vacuum, Surfaces, and Films*, 2005. **23**(1): p. 146-150.

117. Donnelly, V.M. and A. Kornblit, "Plasma etching: Yesterday, today, and tomorrow". *Journal of Vacuum Science & Technology A*, 2013. **31**(5).

118. d'Agostino, R. and D.L. Flamm, "Plasma etching of Si and SiO2 in SF6–O2 mixtures". *Journal of Applied Physics*, 1981. **52**(1): p. 162-167.

119. Schmidtchen, J., A. Splett, B. Schuppert, K. Petermann, and G. Burbach, "Low loss singlemode optical waveguides with large cross-section in silicon-on-insulator". *Electronics Letters*, 1991. **27**(16): p. 1486-1488.

120. Payne, F.P. and J.P.R. Lacey, "A theoretical analysis of scattering loss from planar optical waveguides". *Optical and Quantum Electronics*, 1994. **26**(10): p. 977-986.

121. Tien, P.K., "Light Waves in Thin Films and Integrated Optics". *Applied Optics*, 1971. **10**(11): p. 2395-&.

122. Legtenberg, R., H. Jansen, M. de Boer, and M. Elwenspoek, "Anisotropic reactive ion etching of silicon using SF 6/O 2/CHF 3 gas mixtures". *Journal of The Electrochemical Society*, 1995. **142**(6): p. 2020-2028.

123. Pessoa, R.S., L.L. Tezani, H.S. Maciel, G. Petraconi, and M. Massi, "Study of SF6 and SF6/O-2 plasmas in a hollow cathode reactive ion etching reactor using Langmuir probe and optical emission spectroscopy techniques". *Plasma Sources Science & Technology*, 2010. **19**(2).

124. Kechkar, S., P. Swift, J. Conway, M. Turner, and S. Daniels, "Investigation of atomic oxygen density in a capacitively coupled O-2/SF6 discharge using two-photon absorption laser-induced fluorescence spectroscopy and a Langmuir probe". *Plasma Sources Science & Technology*, 2013. **22**(4).

125. Zhang, Q.Z., Y.X. Liu, W. Jiang, A. Bogaerts, and Y.N. Wang, "Heating mechanism in direct current superposed single-frequency and dual-frequency capacitively coupled plasmas". *Plasma Sources Science & Technology*, 2013. **22**(2).

126. Hamaoka, F., T. Yagisawa, and T. Makabe, "Numerical investigation of relationship between micro-scale pattern, interfacial plasma structure and feature profile during deep-Si etching in two-frequency capacitively coupled plasmas in SF6/O-2". *Journal of Physics D-Applied Physics*, 2009. **42**(7).

127. Watanabe, A., F. Ishikawa, and M. Kondow, "Effects of Plasma Processes on the Characteristics of Optical Device Structures Based on GaAs". *Japanese Journal of Applied Physics*, 2012. **51**(5).

128. Ray, T., H. Zhu, and D.R. Meldrum, "Deep reactive ion etching of fused silica using a single-coated soft mask layer for bio-analytical applications". *Journal of Micromechanics and Microengineering*, 2010. **20**(9): p. 097002.

129. Miyawaki, Y., Y. Kondo, M. Sekine, K. Ishikawa, T. Hayashi, K. Takeda, H. Kondo, A. Yamazaki, A. Ito, H. Matsumoto, and M. Hori, "Highly Selective Etching of SiO2 over Si3N4 and Si in Capacitively Coupled Plasma Employing C5HF7 Gas". *Japanese Journal of Applied Physics*, 2013. **52**(1).

130. Porkolab, G.A., P. Apiratikul, B. Wang, S.H. Guo, and C.J.K. Richardson, "Low propagation loss AlGaAs waveguides fabricated with plasma-assisted photoresist reflow". *Optics Express*, 2014. **22**(7): p. 7733-7743.

131. Ohring, M., "Materials Science of Thin Films". 2001: Academic Press. 818.

132. Ben Masaud, T.M., A. Tarazona, E. Jaberansary, X. Chen, G.T. Reed, G.Z. Mashanovich, and H.M.H. Chong, "Hot-wire polysilicon waveguides with low deposition temperature". *Optics Letters*, 2013. **38**(20): p. 4030-4032.

133. Agarwal, A.M., L. Liao, J.S. Foresi, M.R. Black, X.M. Duan, and L.C. Kimerling, "Low-loss polycrystalline silicon waveguides for silicon photonics". *Journal of Applied Physics*, 1996. **80**(11): p. 6120-6123.

134. Orcutt, J.S., S.D. Tang, S. Kramer, K. Mehta, H.Q. Li, V. Stojanovic, and R.J. Ram, "Low-loss polysilicon waveguides fabricated in an emulated high-volume electronics process". *Optics Express*, 2012. **20**(7): p. 7243-7254.

135. Kwong, D., J. Covey, A. Hosseini, Y. Zhang, X.C. Xu, and R.T. Chen, "Ultralow-loss polycrystalline silicon waveguides and high uniformity 1x12 MMI fanout for 3D photonic integration". *Optics Express*, 2012. **20**(19): p. 21722-21728.

136. Madan, R., B. Gupt, S. Saluja, U. Kansra, B. Tripathi, and B. Guliani, "Coagulation profile in diabetes and its association with diabetic microvascular complications". *J Assoc Physicians India*, 2010. **58**: p. 481-484.

137. Badulescu, O., C. Badescu, I. Alexa, C. Manuela, and M. Badescu, "Coagulation Profile in Patients with Type 2 Diabetes Mellitus and Cardiovascular Disease". *Haematologica-the Hematology Journal*, 2010. **95**: p. 766-766.

138. Key, N., M. Makris, D. O'Shaughnessy, and D. Lillicrap, "Practical hemostasis and thrombosis". 2009: Wiley Online Library.

139. Rodvien, R. and C.H. Mielke, "Role of Platelets in Hemostasis and Thrombosis". *Western Journal of Medicine*, 1976. **125**(3): p. 181-186.

140. Mackman, N., R.E. Tilley, and N.S. Key, "Role of the extrinsic pathway of blood coagulation in hemostasis and thrombosis". *Arteriosclerosis Thrombosis and Vascular Biology*, 2007. **27**(8): p. 1687-1693.

141. Riddel, J.P., B.E. Aouizerat, C. Miaskowski, and D.P. Lillicrap, "Theories of blood coagulation". *Journal of Pediatric Oncology Nursing*, 2007. **24**(3): p. 123-131.

142. Bolton-Maggs, P.H.B., D.J. Perry, E.A. Chalmers, L.A. Parapia, J.T. Wilde, M.D. Williams, P.W. Collins, S. Kitchen, G. Dolan, and A.D. Mumford, "The rare coagulation disorders - review with guidelines for management from the United Kingdom Haemophilia Centre Doctors' Organisation". *Haemophilia*, 2004. **10**(5): p. 593-628.

143. Nelson, K., I. Thethi, J. Cunanan, D. Hoppensteadt, R. Bajwa, J. Fareed, and V. Bansal, "Upregulation of Surrogate Markers of Inflammation and Thrombogenesis in Patients With ESRD: Pathophysiologic and Therapeutic Implications". *Clinical and Applied Thrombosis-Hemostasis*, 2011. **17**(3): p. 302-304.

144. Menendez-Jandula, B., J.C. Souto, A. Oliver, I. Montserrat, M. Quintana, I. Glch, X. Bonfill, and J. Fontcuberta, "Comparing self-management of oral anticoagulant therapy with clinic management - A randomized trial". *Annals of Internal Medicine*, 2005. **142**(1): p. 1-10.

145. Quick, A.J., M. Stanley-Browne, and F.W. Bancroft, "A study of the coagulation defect in hemophilia and in jaundice". *American Journal of the Medical Sciences*, 1935. **190**: p. 501-511.

146. Owren, P.A. and K. Aas, "The Control of Dicumarol Therapy and the Quantitative Determination of Prothrombin and Proconvertin". *Scandinavian Journal of Clinical & Laboratory Investigation*, 1951. **3**(3): p. 201-208.

147. Lowe, L.B., S.H. Brewer, S. Kramer, R.R. Fuierer, G.G. Qian, C.O. Agbasi-Porter, S. Moses, S. Franzen, and D.L. Feldheim, "Laser-induced temperature jump electrochemistry on gold nanoparticle-coated electrodes". *Journal of the American Chemical Society*, 2003. **125**(47): p. 14258-14259.

148. Korte, W., S. Clarke, and J.B. Lefkowitz, "Short activated partial thromboplastin times are related to increased thrombin generation and an increased risk for thromboembolism". *American Journal of Clinical Pathology*, 2000. **113**(1): p. 123-127.

149. Donahue, S.M. and C.M. Otto, "Thromboelastography: a tool for measuring hypercoagulability, hypocoagulability, and fibrinolysis". *Journal of Veterinary Emergency and Critical Care*, 2005. **15**(1): p. 9-16.

150. Lim, H., J. Nam, Y. Lee, S. Xue, S. Chung, and S. Shin, "Blood Coagulation study using light-transmission method". *Korea University*, 2010.

151. Vikinge, T.P., K.M. Hansson, P. Sandstrom, B. Liedberg, T.L. Lindahl, I. Lundstrom, P. Tengvall, and F. Hook, "Comparison of surface plasmon resonance and quartz crystal microbalance in the study of whole blood and plasma coagulation". *Biosensors & Bioelectronics*, 2000. **15**(11-12): p. 605-613.

152. Hansson, K., T.P. Vikinge, M. Rånby, P. Tengvall, I. Lundström, K. Johansen, and T. Lindahl, "Surface plasmon resonance (SPR) analysis of coagulation in whole blood with application in prothrombin time assay". *Biosensors and Bioelectronics*, 1999. **14**(8): p. 671-682.

153. Kalchenko, V., A. Brill, M. Bayewitch, I. Fine, V. Zharov, E. Galanzha, V. Tuchin, and A. Harmelin, "In vivo dynamic light scattering imaging of blood coagulation". *Journal of biomedical optics*, 2007. **12**(5): p. 052002-052002-4.

154. Ur, A., "Changes in the electrical impedance of blood during coagulation". 1970.

155. Lei, K.F., K.H. Chen, P.H. Tsui, and N.M. Tsang, "Real-Time Electrical Impedimetric Monitoring of Blood Coagulation Process under Temperature and Hematocrit Variations Conducted in a Microfluidic Chip". *Plos One*, 2013. **8**(10).

156. Puckett, L.G., G. Barrett, D. Kouzoudis, C. Grimes, and L.G. Bachas, "Monitoring blood coagulation with magnetoelastic sensors". *Biosensors and Bioelectronics*, 2003. **18**(5): p. 675-681.

157. Morales Cruzado, B., S. Vázquez y Montiel, and J.A. Delgado Atencio. "Behavior of optical properties of coagulated blood sample at 633 nm wavelength". 2011.

158. Tripathi, M.M., Z. Hajjarian, E.M. Van Cott, and S.K. Nadkarni, "Assessing blood coagulation status with laser speckle rheology". *Biomedical Optics Express*, 2014. **5**(3): p. 817-831.

159. Liang, W., Y.Y. Huang, Y. Xu, R.K. Lee, and A. Yariv, "Highly sensitive fiber Bragg grating refractive index sensors". *Applied Physics Letters*, 2005. **86**(15).

160. Wu, D.K.C., B.T. Kuhlmey, and B.J. Eggleton, "Ultrasensitive photonic crystal fiber refractive index sensor". *Optics Letters*, 2009. **34**(3): p. 322-324.

161. De Vos, K., I. Bartolozzi, E. Schacht, P. Bienstman, and R. Baets, "Silicon-on-Insulator microring resonator for sensitive and label-free biosensing". *Optics express*, 2007. **15**(12): p. 7610-7615.

162. Ding, J.-F., L.-Y. Shao, J.-H. Yan, and S. He, "Fiber-taper seeded long-period grating pair as a highly sensitive refractive-index sensor". *Photonics Technology Letters, IEEE*, 2005. **17**(6): p. 1247-1249.

163. Jorgenson, R. and S. Yee, "A fiber-optic chemical sensor based on surface plasmon resonance". *Sensors and Actuators B: Chemical*, 1993. **12**(3): p. 213-220.

164. Pal, S.S., S.K. Mondal, U. Tiwari, P.V.G. Swamy, M. Kumar, N. Singh, P.P. Bajpai, and P. Kapur, "Etched multimode microfiber knot-type loop interferometer refractive index sensor". *Review of Scientific Instruments*, 2011. **82**(9).

165. Chen, L.X., X.G. Huang, J.Y. Li, and Z.B. Zhong, "Simultaneous measurement of refractive index and temperature by integrating an external Fabry-Perot cavity with a fiber Bragg grating". *Review of Scientific Instruments*, 2012. **83**(5).

166. Wang, Y., D. Wang, M. Yang, W. Hong, and P. Lu, "Refractive index sensor based on a microhole in single-mode fiber created by the use of femtosecond laser micromachining". *Optics letters*, 2009. **34**(21): p. 3328-3330.

167. Zhang, A.P., G.F. Yan, S.R. Gao, S.L. He, B. Kim, J. Im, and Y. Chung, "Microfluidic refractive-index sensors based on small-hole microstructured optical fiber Bragg gratings". *Applied Physics Letters*, 2011. **98**(22).

168. Gu, Z.Z., R. Horie, S. Kubo, Y. Yamada, A. Fujishima, and O. Sato, "Fabrication of a Metal-Coated Three-Dimensionally Ordered Macroporous Film and its Application as a Refractive Index Sensor". *Angewandte Chemie*, 2002. **114**(7): p. 1201-1204.

169. Tian, Z., S.S. Yam, and H.-P. Loock, "Refractive index sensor based on an abrupt taper Michelson interferometer in a single-mode fiber". *Optics letters*, 2008. **33**(10): p. 1105-1107.

170. Barton, J.K., D.P. Popok, and J.F. Black, "Thermal analysis of blood undergoing laser photocoagulation". *Ieee Journal of Selected Topics in Quantum Electronics*, 2001. **7**(6): p. 936-943.

171. Jedrzejewska-Szczerska, M., "Measurement of complex refractive index of human blood by low-coherence interferometry". *European Physical Journal-Special Topics*, 2013. **222**(9): p. 2367-2372.

172. Drezek, R., A. Dunn, and R. Richards-Kortum, "A pulsed finite-difference time-domain (FDTD) method for calculating light scattering from biological cells over broad wavelength ranges". *Optics Express*, 2000. **6**(7): p. 147-157.

173. Campbell, S.A., "The science and engineering of microelectronic fabrication". 1996: Oxford University Press, USA.

174. Cheemalapati, S., M. Ladanov, J. Winskas, and A. Pyayt, "Optimization of dry etching parameters for fabrication of polysilicon waveguides with smooth sidewall using a capacitively coupled plasma reactor". *Applied Optics*, 2014. **53**(25): p. 5745-5749.

175. Barrera, F.J., B. Yust, L.C. Mimun, K.L. Nash, A.T. Tsin, and D.K. Sardar, "Optical and spectroscopic properties of human whole blood and plasma with and without Y2O3 and Nd3+:Y2O3 nanoparticles". *Lasers in Medical Science*, 2013. **28**(6): p. 1559-1566.

176. Rappaz, B., A. Barbul, F. Charriere, J. Kühn, P. Marquet, R. Korenstein, C. Depeursinge, and P. Magistretti. "Erythrocytes volume and refractive index measurement with a digital holographic microscope". in *Biomedical Optics (BiOS) 2007*. 2007. International Society for Optics and Photonics.

177. Turgeon, M.L., "Clinical Hematology: Theory and Procedures". 2005: Lippincott Williams & Wilkins.

178. Tangelder, G.J., D.W. Slaaf, A.M.M. Muijtjens, T. Arts, M.G.A.O. Egbrink, and R.S. Reneman, "Velocity Profiles of Blood-Platelets and Red-Blood-Cells Flowing in Arterioles of the Rabbit Mesentery". *Circulation Research*, 1986. **59**(5): p. 505-514.

# APPENDIX A: CELL STAINING PROCEDURES, LITERATURE SUMMARY AND APPROVAL LETTER

## A.1 *In-Vitro* Experiments Cell Staining Procedures

### A.1.1 Fibroblast Acridine Orange Experiment

The fibroblast cells were fixed in in 4% paraformaldehyde, rinsed with phosphate buffer saline (PBS) solution and incubated for 2 minutes in Acridine orange solution of concentration 10 µg/ ml, and then were rinsed and used in nanoendoscope experiment.

### A.1.2 MDA-MB-231 MitoTracker Experiment

Mitochondria were labeled by incubating cells with 100 nM MitoTracker (Life Technologies) at 37°C for 30 min followed by PBS washing for three times. Stained live cells were subjected to nanoendoscope experiment.

### A.1.3 Liver Cell Hoechst Experiment

Live cells were stained with Hoechst (10 µg/mL) diluted in HCM for 30 minutes at 37°C, rinsed and used in nanoendoscope experiment.

## A.2 Cell Viability Experiments Staining Procedures

### A.2.1 Experiment 1

In experiment 1, the live Dead Cell kit showing green fluorescence of live cells was continuously interrogated with the nanoendoscope.

### A.2.2 Experiment 2

In experiment 2, the live cells were stained with CellTracker™ Green CMFDA Dye (50 µg/mL) and Hoechst (10 µg/mL) diluted in HCM for 30 minutes at 37°C.

### A.2.3 Experiment 3

In experiment 3, live cells were stained with CellTracker™ Green CMFDA Dye (50 µg/mL) and Hoechst (10 µg/mL) diluted in HCM for 30minutes at 37°C.

## A.3 Summary of Single Cell Analysis Devices

Table A1 A summary of single cell analysis devices.

| S.No | Device | Study | Significance of the study | Signal detected | Reference |
|---|---|---|---|---|---|
| 1 | Nanofibers. | Detection of enzyme lactate. | Increased lactase is correlated to higher incidence of metastasis. | Fluorescence. | [28] |
| 2 | Nanofibers. | Detection Ca ion concentration. | It acts intracellular messengers. Increase in calcium ion concentration can cause cell death. | Fluorescence. | [31] |
| 3 | Nanofibers. | Sensing of pH. | It is important for various functions such as metabolism, apoptosis and malignancy. | Fluorescence. | [43] |
| 4 | CNT attached onto AFM + QD. | Deliver QD into a single cell. | Deliver cargo. | Fluorescent microscopy signal. | [49] |
| 5 | CNT on Glass pipette. | SERS in signal cell and preliminary electrochemical studies outside cell. | Sensing and Deliver cargo. | Raman signal. | [51] |
| 6 | CNT on glass capillaries. | SERS analysis in different parts of a single cell. | It was proposed that, in future, this device can be used for real time detection of heterogeneous cells. | Raman signal. | [52] |

Table A1 Continued.

| S.No | Device | Study | Significance of the study | Signal detected | Reference |
|---|---|---|---|---|---|
| 7 | Needle nano probe. | Electrochemical measurements in microenvironments. | Can facilitate future intracellular studies. | Electrical signals. | [53] |
| 8 | Nano needle + QD. | Deliver QD into a single cell. | Deliver cargo and monitor diffusion of released quantum dots across the cell to estimate several biophysical properties of the cell. | Fluorescent microscopy signal. | [54] |
| 9 | Nanowires based device. | SERS spectroscopy. | Demonstrated in-situ intracellular analysis. | Raman signal. | [55] |
| 10 | Nano needle. | Deliver DNA into single cell. | Deliver cargo. | Fluorescent microscopy signal. | [56] |
| 11 | Fiber + NW. | 1) Deliver QD 2) Measure pH. | Cargo delivery. | Fluorescence. | [57] |
| 12 | Fiber+ Nanocavity. | Sensing of protein streptavidin | | Photoluminescence spectra. | [59] |
| 13 | Nanofibers. | Detection of caspase-9 activity. | Detect onset of apoptosis. | Fluorescence. | [60] |
| 14 | Nanofibers. | Detection of Ca Ion concentration. | Smooth muscle contractility is regulated by $[Ca2^{+}]$ concentration. | Fluorescence. | [61] |
| 15 | Nanofibers. | Detection of benzopyrene tetrol (BPT). | Cancer biomarker. | Fluorescence. | [62] |
| 16 | Nanofibers. | Detection of telomerase. | Cancer biomarker. | Fluorescence. | [63] |
| 17 | Nanofibers. | Measurement of BaP. | Carcinogen. | Fluorescence. | [64] |
| 18 | Nanofibers+ NP. | Detection of protein p53. | Tumor suppressor protein. | LSPR. | [66] |
| 19 | Pulled glass. | SERS response to addition of KCl. | Demonstrate in-situ intracellular analysis during external stimuli. | Raman signal. | [67] |
| 20 | Nanofibers. | Detection of cytochrome c. | | Fluorescence. | [69] |

## A.4 Approval for Re-Printing

The approval email received from OSA for reproducing the work presented in this dissertation**.**

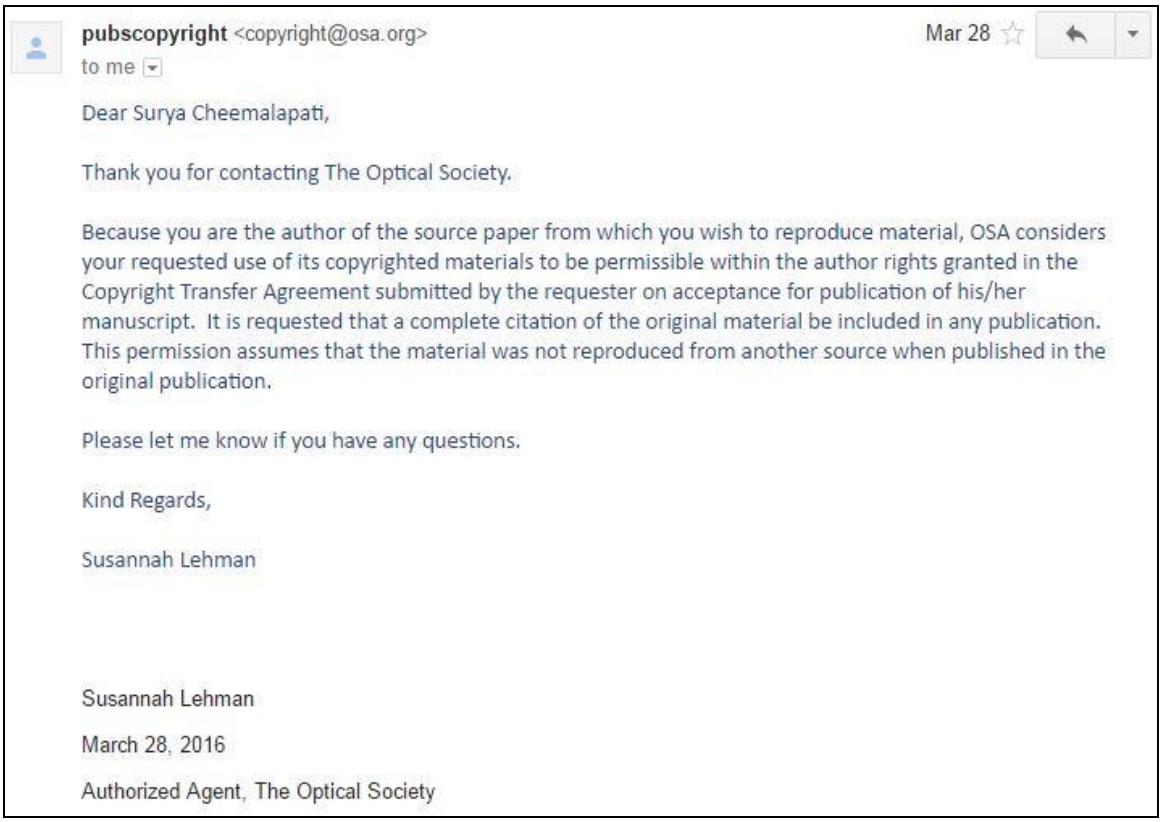

**pubscopyright** <copyright@osa.org> Mar 28

to me

Dear Surya Cheemalapati,

Thank you for contacting The Optical Society.

Because you are the author of the source paper from which you wish to reproduce material, OSA considers your requested use of its copyrighted materials to be permissible within the author rights granted in the Copyright Transfer Agreement submitted by the requester on acceptance for publication of his/her manuscript. It is requested that a complete citation of the original material be included in any publication. This permission assumes that the material was not reproduced from another source when published in the original publication.

Please let me know if you have any questions.

Kind Regards,

Susannah Lehman

Susannah Lehman

March 28, 2016

Authorized Agent, The Optical Society

## A.5 Articles

Below are the first pages of the articles reproduced in this dissertation with permission from OSA.

# Optimization of light delivery by a nanowire-based single cell optical endoscope

**Mikhail Ladanov,[1] Surya Cheemalapati,[1] and Anna Pyayt,[1,*]**

*[1]Department of Chemical and Biomedical Engineering, University of South Florida, 4202 E. Fowler Ave. Tampa, FL 33620, USA*

*[*]pyayt@usf.edu*

**Abstract:** Here we present a new design and FDTD simulations of light delivery by a nanowire-based intracellular endoscope. Nanowires can be used for minimally invasive and very local light delivery inside cells. One of the main challenges is coupling of light into the nanowire. We propose a new plasmonic coupler interface between cleaved optical fiber and a nanowire, and optimize light coupling efficiency and contrast.



**OCIS codes:** (170.0170) Medical optics and biotechnology; (220.0220) Optical design and fabrication

**References and links**

1. H. Andersson and A. van den Berg, "Microtechnologies and nanotechnologies for single-cell analysis," Curr. Opin. Biotechnol. 15(1), 44–49 (2004).
2. J. E. Ferrell, Jr. and E. M. Machleder, "The biochemical basis of an all-or-none cell fate switch in xenopus oocytes," Science 280(5365), 895–898 (1998).
3. J. S. Marcus, W. F. Anderson, and S. R. Quake, "Microfluidic single-cell mRNA isolation and analysis," Anal. Chem. 78(9), 3084–3089 (2006).
4. W. J. Blake, M. KAErn, C. R. Cantor, and J. J. Collins, "Noise in eukaryotic gene expression," Nature 422(6932), 633–637 (2003).
5. M. B. Elowitz, A. J. Levine, E. D. Siggia, and P. S. Swain, "Stochastic gene expression in a single cell," Science 297(5584), 1183–1186 (2002).
6. M. N. Teruel and T. Meyer, "Parallel single-cell monitoring of receptor-triggered membrane translocation of a calcium-sensing protein module," Science 295(5561), 1910–1912 (2002).
7. S. Lindström and H. Andersson-Svahn, "Miniaturization of biological assays — Overview on microwell devices for single-cell analyses," Biochimica et Biophysica Acta (BBA) - General Subjects 1810(3), 308–316 (2011).
8. B. H. Villas, "Flow cytometry: an overview," Cell Vis. 5(1), 56–61 (1998).
9. P. O. Krutzik and G. P. Nolan, "Fluorescent cell barcoding in flow cytometry allows high-throughput drug screening and signaling profiling," Nat. Methods 3(5), 361–368 (2006).
10. J. P. Nolan and L. A. Sklar, "The emergence of flow cytometry for sensitive, real-time measurements of molecular interactions," Nat. Biotechnol. 16(1), 633–638 (1998).
11. M. Ohsim, "High-throughput microscopy must re-invent the microscope rather than speed up its functions," Br. J. Pharmacol. 152(1), 1–4 (2007).
12. R. Pepperkok and J. Ellenberg, "High-throughput fluorescence microscopy for systems biology," Nat. Rev. Mol. Cell Biol. 7(9), 690–696 (2006).
13. Z. Oryabayeva, R. Singhal, E. A. Vitol, M. G. Schrlau, E. Papazoglou, G. Friedman, and Y. Gogotsi, "Physiological validation of cell health upon probing with carbon nanotube endoscope and its benefit for single-cell interrogation," Nanomedicine 8(5), 590–598 (2012).
14. R. Singhal, Z. Oryabayeva, R. V. Kalyana Sundaram, J. J. Niu, S. Bhattacharyya, E. A. Vitol, M. G. Schrlau, E. S. Papazoglou, G. Friedman, and Y. Gogotsi, "Multifunctional carbon-nanotube cellular endoscopes," Nat. Nanotechnol. 6(1), 57–64 (2011).
15. R. Yan, J.-H. Park, Y. Choi, C.-J. Heo, S.-M. Yang, L. P. Lee, and P. Yang, "Nanowire-based single-cell endoscopy," Nat. Nanotechnol. 7(3), 191–196 (2011).
16. X. Chen, A. Kis, A. Zettl, and C. R. Bertozzi, "A cell nanoinjector based on carbon nanotubes," Proc. Natl. Acad. Sci. U.S.A. 104(20), 8218–8222 (2007).
17. K. Yum, S. Na, Y. Xiang, N. Wang, and M.-F. Yu, "Mechanochemical delivery and dynamic tracking of fluorescent quantum dots in the cytoplasm and nucleus of living cells," Nano Lett. 9(5), 2193–2198 (2009).
18. R. Singhal, S. Bhattacharyya, Z. Oryabayeva, E. Vitol, G. Friedman, and Y. Gogotsi, "Small diameter carbon nanopipettes," Nanotechnology 21(1), 015304 (2010).

#196578 - $15.00 USD Received 30 Aug 2013; revised 23 Oct 2013; accepted 26 Oct 2013; published 7 Nov 2013

18 November 2013 | Vol. 21, No. 23 | DOI:10.1364/OE.21.028001 | OPTICS EXPRESS 28001

# Optimization of dry etching parameters for fabrication of polysilicon waveguides with smooth sidewall using a capacitively coupled plasma reactor

Surya Cheemalapati, Mikhail Ladanov, John Winskas, and Anna Pyayt*

Department of Chemical and Biomedical Engineering, University of South Florida, 4202 E. Fowler Ave. ENB118, Tampa, Florida 33620, USA

*Corresponding author: pyayt@usf.edu

Received 9 May 2014; revised 28 June 2014; accepted 22 July 2014; posted 1 August 2014 (Doc. ID 211810); published 28 August 2014

In this paper, we demonstrate the optimization of a capacitively coupled plasma etching for the fabrication of a polysilicon waveguide with smooth sidewalls and low optical loss. A detailed experimental study on the influences of RF plasma power and chamber pressure on the roughness of the sidewalls of waveguides was conducted and waveguides were characterized using a scanning electron microscope. It was demonstrated that optimal combination of pressure (30 mTorr) and power (150 W) resulted in the smoothest sidewalls. The optical losses of the optimized waveguide were $4.1 \pm 0.6$ dB/cm.



*OCIS codes:* (230.7370) Waveguides; (240.5770) Roughness; (220.4000) Microstructure fabrication.
http://dx.doi.org/10.1364/AO.53.005745

## 1. Introduction

Optical waveguides are critical building blocks of on-chip photonics. Quality of an optical waveguide is largely defined by its optical loss. For straight polysilicon waveguides, absorption and scattering at grain boundaries [1,2], substrate coupling, and radiation loss at etched waveguide sidewalls are the main sources of optical loss [3–5]. Therefore, thicker waveguide claddings can be used to minimize substrate coupling loss and fabrication can be optimized to decrease the surface roughness [1,6,7]. A photolithographic mask used for waveguide patterning has to be printed with high resolution to reduce line edge roughness [8,9]. Additionally, postprocessing methods can be used to make sidewalls smoother. They include gas phase oxidation [10], wet chemical oxidation [11], hydrogenation [2], resist reflow [12], end facet polishing [13], and related processes [14]. This requires the introduction of additional fabrication steps, and increases error rates and cost of the fabrication process. Ideally, fabrication should be done using a simple process with a small number of steps. Since etching of the waveguide is frequently done using one of the dry etching techniques, and capacitively coupled plasma reactors are still widely spread, we conducted a study of optimization of the optical waveguide fabrication using this equipment.

Traditionally, etching of planar waveguides is done using either inductively coupled plasma (ICP) with a passivation gas flow or electron cyclotron resonance (ECR) plasma [15–17], since they have a high density of plasma, high directionality, and higher power levels. However, this equipment is very expensive and, thus, unavailable in many microfabrication facilities, while capacitively coupled plasma reactors are less expensive and more readily available, but were not previously used for this application [18]. Here, we demonstrate the application of a capacitively coupled plasma reactor for the fabrication of polysilicon photonic waveguides with a low loss of $4.1 \pm 0.6$ dB/cm by the optimization of process parameters, such

1559-128X/14/255745-05$15.00/0